Technische Universität Braunschweig

Daniel Dario Schmidt

Evaluation of imaging parameters in Magnetic Particle Imaging

Berichte aus dem **Institut für Elektrische Messtechnik und Grundlagen der Elektrotechnik**

Band 57

Hrsg. Prof. Dr. Meinhard Schilling

Evaluation of imaging parameters in Magnetic Particle Imaging

Von der Fakultät für Elektrotechnik, Informationstechnik, Physik
der Technischen Universität Carolo-Wilhelmina zu Braunschweig

zur Erlangung des Grades eines Doktors
der Ingenieurwissenschaften (Dr.-Ing.)

genehmigte Dissertation

von:	Dipl. Wirtsch.-Ing. Daniel Dario Schmidt
aus:	Geesthacht

eingereicht am:	16.06.2017
mündliche Prüfung am:	03.11.2017

1. Referent:	Prof. Dr. Meinhard Schilling
2. Referent:	Prof. Dr. Tobias Knopp
Vorsitzender:	PD Dr. Frank Ludwig

Druckjahr: 2018

Dissertation an der Technischen Universität Braunschweig,
Fakultät für Elektrotechnik, Informationstechnik, Physik

Kurzfassung

Magnetic Particle Imaging (MPI) ist eine medizinische bildgebende Methode, die sich aktuell (Stand: 2017) im präklinischen Stadium befindet. Die Bildgebung basiert auf der ortsaufgelösten Detektion magnetischer Nanopartikel, die in einem magnetischen Wechselfeld periodisch magnetisiert werden. Mittels Gradientenfeldern, die eine Ortsauflösung ermöglichen, sowie Detektionsspulen, die die Magnetisierungsvorgänge erfassen, kann die Partikelverteilung aus dem Messsignal rekonstruiert werden. Dabei wird Körpergewebe von der Bildgebung ignoriert. Aufgrund des Verzichts auf Radiopharmazeutika sowie ionisierender Strahlung hat MPI gegenüber seinen potenzielle Konkurrenten CT-Angiographie und Bildgebungsmethoden der Nuklearmedizin wie SPECT und PET einen inhärenten Vorteil. Aufgrund dieses Vorteils sowie der hohen räumlicher als auch zeitlichen Auflösung ist MPI ein weltweites Forschungsthema.

Parallel zum MPI hat sich die Magnetic Particle Spectroscopy (MPS) als Methode zur Charakterisierung des Verhaltens magnetischer Nanopartikel unter MPI-Bedingungen etabliert. Mit Ausnahme der Gradientenfelder und somit ohne Ortscodierung werden die potentiellen Tracer der typischen MPI-Umgebung ausgesetzt und die Antwort auf das Anregungsfeld gemessen. Diese Antwort gilt als Indikator einer guten oder schlechten Eignung der magnetischen Nanopartikel als Tracer für MPI. Da diese Methode jedoch nur relative Aussagen über die Bildqualität zulässt und quantitative Abschätzungen über eine erreichbare räumliche Auflösung unter Berücksichtigung des Signal-zu-Rausch-Verhältnisses nur in Phantomstudien im MPI-Scanner möglich sind, besteht hier Optimierungspotential.

Der erste Teil der Arbeit beschreibt den Einfluss des Messsignals im MPI auf die räumliche Auflösung. Basierend auf klassischen Theorien der Signalverarbeitung und der Bildgebung wird das MPI-Signal bezüglich des Nyquist-Shannon-Sampling-Theorems und der Ortsfrequenzen analysiert und auf einen direkten Zusammenhang zwischen Harmonischen und den Ortsfrequenzen hingewiesen. Auf Basis eines je nach Tracermenge und -eigenschaften variierenden Signal-zu-Rausch-Verhältnisses wird die räumliche Auflösung in einen Zusammenhang mit den über dem Rauschlevel liegenden Harmonischen des MPI-Signals gebracht.

Im zweiten Teil wird anhand einer Simulation präsentiert, wie die Tracereigenschaften für MPI-Bedingungen optimiert werden können, um dadurch die räumliche

Auflösung zu maximieren. Es wird dabei gezeigt, dass die Optimierung der Tracer für MPI aufgrund dynamischer Effekte nur über die Abstimmung mehrerer Parameter geschehen kann und dass die Partikel mitunter bei nur leichter Abweichung von dieser Abstimmung bedeutend schwächere Signale im MPI erzeugen können. Final wird ein Faktor präsentiert, der sich in den Simulationen als weitestgehend unabhängig von den externen Parametern Feldstärke und Frequenz zeigt und sich somit als allgemeiner Fixpunkt für optimierte MPI Tracer zu eignen scheint.

Im dritten und letzten Teil der Arbeit wird eine Erweiterung der MPS vorgestellt, die im Gegensatz zur gängigen Methode eine Abschätzung der erreichbaren räumlichen Auflösung des Tracers in Abhängigkeit von Tracermenge und -eigenschaften ermöglicht. Neben der Charakterisierung mehrerer kommerziell erhältlicher Tracer wird darüber hinaus die im ersten Teil vorgestellte Theorie erfolgreich verifiziert. Vergleichend wird zudem eine Studie vorgestellt, in der mehrere Auflösungsphantome eines Tracers in einem kommerziellen MPI-Scanner gemessen wurden. Auch hier stellte sich heraus, dass die Ergebnisse aus der vorgestellten Methode und den Phantom-Experimenten sehr ähnlich sind. Es wird daraus geschlossen, dass die Methode sich gut zur Charakterisierung der erreichbaren räumlichen Auflösung in MPI eignet.

Abstract

Magnetic Particle Imaging (MPI) is a medical imaging modality, that is (in the current state in 2017) in the preclinical stage. It is based on the spatially encoded detection of magnetic nanoparticles that are magnetized by an external magnetic field. Employing gradient fields for spatial encoding and pickup coils to measure the overall magnetization, the particle distribution can be reconstructed from the measurement signal. Body tissue is ignored with this technology. Due to the non-usage of radiopharmaceuticals or ionizing radiation, MPI has an inherent advantage over its potential competitors CT-angiography and the methods of nuclear medicine imaging like SPECT and PET. Based on this advantage and the potential high spatial and temporal resolution, MPI is a worldwide topic of research.

Besides MPI, the Magnetic Particle Spectroscopy (MPS) has been established for the characterization of magnetic nanoparticles under MPI conditions. Except for the gradient field and therefore the spatial encoding, the potential tracers are exposed to the typical MPI environment and their response to the excitation field is measured. This response is taken as an indicator of the suitability of the magnetic nanoparticles as a tracer for MPI. Since this method only yields relative information, an MPI scanner is still needed for quantitative estimations regarding the spatial resolution under consideration of the signal-to-noise ratio. This leaves room for optimization.

The first part of the thesis describes the influence of the measurement signal on the spatial resolution in MPI. Based on classic theories of signal-processing and imaging, the MPI signal is analyzed regarding the Nyquist-Shannon-Sampling-Theorem and the spatial frequencies and a direct relationship between spatial frequencies and harmonic structure is indicated. Depending on the amount of tracers and their properties, the signal-to-noise ratio varies and the spatial resolution is related to the harmonics above noise level.

In the second part, it is presented based on simulation results how the tracer properties may be optimized for MPI to maximize the spatial resolution. It is shown, that due to dynamic effects, tracers need to be attuned specifically for MPI via several parameters and sometimes even slight deviations from this may diminish the corresponding MPI signal. Finally, a parameter is presented that was mostly independent of the applied field strength and frequency. This parameter may therefore be suitable as a general criterion for optimized MPI tracers.

In the third and last part of the thesis, an enhancement of the standard MPS characterization is presented. In contrast to the established method, an estimation of the spatial resolution of the tracer is possible with this new method in dependence on the amount of the tracer and its properties. Besides the characterization of several commercially available tracers, the theory from the first part of the thesis is successfully verified. Moreover, a study is presented in which several resolution phantoms were imaged in a commercial MPI-scanner and compared to the previous resolution characterization of the tracer. It turned out, that the results of both phantom study and the method presented here were very similar. It is therefore concluded that the new method is suitable to characterize the spatial resolution in MPI.

Danksagung

Zunächst möchte ich mich gleichermaßen bei meinen Betreuern am Institut für elektrische Messtechnik an der TU Braunschweig sowie im Fachbereich 8.2 Biosignale der PTB Berlin für die Unterstützung auf dem Weg zu meiner Doktorarbeit bedanken. In Braunschweig ist vor allem mein Doktorvater Professor Dr. Meinhard Schilling zu nennen, der mich bereits durch meine Diplomarbeit begleitet hat und mir anschließend die Möglichkeit gab, als externer Doktorand meine Arbeit im Bereich Magnetic Particle Imaging bei ihm zu schreiben. Weiterhin bedanke ich mich bei PD Dr. Frank Ludwig für die vielen hilfreichen Diskussionen und Anregungen. Aus der Arbeitsgruppe in Berlin bedanke ich mich bei Professor Dr. Lutz Trahms, dass er mir die Gelegenheit gegeben hat, in seinem Fachbereich meine Doktorarbeit zu schreiben und für seinen Einsatz, sobald mal ein Vertrag ausgelaufen war. Ferner bedanke ich mich bei Dr. Uwe Steinhoff für die exzellente Betreuung und die vielen hilfreichen Diskussionen und Anregungen.

Bedanken möchte ich mich auch bei den anderen Doktoranden, Mitarbeitern und Gastwissenschaftlichern der PTB Berlin für die interessanten Diskussionen beim Kaffee, die gemeinsamen Kneipenabende und speziell bei den Doktoranden für die Gesellschaft, wenn wir mal wieder den ganzen Samstag im Labor saßen.

Abschließend bedanke ich mich bei meiner Familie, die mich all die Jahre unterstützt hat und ohne die ich sicherlich nie soweit gekommen wäre und bei all meinen Freunden, die mich in besonders stressigen Phasen ertragen haben.

Contents

List of Figures

List of Tables

List of Abbrevations

MNP Magnetic Nanoparticles

MPI Magnetic Particle Imaging

MPS Magnetic Particle Spectroscopy

FOV Field of View

FFP Field Free Point

PSF Point Spread Function

SVD Singular Value Decomposition

SNR Signal to Noise Ratio

MPMS Magnetic Properties Measurement System

FWHM Full Width at Half Maximum

MTF Modulation Transfer Function

List of Symbols

Sign	Description	Unit
H	magnetic field strength	$\frac{\mathrm{A}}{\mathrm{m}}$
f	frequency	$\frac{1}{\mathrm{s}}$
B	magnetic flux density	T
μ_0	vacuum permeability	$\frac{\mathrm{Vs}}{\mathrm{Am}}$
G	gradient field	$\frac{\mathrm{T}}{\mathrm{m}}$
$\mathbf{A}$	System matrix	$\frac{\mathrm{Am}^2}{\mathrm{mol(Fe)}}$
s	MPI signal	Am^2
n	Number of voxels	1
u	Voltage	V
E	Eletrical field	$\frac{\mathrm{V}}{\mathrm{m}}$
j	Harmonic number	1
p	Coil sensitivity	$\frac{1}{\mathrm{m}}$
M	Magnetization	$\frac{\mathrm{A}}{\mathrm{m}}$
M_{sat}	Saturation magnetization	$\frac{\mathrm{A}}{\mathrm{m}}$
E_{total}	Total energy contributions	J
E_{A}	Anisotropy energy	J
E_{H}	Magnetic energy	J
Θ	Angle between magnetic moment and anisotropy axis	°
φ	Angle between magnetic moment and magnetic field	°
Ψ	Angle between external field and magnetic moment	°
K	Effective anisotropy constant	$\frac{\mathrm{J}}{\mathrm{m}^3}$
d_{c}	Core diameter	nm
D_{h}	Hydrodynamic diameter	nm
d_{h}	Hydrodynamic shell thickness	nm
V_c	Core volume	nm^3
V_H	Hydrodynamic volume	nm^3
H_A	Anisotropy field	$\frac{\mathrm{A}}{\mathrm{m}}$
η	Viscosity	$\mathrm{Pa} \cdot \mathrm{s}$
τ_{N}	Néel relaxation	s

$\tau_{\mathrm{N,H}}$	Field dependent Néel relaxation	s
τ_{B}	Brownian relaxation	s
$\tau_{\mathrm{B,H}}$	Field dependent Brownian relaxation	s
τ_{eff}	Effective relaxation	s
μ	Median diameter	nm
σ	Standard deviation	1
β	Fraction of the first mode in a bimodal distribution	1
h	Point spread function	arb. units
P	Magnetic core size distribution	arb. units
k	Final image	arb. units
g	Input	arb. units
l_{fov}	Length of the 1D field of view	mm
ϵ	Extreme value	arb. units
ρ	Iron density	$\frac{\mathrm{Kg}}{\mathrm{m}^3}$
M_{molar}	Molar mass	$\frac{\mathrm{kg}}{\mathrm{mol(Fe)}}$
m_{mass}	Mass	g
N_{mol}	Amount of particles in mol(Fe)	mol(Fe)
N_{P}	Number of particles	1
N_{p}	Amount of per mol iron	$\frac{1}{\mathrm{mol(Fe)}}$
l	Matrix rank	1
R	Resolution	mm
W	Noise level	Am^2
Γ	Weighting factor for singular values	1
ϑ	Harmonic threshold	1
Φ	Magnetic flux	$\mathrm{V} \cdot \mathrm{s}$
κ	Weighting factor for spectrum S	1
$\lvert\tilde{m}_{\mathrm{i}}\rvert$	i-th harmonic amplitude	Am^2
f_{char}	Characteristic frequency	Hz
c_{Fe}	Iron concentration	$\frac{\mathrm{mol}}{\mathrm{L}}$, $\frac{1}{\mathrm{L}}$
F	Filling factor	1
$\tilde{f}$	Number of spatial periods in the field of view	1
f_{spatial}	Spatial frequency	$\frac{1}{\mathrm{mm}}$
l_{G}	Gap width	1
U_n	n-th Chebyshev polynomial of the second kind	1
$\tilde{U}_n$	FFP velocity modulated n-th Chebyshev polynomial of the second kind	1

1. Introduction

Magnetic Particle Imaging (MPI) is a medical imaging modality used to detect Magnetic Nanoparticles (MNP) that serve as tracers in the imaging process [39]. It is based on the nonlinear response of MNP to the excitation with alternating magnetic fields and is therefore not based on ionizing radiation or radioactive tracers. With fast repetition times [142], it qualifies as a potential alternative to CT angiography [112] [103] and due to the ability to target cancerous tissue [68] [134], it might also become an alternative for nuclear medicine imaging [44] [64]. Current modalities for angiography and nuclear medicine imaging potentially pose risks for the patient, which makes an alternative method a desirable goal. The CT angiography has a high radiation dose of up to 12 mSv [54]. Moreover, studies have shown that 25% of all patients undergoing CT angiography suffer from chronic kidney disease [110] [58] and should avoid iodine or gadolinium contrast agents [40], which are usually employed for CT angiography. Regarding nuclear medicine imaging, the PET and SPECT imaging currently being used both rely on the application of radiopharmaceuticals, resulting in the emission of weak radiation.

To become an alternative to these methods and gain acceptance among physicians as well as among patients, three prerequisites need to be satisfied:

- The scanner geometry must be suitable for humans;
- The method must be safe for the patient;
- The image quality must be superior to comparable imaging methods.

To address the third item on the list, it is necessary to develop methods to evaluate quantitatively potential MPI tracers in terms of image quality, especially the spatial resolution, as it reflects the ability to image small details. The resolution depends on the scanner as well as on the tracer and can be improved, for example, by increasing the applied magnetic field strength as well as by using better suited MNP as tracers. This thesis focuses mainly on the influence of MNP on the resolution, but also addresses scanner parameters.

To characterize the potential resolution of different MNP, there are currently two established procedures, corresponding to the two reconstruction principles in MPI:

the spatial domain based Point Spread Function (PSF) and the frequency domain based spectroscopic MPI, called Magnetic Particle Spectroscopy (MPS).

The PSF is the response of an imaging system to a point-like input and is one of the most basic measures of the image quality of medical imaging systems [15] with applications, among others, in CT [60] and MRI [111] and is consequently also applied in MPI [45] [117]. The advantage of the PSF is its intuitive evaluation. A narrow system response in spatial domain to the point-like input is considered to yield a high resolution, whereas a highly broadened system response is considered to yield a low resolution. However, the resolution characterization via the PSF only depends on the width of the system response and is independent of the Signal to Noise Ratio (SNR), which has been shown to heavily influence the achievable resolution in MPI [70].

The characterization via MPS has been established as the most basic characterization technique for potential MPI tracers [8] [98] [52] [90] [4]. The MPS spectrum is the equivalent of the PSF in frequency domain and a relative measure for the image quality. Based on the spectral amplitudes and their decay, whether or not a tracer is suitable for MPI is evaluated without yielding quantitative information regarding the resolution. Sometimes, also single parameters, such as the third harmonic amplitude, are taken as a measure for suitability as an MPI tracer [92] [127] [55].

The magnetic properties of MNP vary greatly in dependence on the employed magnetic core material, the shape and structural composition of the core, the effective anisotropy constant, the nonmagnetic shell, and the size distribution of the tracers (which will be explained in detail later). Due to this variety of influences of MNP properties, a vast amount of literature exists on the synthesis of suitable MPI tracers with several different approaches [35] [38] [74] [65]. The investigation of the influence of different MNP properties on the PSF as well as on the MPS spectrum is not an easy task. A classic approach of modeling the magnetic behavior on a micromagnetic scale is the Landau-Lifshitz-Gilbert equation. It has already been employed to investigate MNP behavior, resulting in several important implications concerning MNP for MPI [141]. However, this method is highly CPU-intensive [80] and therefore impractical to use for large parameter studies. On a macroscopic scale, the so-called Langevin function was employed for several years to simulate the behavior of particle ensembles in MPI [140] [71]. However, the Langevin function ignores dynamic effects that play an important role for the particle behavior at frequencies

employed in MPI [143] [90]. Recently, this issue was addressed by different groups, resulting in several publications on this topic (e.g., [87] [146] [21] [23]).

Despite the importance of the resolution for medical applications and the high number of MNP properties influencing it, there is currently no established method to characterize the resolution of newly synthesized tracers that also considers the SNR apart from phantom experiments. Furthermore, the influence of structural parameters on the MPI signal, as well as on the spatial resolution, is not yet fully understood.

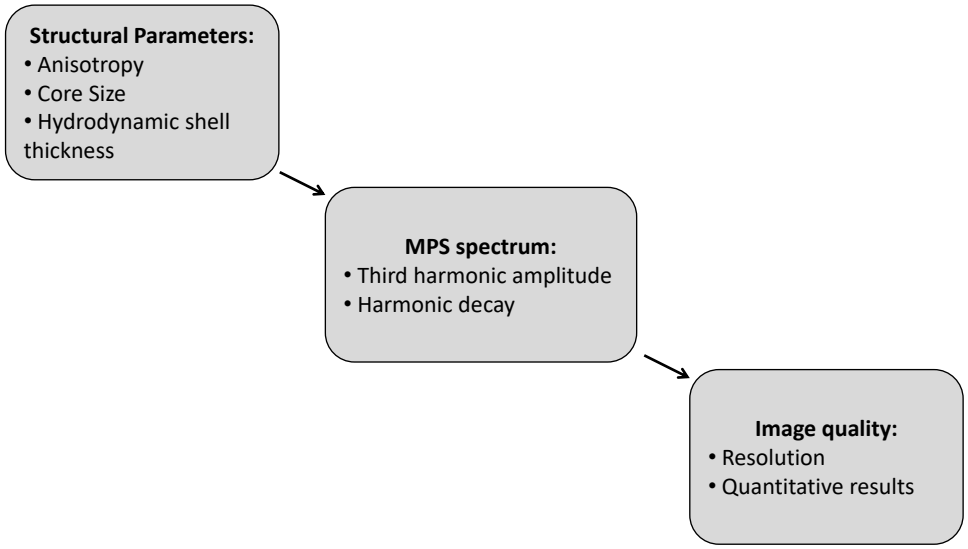

Figure 1: Focus of the PhD Thesis. It is to be investigated how the MPS spectrum is influenced by structural parameters of the MNP and how image quality is related to the MPS spectrum.

Based on the state-of-the-art information outlined above, the focus of this thesis is summarized in Fig. 1. Specifically, this thesis investigates how structural parameters of MNP influence the MPS (and therefore MPI) signal and how the spatial resolution is determined based on this signal. To that end, a simulation environment is developed to perform a comprehensive parameter study with phenomenological expressions of the particle dynamics in a high-frequency magnetic field to better understand the influence of structural parameters.

Furthermore, a method is developed and applied to characterize the achievable resolution of tracers under consideration of the noise level to provide a practical tool to characterize the potential resolution before performing MPI measurements.

The thesis is structured as follows: In **Chapter 2**, the necessary fundamentals will be explained. To understand the behavior of MNP in an MPI setup, the particle physics are covered first. Since the thesis aims to investigate the influence of MNP on the spatial resolution, general means of quantifying the spatial resolution are introduced afterwards, followed by an explanation of the experimental system, especially MPI, but also the characterization techniques MPS and the static magnetization measurements.

In **Chapter 3**, the MNP employed for this thesis are introduced and characterized with the techniques, that were introduced in Chapter 2.

Chapter 4 covers the techniques to quantify the spatial resolution that were introduced in Chapter 2 and sets them in the context of MPI. Furthermore, the influence of the SNR on the spatial resolution in MPI is discussed and an expression for the resolution in MPI in dependence on the available harmonics is introduced.

To find physical properties of the MNP that maximize the resolution, a simulation of the particle behavior in the characterization technique MPS is performed in **Chapter 5**.

Lastly, in **Chapter 6** a new characterization technique that enhances the MPS characterization is introduced to quantify the achievable spatial resolution in MPI. Here, the MNP introduced in Chapter 3 as well as simulated MNP are characterized with the new technique. At the same time, the results obtained here are compared to the theoretical relationship between spatial resolution and available harmonics as well as to regular phantom experiments performed with an MPI scanner.

2. Fundamentals

Since the aim of this thesis is the evaluation of the resolution in MPI, a fundamental understanding of the physics of MNP is just as important as the established methods to describe the image quality in medical imaging and the basics of MPI itself. Firstly, this chapter covers the physics of MNP, beginning with their magnetic structure, followed by a description of the characteristic behavior of superparamagnetic particles and the influence of the entire complex in which the particle core is embedded. Secondly, this chapter covers the abstract term *image quality* including well-established methods for its characterization. Lastly, MPI as well as the spectroscopic MPS and the static magnetization measurement that are employed for the tracer characterization are discussed.

2.1. Magnetic Nanoparticles

MNP are a widely used type of nanoparticles given the possibility of manipulating their behavior with magnetic fields. When discussing MNP, especially in medicine, *nano* means a range of approximately 1 nm to 100 nm in diameter. Applications for larger nanoparticles, or sometimes microparticles, can also be found but are not relevant in the context of this work.

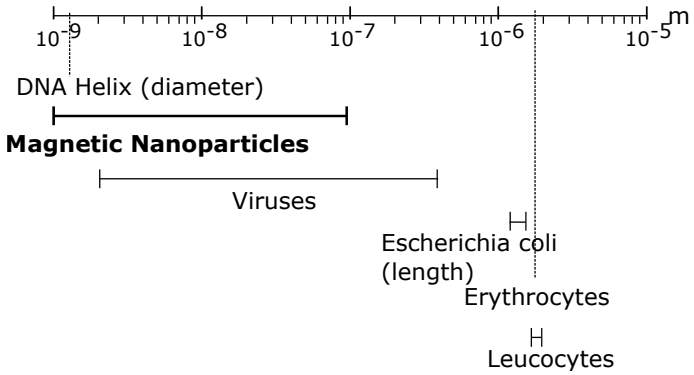

Figure 2: Dimension of magnetic nanoparticles in comparison to biological entities.

As can be seen in Fig. 2, MNP that are subject to research for medical applications are smaller than erythrocytes (red blood cells), leucocytes (white blood cells), and even smaller than some viruses. The possibility of external manipulation as well as its small size make MNP a relevant research tool in medicine with applications

ranging from immunoassays [14] [41] [82] over gene transfer [24] [126] [95], drug delivery [25] [133] [3], magnetic hyperthermia [59] [130] [79] to angiography [39] [42], i.e., MPI.

2.1.1. Single domain particles

Usually, ferromagnetic and ferrimagnetic materials consist of several domains separated by domain walls [84], where each domain has its own net magnetic moment. Those domain walls are formed in a bulk material by the tendency to minimize the internal magnetic energy via the compensation of magnetostatic energy and domain wall energy [102]. Due to the minimization effects, the probability for domain walls decreases with decreasing volume. By reducing the size, at some point a critical volume is reached where it is more energy efficient for all spins to align in the same direction than to build a domain wall. This critical diameter for single domain particles was first derived by Frenkel and Dorfman [36] and was later published in an improved version by Kittel [69], which he proclaimed to be between of $d_c = 10$ nm to $d_c = 100$ nm. The particles considered in this work are all single domain particles and the implications for particle behavior will be described in the following sections.

2.1.2. Magnetic Anisotropy

In the single domain state, all spins of a particle are coupled and the ensemble of spins can be described by one magnetic moment m. The direction of the moment is determined by several energetic influences. Besides the magnetic field strength H, the magnetic anisotropy is a major influence on the direction (Fig. 3).

Under the assumption of uniaxial anisotropy (meaning that there is only one anisotropy axis, i.e., the easy axis) and in the absence of an external magnetic field, the total energy of the particle E_{total} is given by the anisotropy energy E_A:

$$E_{\text{total}} = E_A = -KV_c \sin^2(\theta) \tag{2.1}$$

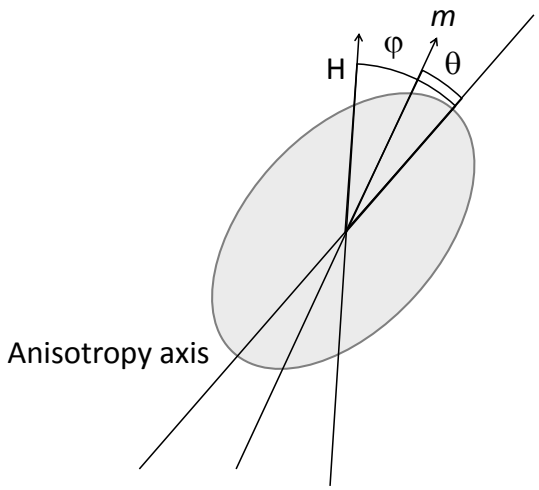

Figure 3: Single domain particle with uniaxial anisotropy. The moment direction and the anisotropy axis form an angle θ. The magnetic field and the anisotropy axis form the angle φ.

with V_c as the particle core volume, K as the effective anisotropy constant and θ as the angle between the magnetically easy axis or anisotropy axis and the magnetic moment [5]. Since the particle tends to minimize its internal energy, there are two stable configurations without an applied external field: At $\theta = 0°$ and $\theta = 180°$ (Fig. 4 middle). In thermal equilibrium, both states are energetically equivalent and therefore equally probable.

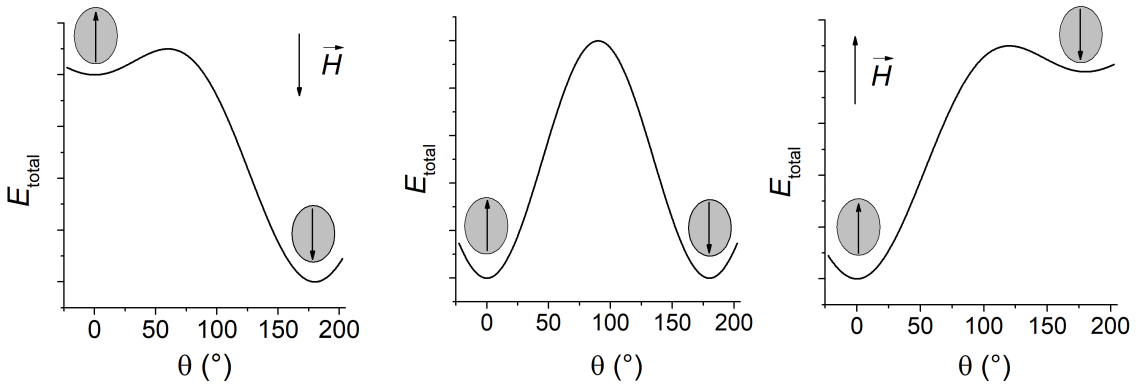

Figure 4: Energy barrier of magnetic nanoparticles with applied magnetic field parallel to the anisotropy axis (left), without applied magnetic field (middle), and with an applied magnetic field antiparallel to the anisotropy axis (right).

When applying an external magnetic field, the energy of the particle not only consists of the anisotropy energy but also of the energy E_{H} induced by the magnetic field [16], resulting in:

$$E_{\mathrm{total}} = E_{\mathrm{A}} + E_{\mathrm{H}} = -KV_{\mathrm{c}}\sin^2(\theta) - m\mu_0 H(\varphi - \theta) \tag{2.2}$$

where μ_0 is the vacuum permeability. Now, the energy landscape of the particle is shifted out of balance and, depending on the direction of the magnetic field, either the direction parallel (Fig. 4 left) or antiparallel (Fig. 4 right) to the anisotropy axis becomes an energetically preferable and more probable state.

2.1.3. Superparamagnetic Behavior of Magnetic Nanoparticles

Another influence on the particle besides the anisotropy and the external magnetic field is the thermal energy $k_{\mathrm{B}}T$ [84], consisting of the Boltzmann-constant k_{B} and the temperature T. For magnetic particles much larger than the nanometer regime, the anisotropy energy is larger than the thermal energy, making the anisotropy axis the energetically preferred orientation. Below a certain particle size, the magnetic moment becomes susceptible to stochastic thermal processes leading to random reorientations of the magnetic moment [5]. Therefore, even though the bulk material of the nanoparticle is still ferromagnetic or ferrimagnetic, it behaves like a paramagnet. Bean and Livingston coined the term superparamagnetism for this behavior and postulated a definition containing two conditions [5]:

- The ensemble of magnetic particles shows no hysteresis effects;
- Magnetization curves superimpose when the x-axis is normalized to temperature T.

Under the assumption of a slowly varying magnetic field and neglectable anisotropy, ensembles of superparamagnetic particles aligned with the magnetic field can be described by the Langevin function:

$$M = M_{\mathrm{sat}}\left(\coth(\xi) - \frac{1}{\xi}\right) \tag{2.3}$$

with:

$$\xi = \frac{m\mu_0 H}{k_B T} = \frac{M_{sat}\pi/6 d_c^3 \mu_0 H}{k_B T}, \tag{2.4}$$

with d_c as the core diameter of spherical particles and M_{sat} as the saturation magnetization. In Fig. 5 the temperature normalized magnetization of particles according to Bean & Livingstons definition with a core size of $d_c = 10$ nm is depicted.

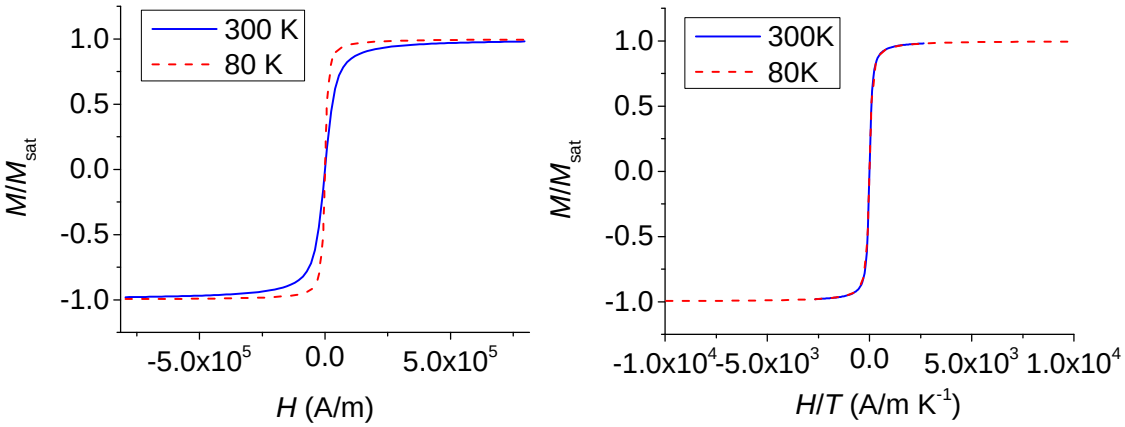

Figure 5: Left: Normalized magnetization curves according to the Langevin function for magnetic nanoparticles with $d_c = 10$ nm at two different temperatures; Right: The same magnetization curves plotted over the temperature normalized magnetic field H/T.

.

Since the assumption of an ensemble of particles all with an identical diameter is not realistic, the multidispersity of MNP will be presented next.

2.1.4. Multidispersity of Magnetic Nanoparticles

So far, it was assumed that all particles of the ensemble have an identical diameter (monodisperse). A more realistic assumption is a size distribution consisting of several different diameters (polydisperse). As shown by Chantrell, the magnetic moments of MNP in an ensemble can be superposed to one total moment (Moment Superposition Model) [16]. The overall magnetic moment of an ensemble of anisotropy free particles in thermal equilibrium then denotes:

$$M = M_{\text{sat}} \int f(d_{\text{c}}) \mathcal{L}(\xi(d_{\text{c}}, H)) \mathrm{d}d_{\text{c}} \tag{2.5}$$

with $f(d_{\text{c}})$ being the distribution function and $\mathcal{L}$ being the Langevin function (2.3) in dependence on $\xi(d_{\text{c}}, H)$ (2.4). Following the proposition of Chantrell [16], the particle distribution is often described via a log-normal distribution [28] [143]:

$$f(d_{\text{c}}) = P(d_{\text{c}}, \mu, \sigma) = \frac{1}{\sqrt{2\pi}\sigma d_{\text{c}}} \exp\left[-\frac{(\ln(d_{\text{c}}) - \ln(\mu))^2}{2\sigma^2} \right] \tag{2.6}$$

where μ is the median diameter of the distribution (not to be confused with the magnetic permeability) and σ is the standard deviation. The size distribution may also be bimodal when it is composed of two separate modes [28]. It then denotes:

$$P(d_{\text{c}}, \mu_1, \sigma_1, \mu_2, \sigma_2, \beta) = (1 - \beta) P_1(d_{\text{c}}, \mu_1, \sigma_1) + \beta P_2(d_{\text{c}}, \mu_2, \sigma_2) \tag{2.7}$$

where β is the fraction of the second mode [28].

The following sections will explain how different particle sizes influence the rotation times in an alternating field and the derived implications concerning the ability to model the particle behavior.

2.1.5. Brownian and Néel relaxation

Up to this point, the change in magnetization due to the excitation with an external magnetic field was considered in the steady state. When operating with (quasi)static magnetic fields, this simplification is absolutely valid. Nevertheless, for quickly changing fields, like the AC fields used in MPI, the time needed for the magnetic moments to align to it has to be taken into account. This reorientation to a field change can be achieved via two principles: The internal reorientation of the magnetic moment or Néel relaxation [99] (Fig. 6 left) and the rotation of the whole particle or Brownian relaxation [13] (Fig. 6 right). Based on the relation

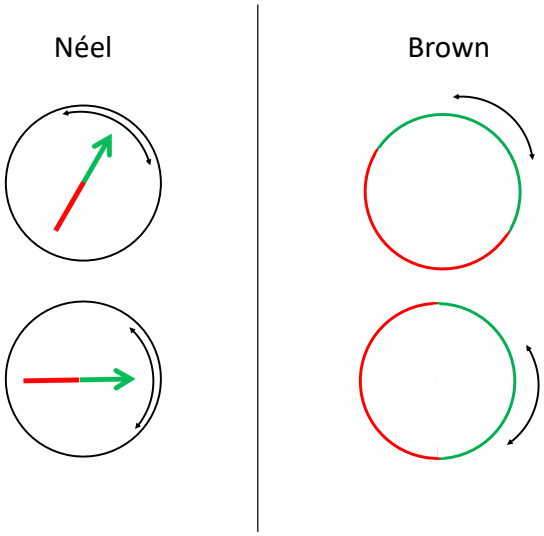

Figure 6: Left: Néel relaxation via rotation of the magnetic moment; Right: Brownian relaxation via rotation of the whole particle.

.

between anisotropy energy $E_A = KV_c$ and thermal energy k_BT, Néel proposed an expression for the thermally excited mean rotation time τ_N of an ensemble of spins with uniaxial anisotropy:

$$\tau_N = \tau_0 \exp\left(\frac{KV_c}{k_BT}\right), \tag{2.8}$$

where τ_0 is the attempt time and V_c is the particle volume. The attempt time is a material dependent constant and is given by several authors as a factor varying between 10^{-8} and 10^{-13} (among others [63], [102], [105]). A mathematical expression for τ_0 when the anisotropy field $H_A = 2K/M_{sat}$ dominates is given by Martsenyuk via:

$$\tau_0 = \frac{M_{sat}}{2\alpha\gamma K} \tag{2.9}$$

with α as the Gilbert damping factor and γ as the gyromagnetic ratio [94].

As the influence of the anisotropy energy grows stronger, for example, as a result of a nonspherical particle shape or generally larger particles, τ_N will reach a point where the particles are no longer agitated by the thermal excitation and are therefore blocked, meaning that the magnetic moment is fixed in the direction of the anisotropy axis.

At this point, only a full rotation of the particle is possible due to their rotational diffusion. This was first derived by Einstein [30] and described for ferrofluids by Brown [13] as:

$$\tau_{\mathrm{B}} = \frac{3V_{\mathrm{H}}\eta}{k_{\mathrm{B}}T} \tag{2.10}$$

where V_{H} is the hydrodynamic volume and η is the viscosity of the suspension. In a medium that allows rotation of the whole particle, MNP realign to an external magnetic field via a combination of those two mechanisms whereby one of them may be the dominating effect. The superposed effective relaxation time τ_{eff} is given by:

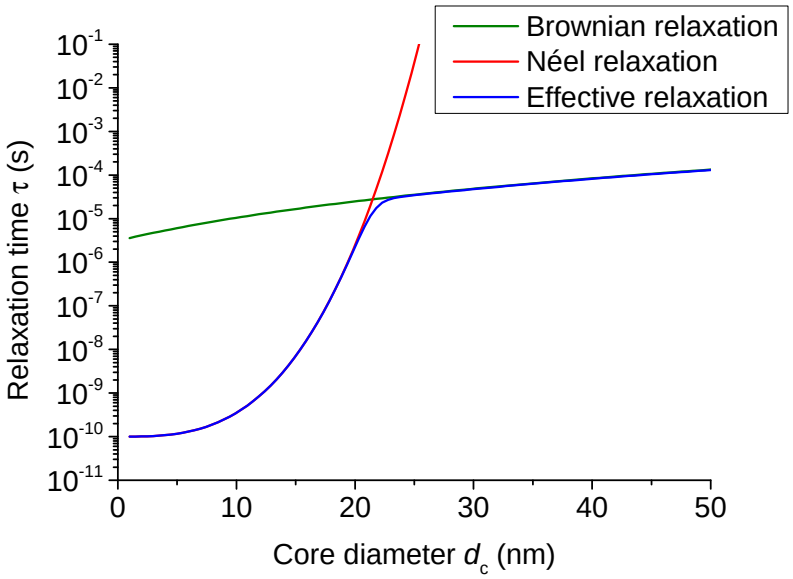

Figure 7: Superposition of Brownian and Néel relaxation.

$$\frac{1}{\tau_{\mathrm{eff}}} = \frac{1}{\tau_{\mathrm{N}}} + \frac{1}{\tau_{\mathrm{B}}}. \tag{2.11}$$

Both relaxation mechanisms as well as the effective relaxation time are visualized in Fig. 7 for an anisotropy constant $K = 10000\,\mathrm{J/m^3}$, a temperature of $T = 293.15$ K, the viscosity of water $\eta = 10^{-3}\,\mathrm{Pa{\cdot}s}$, a hydrodynamic shell thickness $d_{\mathrm{h}} = 10$ nm, and therefore a hydrodynamic diameter $D_{\mathrm{h}} = d_{\mathrm{c}} + 20$ nm.

It can be seen that Néel relaxation is most prominent in smaller nanoparticles while Brownian relaxation can mostly be observed in larger particles, given they can rotate freely. Next, how the relaxation mechanisms influence the particle magnetization will be presented.

2.1.6. Susceptibility and complex susceptibility

The magnetization of every magnetic material is described by the susceptibility χ via:

$$M = \chi H. \tag{2.12}$$

To take the relaxation dynamics and the resulting time lag between excitation and particle response into account, the Debye Model [20] can be used to split χ into a real part χ' and an imaginary part χ'', yielding [86]:

$$M_{\mathrm{dyn}}(t) = (\chi' + i\chi'')M_{\mathrm{stat}}(H) \tag{2.13}$$

with:

$$\chi'(\omega) = \frac{\chi_0}{1 + (\omega\tau_{\mathrm{eff}})^2}, \tag{2.14}$$

and:

$$\chi''(\omega) = \frac{\chi_0\omega\tau_{\mathrm{eff}}}{1 + (\omega\tau_{\mathrm{eff}})^2} \tag{2.15}$$

with $\omega = 2\pi f$ and f as the frequency of the excitation field. Here:

$$\chi_0 = \frac{\mu_0 n m^2}{3k_{\mathrm{B}}T} \tag{2.16}$$

where n is the number of particles.

Employing the parameters used in (2.11) and a magnetic core diameter $d_{\mathrm{c}} = 20$ nm, the complex susceptibility can be calculated via (2.14) to (2.16) (see Fig. 8).

It can be seen in this example, that for lower frequencies, the susceptibility solely consists of the real part since the particles still follow H nearly instantaneously. At some point, the imaginary part becomes more prominent indicating a time lag

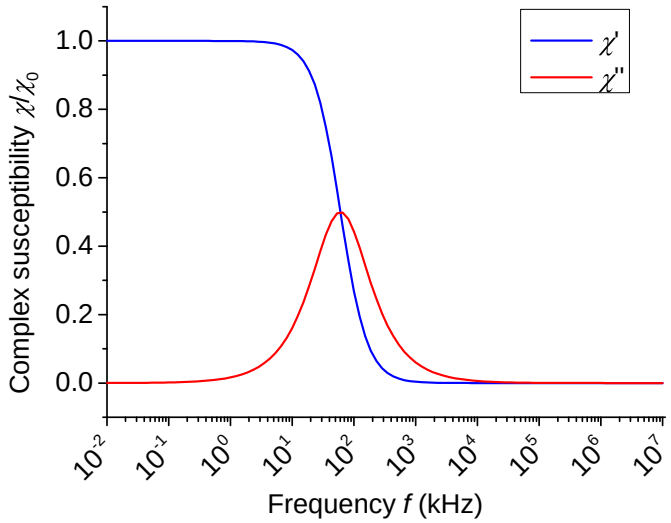

Figure 8: Complex susceptibility χ' and χ" for $d_c = 20$ nm.

between magnetization and magnetic field strength. Here, the imaginary part of the susceptibility χ" reaches its maximum at $f \approx 65$ kHz, corresponding to the relaxation time $\tau(d_c = 20\,\text{nm}) = 1/f = 15\,\mu\text{s}$ in Fig. 7. This frequency is called the characteristic frequency f_{char} of the particle. At higher frequencies, the particles in this example are not able to follow the field and the real and imaginary part of the susceptibility both drop to zero.

2.1.7. Field dependent relaxation

So far, the relaxation times, and thus the complex susceptibility, were treated as independent of the external magnetic field strength. Yet, it seems obvious that the influence of the external field on the magnetic moment influences the Brownian motion of the whole particle as well as the reorientation of the magnetic moment via Néel [21]. When both expressions were first derived by Brown and Néel, the behavior of single domain particles was to be explained without or with only a weak external field, i.e., the influence of thermal fluctuation and anisotropy on an ensemble of single domain particles. Hence, the term relaxation makes sense as both mechanisms explain how single domain particles relax from a state of order into a random chaotic state. However, the term no longer fits when particle behavior with applied magnetic fields is described. In this context, the term *rotational dynamics* seems to fit better.

Among others, the field dependency of the Brownian reorientation has been demonstrated by Chemla et al. [17]. Based on the Fokker-Planck-Equation, Yoshida and Enpuku performed numerical simulations to derive a phenomenological term for the Brownian rotational dynamics [145] [146]. They proposed the equation:

$$\tau_{\mathrm{B,H}} = \frac{\tau_{\mathrm{B}}}{\sqrt{1 + 0.126\xi^{1.72}}} \tag{2.17}$$

which only depends on the zero field relaxation time and the argument of the Langevin Function ξ and thus makes this expression easily usable for simulations in AC fields.

First indications regarding the field dependency of the Néel time are given by Chantrell et al. [16] and was further developed by Ludwig et al. [87]. Here, the shift in the energy landscape induced by the external magnetic field is taken into account, yielding for the Néel relaxation dynamics:

$$\tau_{\mathrm{N,H}}(H) = \tau_0 \mathrm{exp}\left[1 - 2\frac{H}{H_A}(\mathrm{cos}\psi + \mathrm{sin}\psi) + \left(\frac{H}{H_A}\right)^2\right] \tag{2.18}$$

where $\psi = \varphi - \theta$ is the angle between external field and magnetic moment and H_{A} is the anisotropy field. Based on these insights, a phenomenological expression similar to (2.17) has been derived by Dieckhoff et al. [23] and is given by:

$$\tau_{\mathrm{N,H}} = \frac{\tau_{\mathrm{N}}}{\sqrt{1 + 1.97\xi^{3.18}}}. \tag{2.19}$$

The two expressions for Brownian and Néel rotational dynamics are visualized in Fig. 9. It can be seen that the Néel rotation drops much faster than the Brownian rotation. This indicates that even particles that mainly follow the Brownian rotational mechanics might switch to primarily Néel rotation at higher excitation fields, which is an important insight for the research on medical applications of particles that are to be used in highly viscous environments like blood.

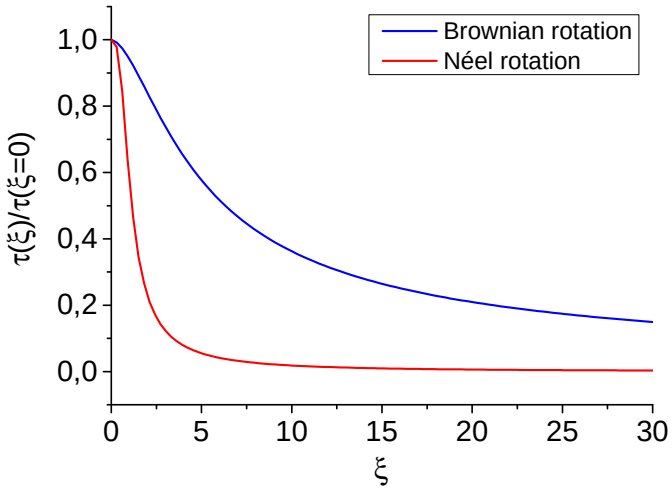

Figure 9: Normalized rotational dynamics for Brownian and Néel rotational dynamics. Néel rotation tends to drop much faster than Brownian rotation.

The final section of the introduction into MNP will cover the influence of the whole suspension on particle behavior.

2.1.8. Composition of Magnetic Nanoparticles

For the characterization of MNP as MPI tracers, it is important to not only consider the magnetism of the particle core but to consider the whole system, consisting of core, hydrodynamic shell, and the suspension medium. This becomes apparent considering the respective influences on the magnetic behavior. While the magnetic moment and the anisotropy axis of the particle depend on the size and structure of the core, the behavior of relaxation dynamics also strongly depends on the hydrodynamic shell and the suspension medium.

The coating of magnetic cores with a hydrodynamic shell is an important step in the synthesis process of MNP to prevent agglomeration and eventual sedimentation. A second reason for the coating of MNP is their susceptibility to oxidation and therefore instability in their properties as well as biocompatibility [129]. This process is especially important for pure metals like iron, cobalt, and nickel [84]. The coating not only keeps the particles in a colloidally stable state, it also opens up possibilities to functionalize the particles [105] [96] by attaching therapeutic agents or additional

imaging markers [133]. Biocompatible coatings include monolayer ligands, polymers like dextran, and silica coatings [100].

The hydrodynamic shell of the particles influences their behavior, especially in the regime of Brownian relaxation, as can be seen in (2.10). Particles, whose moments are blocked, rotate via the Brownian mechanism. This mechanism also includes the shell, which rotates together with the particle core. Therefore, a large hydrodynamic diameter may significantly slow τ_B but may be necessary to keep the MNP colloidally stable. To this point, the particles have been treated as single, nearly spherical

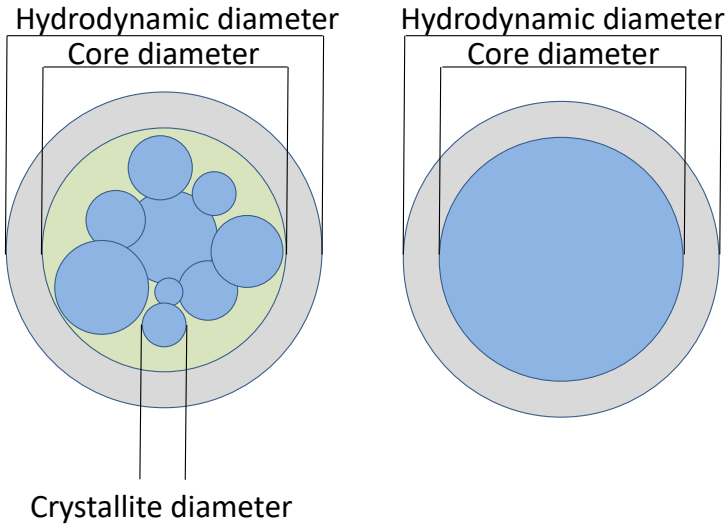

Figure 10: MNP are composited of the particle core and the hydrodynamic shell. The core may be composited of several small crystallites to form a multicore particle (left) or one large crystallite to form a single core particle (right) according to [10].

.

cores inside hydrodynamic shells (Fig. 10 right). Assuming uniaxial anisotropy, this single core particle consists of one so-called crystallite [10], which is the ensemble of aligned magnetic moments. Besides these single core particles, so-called multicore particles are a widely used particle type [147] [77]. Here, the particle core consists of several crystallites that are clustered in one hydrodynamic shell (Fig. 10 left). Consequently, this composition influences the time scales of the Néel rotational behavior since the reorientation of the particles magnetic moment occurs separately for each crystallite. As the reorientation time for smaller particles is faster than

for larger particles (see Fig. 7), it is suspected that multicore particles with large net magnetic moments composed of several smaller crystallites might be a suitable particle type for high-frequency applications like MPI [27].

Still, it has to be considered that closely packed crystallites are strongly affected by dipolar interaction [114], so that in addition to the anisotropy (2.2) and magnetic energy, the energy of the dipole-dipole interaction strongly affects these particles.

The third influencing factor on the magnetic behavior of MNP is the suspension. A suitable suspension medium is not only crucial for the stability and biocompatibility of MNP, the viscosity in which the particles are suspended directly influences the Brownian motion as can be seen in (2.10). This should be kept in mind, especially when Brownian particles are used in blood.

It can be concluded that the behavior of MNP in a magnetic field depends on several different aspects ranging from internal structure to external influences, like suspension medium or magnetic field strength. All of these influences will eventually more or less affect the image quality in a medical setup. However, before it can be further discussed how MNP affect the image quality, the term itself and means to measure need to be introduced.

2.2. Image quality

Many diagnoses and medical decisions depend upon the results of medical imaging. The accuracy of anatomical or functional information is roughly condensed under the term *image quality*. This represents a general judgment about the quality of a medical image and is often associated with contrast and spatial resolution [125] [15] [18].

The aim of this thesis is to investigate the relationship between image quality in the sense of spatial resolution and tracers in MPI. In this chapter, the term *image quality* as well as the basic concepts of its quantification are reviewed in the sense of medical imaging.

2.2.1. Point Spread Function

The generally accepted definition of spatial resolution is the minimum size of an object that can still be imaged or the minimum distance between two lines that can still be resolved in an imaging system [15]. Following this concept, the fundamental limit of the resolution in every digital imaging system is the pixel size (Fig. 11). Even though it may still be possible to detect and image an object smaller than this limit, it will only be imaged by filling out the whole pixel. Yet, this concept is just the technical limit of imaging systems, presuming that the object is not located between two pixels and that the system is capable of perfectly imaging the object without any loss of information.

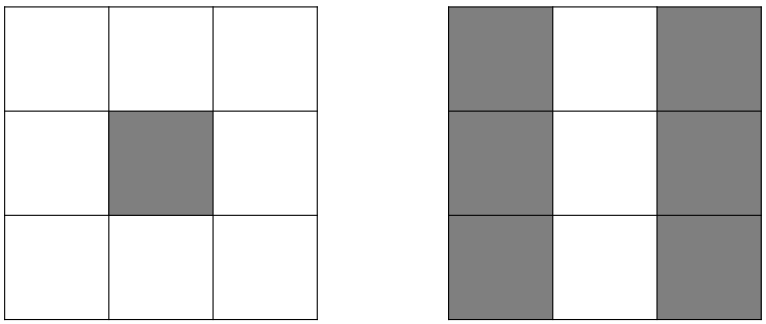

Figure 11: The pixel size as the fundamental resolution limit. Left: The center pixel is completely filled and is therefore the smallest resolvable unit of the imaging system. Right: Two lines are one pixel apart from each other and have the minimum resolvable distance from each other.

In reality, medical imaging systems often suffer from a blurring effect in the acquired image compared with the imaged object. The reason is the PSF or impulse response, which describes the relationship between a point-like object in the center of the Field of View (FOV) and the corresponding image. It is mathematically described by the convolution, which is given by the equation:

$$k(x) = \int_{-\infty}^{\infty} h(x)g(x - x')dx' = (h * g)(x) \tag{2.20}$$

with the imaged object g, the PSF h, and the final image k. The convolution can be understood as the superposed blurring or smearing effects for all imaged objects in the FOV. A symmetric PSF is depicted in Fig. 12. In the top row it can be seen how the PSF widens a point-like input directly in the center of the image. The output in this case is equivalent to the PSF. Correspondingly, Fig. 12 (bottom) depicts the effect of the PSF on two point-like inputs next to each other. It is noticeable that the signal between the inputs in the image k is not fully reduced to zero. The PSF of this example would therefore slightly reduce the contrast between the two inputs.

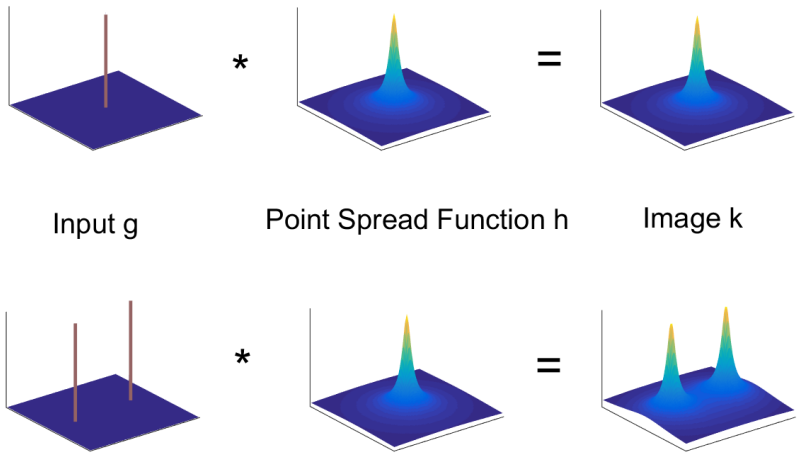

Figure 12: The image k is the convolution of the input g and the convolution kernel or Point Spread Function h.

This effect limits the achievable spatial resolution as two point-like sources can only be resolved if their superposed signals still exhibit two separate peaks. This principle is visualized in Fig. 13. Here, the dashed lines depict the point-like objects, the red and blue lines are the corresponding PSFs and the black line is the output signal, consisting of the superposed PSFs. In Fig. 13 (left), the distance between the two objects is large enough so that they can easily be resolved. In Fig. 13 (middle), the objects are getting closer and the single peaks begin two merge. Here, the

output signal is barely recognizable as being composed of two separate peaks. At this point, the distance between the objects corresponds to the width of the PSF at 50% of its height and is recognized as a typical measure for the spatial resolution of imaging systems, called Full Width at Half Maximum (FWHM) [125] [15]. For objects closer than the FWHM like in Fig. 13 (right), the system responses of the objects superpose each other to a signal with only one major peak, making it impossible to distinguish the objects from each other in the resulting image.

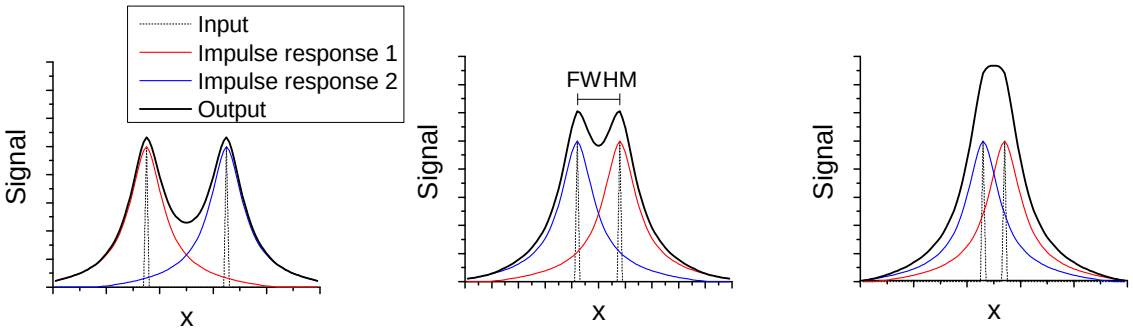

Figure 13: Two point-like objects can still be distinguished if their distance is at least the width of the Point Spread Function at 50% of its height. Left: Point-like objects that can easily be resolved. Middle: Objects at the resolution threshold that can barely be resolved with the object distance corresponding to the Full Width at Half Maximum. Right: The Objects can no longer be resolved.

2.2.2. Modular Transfer Function

An equivalent to the convolution can be found in the frequency domain, where it is described as a multiplication:

$$K(f) = H(f)G(f) \tag{2.21}$$

where $H(f)$ and $G(f)$ are the Fourier transforms of a convolution kernel h, an input g and the spatial frequency $f = 1/l_{\text{fov}}$ with l_{fov} as the length of the FOV. The Fourier transformation of a signal $s(x)$ with $x = [0, l_{\text{fov}}]$ is given by:

$$S(f) = \int_{-\infty}^{\infty} s(x)\exp\left(-2\pi i f x\right) \mathrm{d}x \tag{2.22}$$

where $i = (-1)^{1/2}$. The Fourier transformation is employed to describe any periodic signal as a sum of sine functions:

$$s(x) = \sum_{n=0}^{N} a_n \sin(2\pi n x f + \varphi_n) \tag{2.23}$$

where a_n is a vector of Fourier coefficients (which is usually called the harmonic spectrum) and φ_n is the vector of phase shifts for the sine component. The principle is visualized in Fig. 14 with $N = 7$.

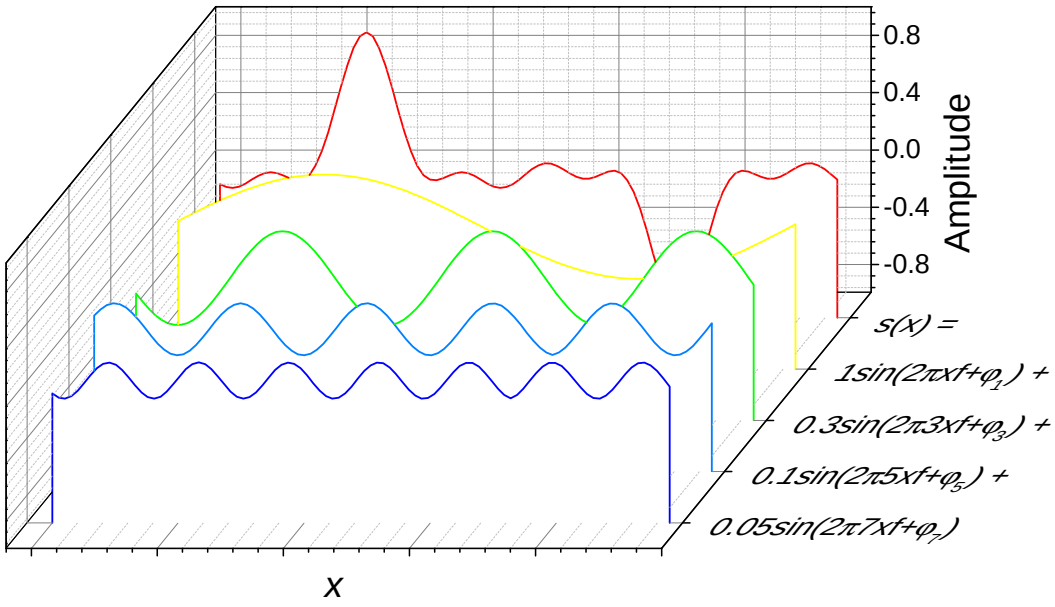

Figure 14: A signal $s(x)$ (red) can be decomposed into a sum of sine functions. The amplitudes of the sine functions correspond to the Fourier coefficients a_n and form the harmonic spectrum.

Spatial frequencies are usually expressed in line pairs or cycles per millimeter [12] [125] [15] and describe the number of periods of a frequency per length. The normalized Fourier coefficients a_n/a_0 of the Fourier transformed PSF $H(f)$ plotted over the spatial frequencies is called the Modulation Transfer Function (MTF).

The name of the MTF is derived from the way it modulates the frequencies of an input $G(f)$. As per equation (2.21), the MTF is multiplied with the input distribution of objects in frequency domain where the spatial frequencies of the input are modulated accordingly. Thus, an amplitude in the MTF of 0.4 means a reduction of the input amplitude of the respective spatial frequency in the output to 40%.

Just like the PSF, the MTF can also be used as a measure for the maximum achievable spatial resolution [12]. While the PSF describes the relationship between imaging input and output in the spatial domain, the MTF describes this relationship in the frequency domain.

Typically, a coefficient is defined when the signal damping becomes too strong to resolve a sinusoidal input of the given spatial frequency (see Fig. 15). This may be 10% [15], but also other values like 3% or 5% have been proposed [125]. The corresponding value on the x-axis then defines the maximum resolvable spatial frequency, which is the inversion of the highest achievable spatial resolution.

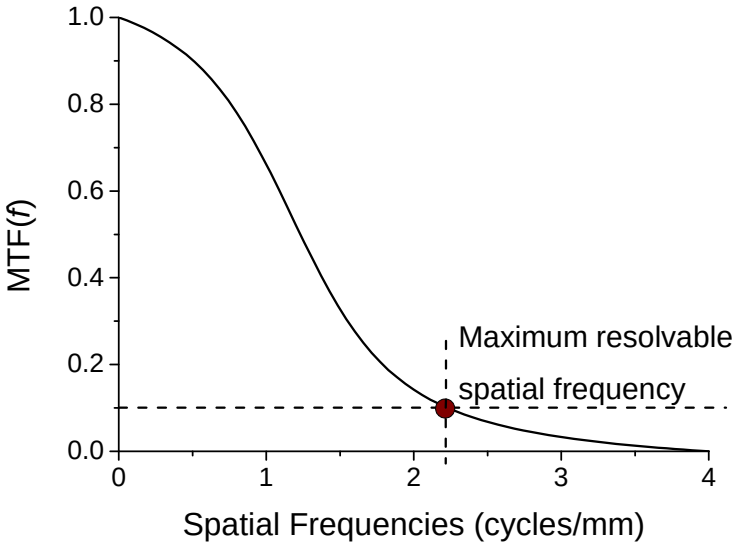

Figure 15: The MTF describes the signal damping over the spatial frequency. A typical measure for the spatial resolution is to set a maximum damping coefficient that still allows two objects of the corresponding distance to be resolved. In this case, the coefficient is 0.1.

Two criterions for the resolution, one in the spatial and one in the frequency domain have been presented in the previous section. The next section will introduce a prerequisite for the acquisition of spatial frequencies.

2.2.3. Nyquist frequency

The Nyquist frequency, based on the Nyquist-Shannon sampling theorem, is a fundamental law in the field of signal processing [122]. While the MTF describes the loss in contrast for higher spatial frequencies depending on the transfer function, the Nyquist frequency describes the number of sampling points needed to measure a certain frequency in time or space and is given by:

$$f_{\text{sample}} > 2 f_{\text{signal}}. \tag{2.24}$$

Thus, the frequency of the discrete number of sample points (or sample rate) must be greater than twice as high as the frequency of the measured signal. Depending on the imaging system, f_{sample} may refer to the bandwidth of the detector or to the density of detector elements. The latter applies to Charge-Coupled Device (CCD) sensors, for example. The impact of violating and satisfying (2.24) can be seen in Fig. 16.

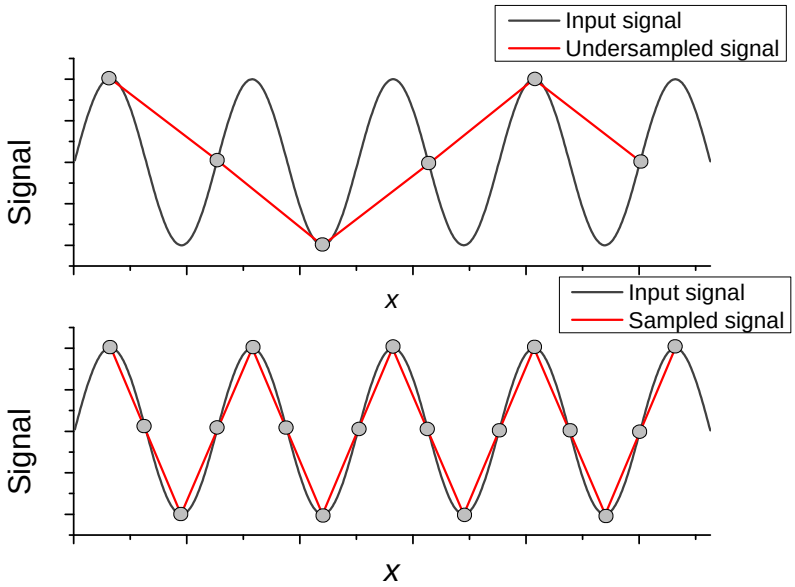

Figure 16: Top: Sampled signal with six detector elements. The signal is undersampled resulting in an underestimated frequency, called aliasing. Bottom: Sampled signal with nine detector elements, which satisfies the Nyquist criterion.

Here, an input signal of 4.5 periods is sampled with a detector consisting of 6 (top) and 17 (bottom) detector elements. The latter satisfies the Nyquist criterion, while the former violates it. Consequently, the input signal is undersampled and seems to have a much lower spatial frequency, a so called aliasing effect. By contrast, 17 detector elements satisfy the Nyquist criterion (2.24) and the input signal is sampled with the same spatial frequency. This principle can also be interpreted from an imaging point of view. When treating the input signal as a sinusoidal distribution that is to be imaged, a spatial frequency that meets the requirements of the Nyquist frequency is necessary. If the bandwidth of the detector is somehow limited and incapable of providing the needed spatial frequency (here given by the number of detector elements), this distribution cannot be imaged without a loss in resolution.

The Nyquist criterion is therefore only an indirect measure for the resolution; however, as discussed later in this thesis, it highly influences the image quality in MPI.

In the following section, the experimental systems, particularly MPI itself, will be explained.

2.3. Experimental systems

In this chapter, the fundamentals of MPI as well as the MNP characterization techniques MPS and Magnetic Properties Measurement System (MPMS) will be introduced. As the main topic of the thesis is MPI, it will comprise the largest part of this chapter. The section regarding MPI will first cover the basic principle of signal generation and spatial encoding. It will then be followed by an overview of the two main reconstruction principles in the time and frequency domains and end with additional implications for the imaging process in 2D and 3D. Since the principle of signal generation in MPS is very similar to MPI, the section about MPS will cover primarily, how it is employed as a technique to characterize the tracer performance for MPI. In the section about MPMS, it will be described how it is employed to measure MNP in a field regime of up to several Tesla and how the measurements are employed to reconstruct the size distribution of the measured tracer.

2.3.1. Magnetic Particle Imaging

MPI is an imaging modality that enables the quantitative detection of MNP that are employed as tracer material. It was developed at Philips Research Hamburg and first published in Nature in 2005 [39]. The next milestone in the development of MPI was the first report of three dimensional, real time *in vivo* imaging of a beating mouse heart in 2009 [142]. At this time, the image reconstruction in MPI was only possible in frequency space. This changed in 2010 and 2011, when the X-Space formulation of MPI was published, first for 1D [42] and later for 2D and 3D images [43]. This formulation enabled the direct image reconstruction in space based on the PSF. The latest significant step in the development process of MPI was the multi-color MPI to distinguish different binding states of one tracer or of different tracers from each other in the reconstruction process in 2015 [107].

To date, MPI has been used for monitoring MNP based hyperthermia [97], imaging of sentinel lymph node biopsy [50], and in-vivo vascular imaging [142].

In the following chapter, the fundamentals of this imaging technology will be reviewed from basic signal generation over spatial encoding to reconstruction principles.

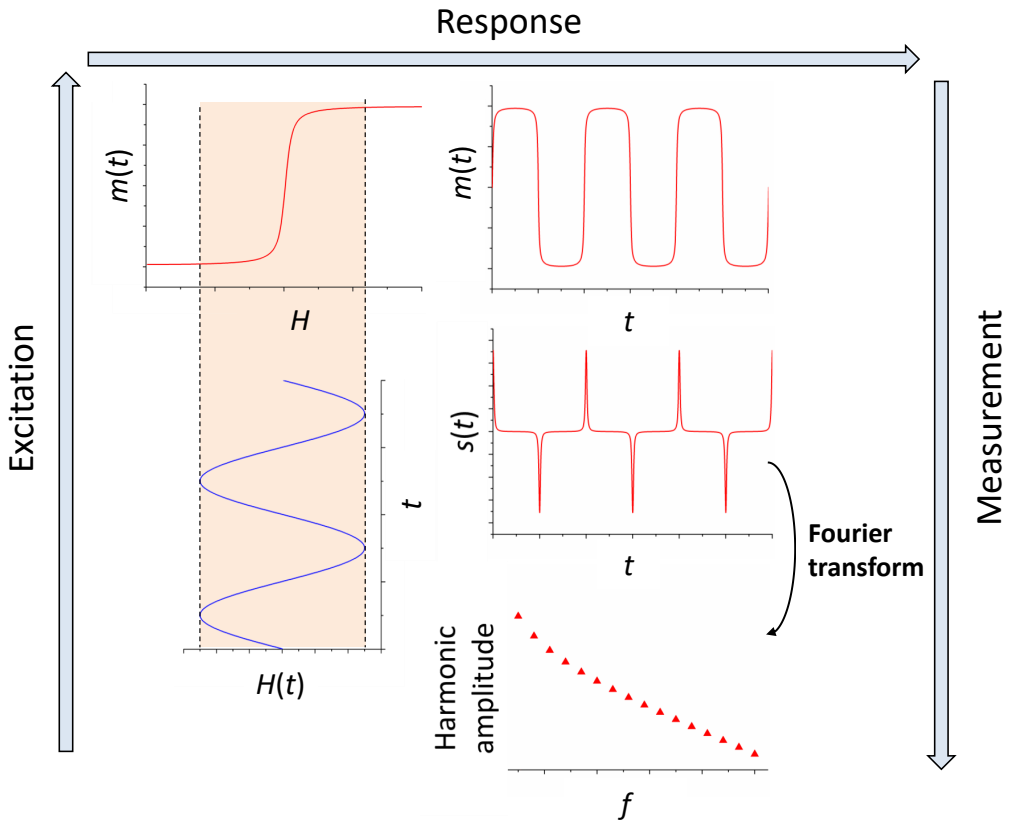

Figure 17: Signal generation in MPI according to Rahmer et al. [108]. Clockwise from bottom left to bottom right: The oscillating magnetic field periodically magnetizes the particles that exhibit a nonlinear dynamic susceptibility, yielding a distorted oscillating magnetic moment. From the measurement signal $s(t)$, the characteristic harmonic spectrum is derived and the fundamental frequency (blue) is filtered out.

2.3.1.1. Basic principle Fig. 17 illustrates the fundamental principle of MPI. When MNP are exposed to an oscillating external magnetic field $H(t)$ (the drive field, which operates at up to 25 mT) with a frequency f, the particles are periodically magnetized (left) yielding an oscillating net magnetic moment $m(t)$ of the ensemble (top right). Due to the nonlinear shape of the dynamic susceptibility, the oscillating magnetic moment is distorted compared with the sinusoidal excitation. This particle induced distortion results in a moment that now not only oscillates with f, but also with a set of higher harmonics. Induction coils are employed to measure the magnetic moment, so the total MPI signal can be derived according to Knopp [72]: The induced voltage due to Faradays law is based on the time derivative

of the magnetic flux density B, integrated over the surface of the pickup coil:

$$u(t) = \oint_{\partial A} \vec{E} d\vec{l} = -\int\int_{A} \frac{\partial \vec{B}}{\partial t} dA. \tag{2.25}$$

In MPI, the total magnetic flux density inside the pickup coil comprises not only the magnetic field generated by the magnetized tracers, but also the drive field. Since the drive field is harmonic over the whole FOV including the pickup coils, its contribution to the overall induced voltage can easily be calculated using (2.25) and $B = \mu_0 H_{\text{Drive}} \sin(\omega t)$.

To describe the voltage induced by the field that is generated by the magnetized tracers, the law of reciprocity is applied, stating that the receive properties of a coil are the same as their field generating properties. The induced voltage is then expressed via an integral over the volume V of the FOV via:

$$u(t) = -\mu_0 \int_V \frac{\partial}{\partial t} \vec{M}(\vec{r}, t) p(\vec{r}) d^3\vec{r} \tag{2.26}$$

with $\vec{M}$ being the particle magnetization and $p(\vec{r})$ being the coil sensitivity as a function of the location in the FOV (A detailed derivation of the coil sensitivity via the Biot-Savart Law can be found in [72]). Hence, in MPI the differential of the particle magnetization as well as the differential of the drive field are measured (Fig. 17 right).

Since the drive field is approximately five decimal powers higher than the system response of the MNP, the first harmonic is filtered using highpass filters. This leads not only to the suppression of the voltage fraction induced by the drive field, but also to the suppression of the first harmonic of the particle response. The measurement signal can therefore be expressed as:

$$u(t) = u^M(t) = -\mu_0 \int_V \frac{\partial}{\partial t} (\vec{M}(\vec{r}, t) - \vec{M}_1(\vec{r}) \sin(\omega t)) p(\vec{r}) d^3\vec{r} \tag{2.27}$$

with $\vec{M}_1(\vec{r})\sin(\omega t)$ as the suppressed first harmonic of the magnetization. For the imaging process, usually the harmonic spectrum beginning with the third harmonic (Fig. 17 bottom right) is employed.

2.3.1.2. Spatial encoding The spectrum alone does not yield a spatial resolution, as there needs to be a way to distinguish the superposed signals from each other that are generated by tracers at different locations. Therefore, an additional field is introduced (selection field) generated by two Maxwell coils. These Maxwell coils generate a linear field gradient G between each other, resulting in a distinct offset field $H_{\text{off}}(x) = -G/\mu_0 x$ in the field of view depending on the location x.

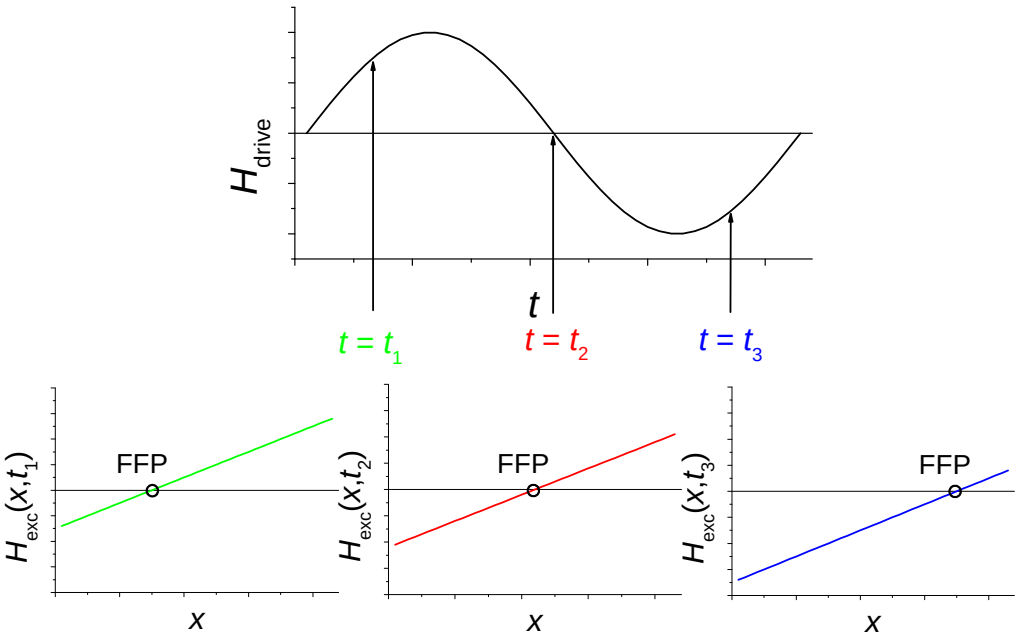

Figure 18: Signal superposition of drive field $H(t)$ (top) and selection field $H_{\text{off}}(x)$ over the field of view (bottom) at different times t. The field superposition generates a field free point (FFP) moving through the field of view.

Fig. 18 depicts the superposition of both drive field and selection field over the FOV at three different times $t = t_i$. This superposition yields the resulting magnetic field:

$$H_{\text{exc}}(x,t) = H_{\text{Drive}}(t) - Gx/\mu_0 = H_{\text{Drive}}(t) + H_{\text{off}}(x) \tag{2.28}$$

and therefore a different alternating excitation field at every location in the FOV.

This results in the movement of a Field Free Point (FFP) through the FOV, whose position is varied via the time dependent drive field. Consequently, tracers at different locations in the FOV are influenced by different magnetic fields.

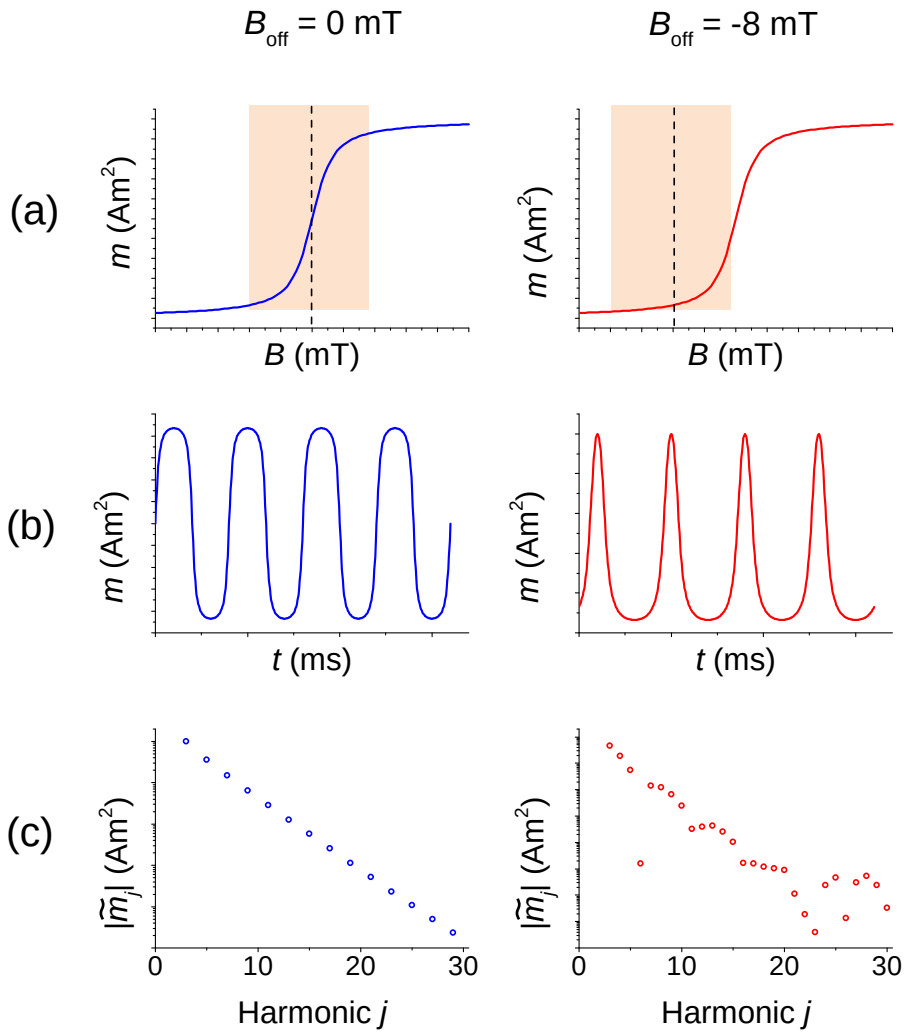

Figure 19: MPI signal generation. (a) The scanned regime of the dynamic susceptibility; (b) The resulting magnetic moment of tracers at different locations in the FOV; (d) Fourier spectrum of the measurement signal.

The effect on the signal generation of different magnetic fields at every location can be seen in Fig. 19. The colored area in (a) depicts the covered excitation field regime $B_{\text{exc}}(x,t)$ of the magnetization curve without offset field B_{off} (left), the situation usually at the center of the FOV, and with an applied negative offset field (right), respectively. Fig. 19 (b) depicts the resulting net magnetic moment $m(t)$ of the tracer as a consequence of the excitation $B_{\text{exc}}(x,t)$. To suppress spurious signals

of the drive field in the detector, the fundamental frequency f_1 is filtered out, also removing the first harmonic of the magnetic moment. Lacking the full information on the measured magnetic moment, a Fourier Transformation is performed and the magnetic is evaluated in frequency domain (c) without f_1. It can be seen, that for field offset $B_{\text{off}} = 0$ mT, the even harmonics vanish due to the symmetry of the magnetization curve, whereas additional even harmonics occur for nonzero field offsets (green dots in (c)). These different spectra at different offset fields are exploited to reconstruct the particle distribution from the overall measurement signal. This reconstruction process will be explained in more detail in the next sections.

2.3.1.3. Frequency domain reconstruction The reconstruction in the frequency domain is called the system matrix reconstruction. The name is derived from the system matrix (or transfer function) $\mathbf{A}$ that describes the response of the system in frequency domain to a point source (a zero dimensional particle distribution, i.e., delta distribution) for every discrete spatial position $\vec{r}$ in the FOV. This leads to a matrix with the size $n \times m$ with n as the number of voxels in the FOV and m as the number of harmonics. In vector form, the overall relationship between system function and measurement signal s can be written as:

$$\mathbf{A}N_{\text{p}}(\vec{r}) = s \tag{2.29}$$

with $N_{\text{p}}(\vec{r})$ as the amount of particles as a function of the location, also called the spatial tracer distribution. The signal of a point-like source of MNP at the given location $\vec{r} = \vec{r}\,'$ in the FOV can be written according to (2.27) and the relationship:

$$\int_{-\infty}^{\infty} f(\vec{r})\delta(\vec{r} - \vec{r}\,')dx = f(\vec{r}\,') \tag{2.30}$$

as:

$$s(t, \vec{r}\,') = -\mu_0 \frac{\mathrm{d}}{\mathrm{d}t}\vec{M}_{\text{filter}}(t, \vec{r}\,')p(\vec{r}\,') \tag{2.31}$$

with $\vec{M}_{\text{filter}} = \vec{M} - \vec{M}_1 \sin(\omega t)$ and δ as a delta distribution. Thus, the corresponding row of the system matrix can be obtained by the Fourier transformation $\mathcal{F}$ of the

signal and normalization to the particle amount:

$$A(f, \vec{r}\,') = \frac{\mathcal{F}(s(t, \vec{r}\,'))}{N_{\mathrm{p}}(\vec{r}\,')}. \tag{2.32}$$

Inserting the Langevin function (2.3) into (2.31), a system function can be modeled for demonstration purposes (Fig. 20).

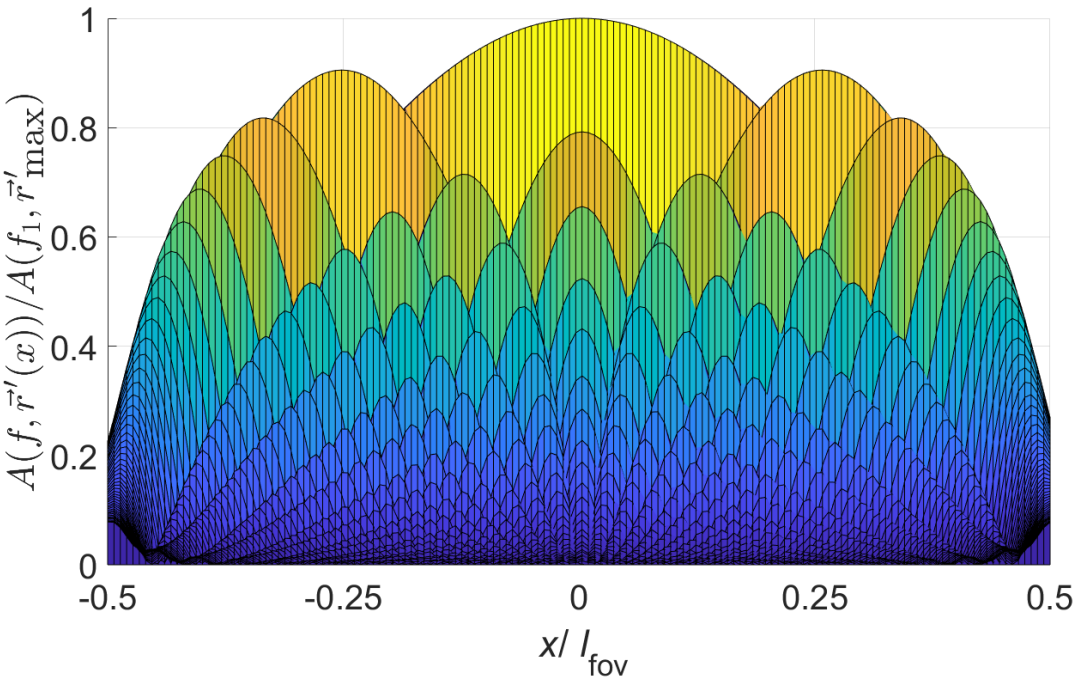

Figure 20: System matrix modeled via Langevin function. The depicted waves correspond to the harmonic amplitudes at each location in the normalized FOV. The harmonic spectra seen earlier are therefore orthogonal to x and m. The color map only indicates the strength of the harmonic amplitude and is used to distinguish the values from one another.

Here, the harmonic amplitudes are depicted for the 1D case over the normalized FOV. The harmonic axis in this picture is orthogonal to the x- and y-axis and not visible. The depicted waves are the absolute harmonic amplitudes beginning with the first harmonic f_1 in the background (which is usually filtered out) to the higher harmonics in the foreground. The color map only indicates the strength of the

harmonic amplitude and is used to distinguish the values from each other. These spectra form the set of base functions out of which s is composed. In the ideal case of particles behaving purely according to the Langevin function, the distinct form of the curve shape of each harmonic amplitude over the FOV can be modeled using Chebyshev polynomials of the second kind [108] [85], which will be further elucidated in section 4.3.

The particle distribution $N_\mathrm{p}(\vec{r})$ can be reconstructed by solving the least squares problem:

$$\mathbf{I}N_\mathrm{p}(\vec{r}) = \mathbf{A}^{\oplus}s \tag{2.33}$$

where $\mathbf{I}$ is the identity matrix that is derived from the multiplication of $\mathbf{A}^{\oplus}\mathbf{A}$ with $\mathbf{A}^{\oplus}$ as the Moore-Penrose pseudoinverse of $\mathbf{A}$.

It should be mentioned here that the solution of the least squares problem does not usually lead to a satisfying result. Not only is the inverse problem highly ill-conditioned, the measurement vector is also composed not only of the particle signal, but also of a significant noise contribution $s = s_\mathrm{particle} + s_\mathrm{noise}$. This gives rise to the need of regularization [76].

The most common approaches for regularization are based on the manipulation of the singular values (the square root of the eigenvalues) of the system function, thereby suppressing signal components that are too heavily contaminated by noise. Such approaches are mostly based on the Singular Value Decomposition (SVD), like the truncated SVD or the Tikhonov regularization. The SVD is given by:

$$\mathbf{A} = \mathbf{U}\mathbf{\Sigma}\mathbf{V}^* \tag{2.34}$$

where $\mathbf{A}$ is the system function with $n \times m$ entries and rank l, $\mathbf{U}$ is an $m \times m$ unitary matrix, $\mathbf{\Sigma}$ is a sparse $m \times n$ matrix with the only non zero entries being the singular values of $\mathbf{A}$ on the main diagonal and $\mathbf{V}^*$ is the conjugate transpose of the unitary matrix $\mathbf{V}$. The Singular Value Decomposition enables a simple inversion of

the system function by inverting the singular values σ_i of $\mathbf{\Sigma}$:

$$\mathbf{\Sigma}^{\oplus}_{n,m} = \begin{cases} \frac{1}{\sigma_i}, & \text{for } i = j \leq l \\ 0, & \text{else} \end{cases} \tag{2.35}$$

and reconstructing the inverse system function $\mathbf{A}^{\oplus}$ via matrix multiplication. Since the truncated SVD as well as the Tikhonov regularization are based on a weighting function applied on the singular values, the SVD is a commonly used approach in solving inverse problems [7]. The difference between the truncated SVD and the Tikhonov regularization is the weighting function applied on the singular values before inversion. While a cutoff value $k < l$ is set for the truncated SVD, where the singular values are set to zero, the weighting factor Γ for the Tikhonov regularization is calculated using:

$$\Gamma_i = \frac{\sigma_i}{\sigma_i^2 + \lambda^2} \tag{2.36}$$

with λ as a regularization factor. The resulting curve form of the weighting factors can be seen in Fig. 21. Due to the high computational speed, the iterative Kaczmarz

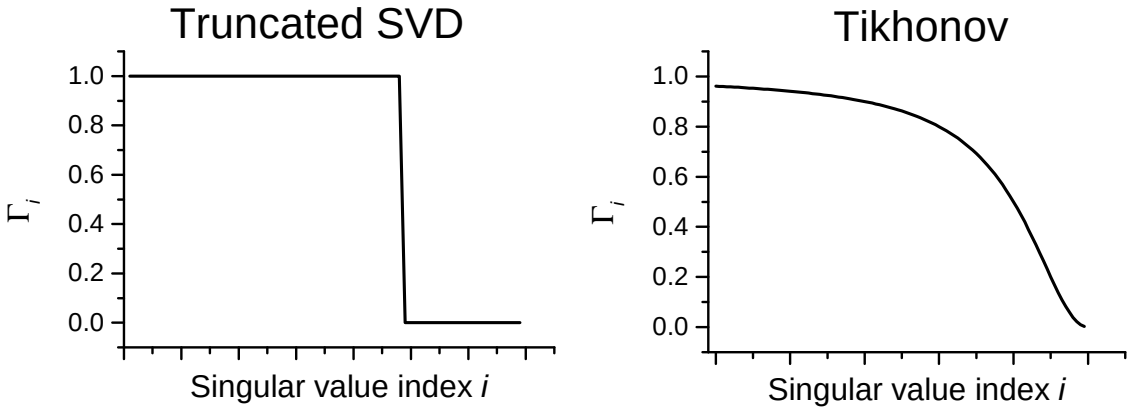

Figure 21: Singular value weighting factors of truncated Singular Value Decomposition compared with Tikhonov regularization.

algorithm [61] is a regularization approach commonly used in MPI (often in combination with the Tikhonov regularization) [142] [70] [106]. As the name suggests, the Kaczmarz algorithm is an iterative solver, following the relationship (for an $n \times m$ matrix with $m \geq n$ and m as the number of harmonics employed in reconstruction

and n as the number of voxels):

$$\vec{N}_{\mathrm{p},k+1} = \vec{N}_{\mathrm{p},k} + \lambda \frac{s_i - \langle \vec{a}_i, \vec{N}_{\mathrm{p},k} \rangle}{||\vec{a}_i||^2} \vec{a}_i, \text{with } i = (k \bmod m) + 1 \tag{2.37}$$

where k is the iterative step, s_i is the i-th measured harmonic of the MPI signal and a_i is a row from the system function, consisting of the responses of i-th harmonic over the FOV. The Kaczmarz regularization iteratively solves each equation of the linear system, which are interpreted as hyperplanes of the solution space [53]. Thus, every iteration consists of as many subiterations as there are harmonics in the reconstruction process and with every subiteration, the particle distribution is solved employing the i-th harmonic. Therefore, the total number of calculations is K iterations times m harmonics or subiterations.

The main advantage of the Kaczmarz algorithm is the reconstruction speed and its memory usage. While the complete system function has to be stored in memory for direct reconstruction methods, iterative methods consume much less memory due to the separate calculations for each row. Furthermore, iterative methods tend to be faster than direct methods. In this work, the Kaczmarz algorithm is used when reconstructing the particle distribution.

2.3.1.4. Time domain reconstruction The time domain reconstruction of MPI is based on the work of Goodwell and Conolly [42] [43] and was proposed under the term X-Space MPI. As the name suggests, it was derived to describe the theory of MPI and the reconstruction of the particle distribution in the time domain instead of the frequency domain to avoid the time consuming measurement of the system function. This is done via the description of the movement of the FFP that was visualized in Fig. 18 according to Goodwell. Based on the superposition of the time dependent drive field and the location dependent field gradient, the FFP location is described as:

$$x_s(t) = \frac{\mu_0 H(t)}{G}, \tag{2.38}$$

leading to the drive field dependent upon the FFP position:

$$H(x,t) = \frac{G(x_s(t) - x)}{\mu_0}. \tag{2.39}$$

Given the relationship $\Phi = \int BdA$ and assuming tracers only in x-direction, the magnetic flux inside the pickup coil generated by the magnetic field of sinusoidally magnetized monodisperse particles, each with the moment m, can be described as:

$$\Phi(t) = \mu_0 m \int p(x) c_{\mathrm{Fe}}(x) \mathcal{L}\left(\frac{\mu_0 m}{k_B T} G(x_s(t) - x)\right) dx \tag{2.40}$$

with $c_{\mathrm{Fe}}(x)$ as the location dependent concentration or particle density distribution. Using the convolution theorem (2.20) and Faraday's law of induction, equation (2.40) can be rewritten as:

$$s(t) = \mu_0 p(x) m c_{\mathrm{Fe}}(x) * \dot{\mathcal{L}}\left(\frac{\mu_0 m}{k_B T} G x\right)\Big|_{x=x_s(t)} \frac{\mu_0 m}{k_B T} G \dot{x}_s(t). \tag{2.41}$$

Finally, the image equation becomes:

$$\begin{aligned} \mathrm{IMG}(x_s(t)) &= \frac{s(t)}{\mu_0 p(x) m G \dot{x}_s(t) \frac{\mu_0 m}{k_B T}} \\ &= c_{\mathrm{Fe}}(x) * \dot{\mathcal{L}}\left(\frac{\mu_0 m}{k_B T} G x\right)\Big|_{x=x_s(t)} = (h * g)(x). \end{aligned} \tag{2.42}$$

As can be seen in (2.42), the image equation is expressed as the convolution of the particle distribution and the derivative of the Langevin function, which serves as the PSF $h(x)$ (see also section 2.2.1). The particle distribution can then be calculated by performing a deconvolution.

In the multidimensional case, the PSF must also be expressed as a two- or three-dimensional function. Without further derivation, the multidimensional PSF can be expressed as:

$$\begin{aligned} h(\vec{x}) =& \dot{\mathcal{L}}(||\xi||) \begin{pmatrix} G_x^3 x^2 & G_x G_y^2 xy & G_x G_z^2 xz \\ G_x^2 G_y xy & G_y^3 y^2 & G_y G_z^2 yz \\ G_x^2 G_z xz & G_y^2 G_z yz & G_z^3 z^2 \end{pmatrix} \frac{1}{H(x,y,z)^2} + \\ & \frac{L(||\xi||)}{||\xi||} \left(\begin{pmatrix} G_x & 0 & 0 \\ 0 & G_y & 0 \\ 0 & 0 & G_z \end{pmatrix} - \begin{pmatrix} G_x^3 x^2 & G_x G_y^2 xy & G_x G_z^2 xz \\ G_x^2 G_y xy & G_y^3 y^2 & G_y G_z^2 yz \\ G_x^2 G_z xz & G_y^2 G_z yz & G_z^3 z^2 \end{pmatrix} \frac{1}{H(x,y,z)^2} \right) \end{aligned} \tag{2.43}$$

with $||\xi|| = \frac{\mu_0 m}{k_B T}\sqrt{(G_x x)^2 + (G_y x)^2 + (G_z x)^2}$. The PSF in a two-dimensional image is depicted in Fig. 22. The specifics of the multidimensional X-Space MPI will not be elaborated any further at this point. A more detailed derivation can be found in [43].

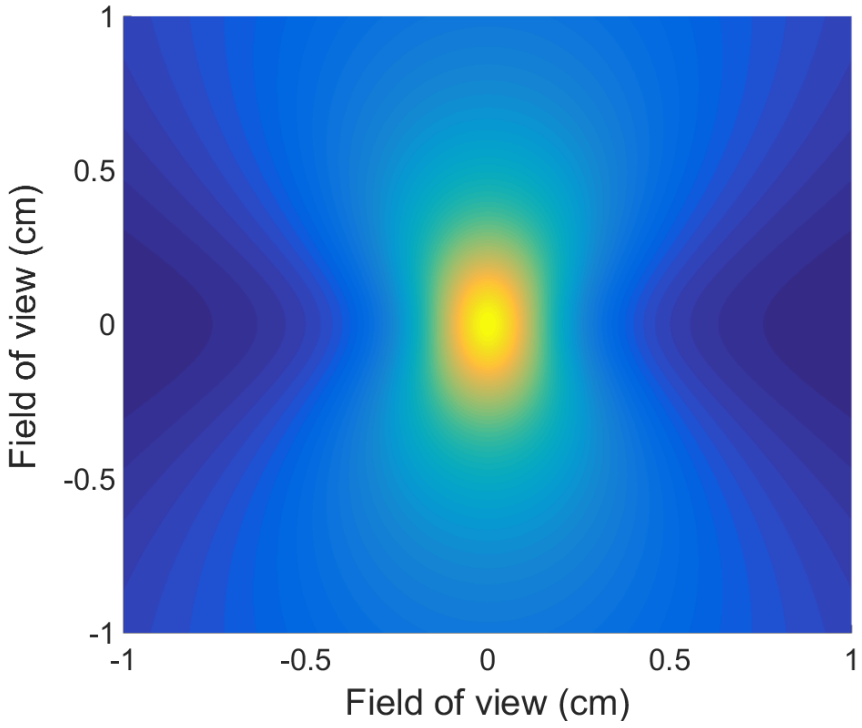

Figure 22: 2D Point Spread Function simulated for sequential acquisition for every single row.

2.3.1.5. Multidimensional MPI To understand the signal generation in MPI and, later on, the achievable resolution, it is of high importance to review the specifics of two- and three-dimensional MPI in the frequency domain. As shown in Fig. 19, the 1D encoding is achieved via a superposition of the time dependent drive field and location dependent field offset. To extend the spatial encoding from a line to a volume, it is necessary to introduce a second and a third drive field $H_{\text{Drive},y}(t)$ and $H_{\text{Drive},z}(t)$ as well as corresponding gradient fields $H_{\text{off},y}(x)$ and $H_{\text{off},z}(x)$. To move the FFP over the full FOV, the three drive fields are operated at different frequencies, for example, $f_{x,y,z} = (24.51, 25.25, 26.04)$ kHz [106]. While the movement of the FFP was just a movement along the FOV in 1D (Fig. 18), in 2D and 3D the FFP moves along a Lissajous trajectory based on the slightly different FFP velocities in each Cartesian direction (Fig. 23).

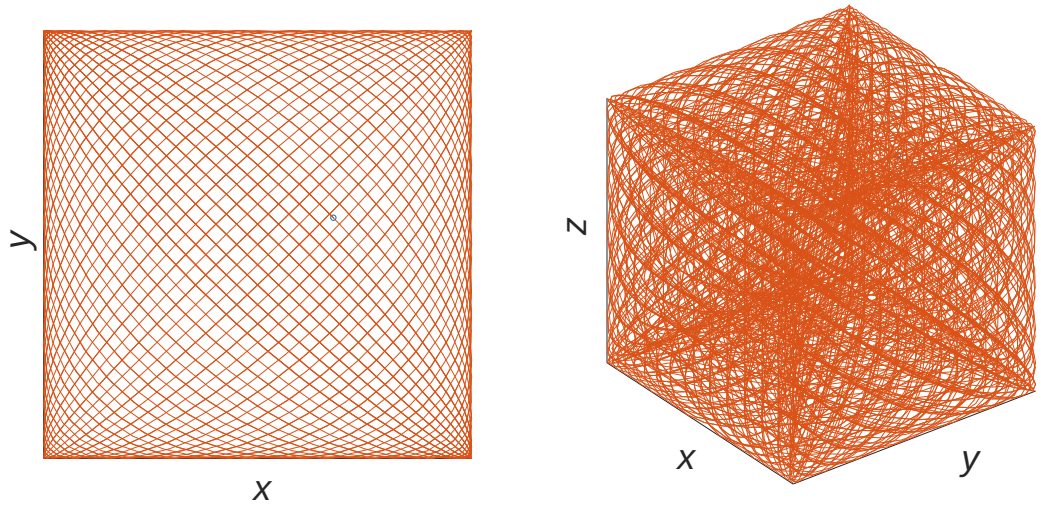

Figure 23: Left: Two-dimensional Lissajous trajectory pattern of the FFP; Right: Three-dimensional Lissajous trajectory pattern of the FFP.

This mechanism of simultaneous excitation with three different frequencies heavily influences the signal generation in MPI. While harmonics in 1D MPI occur at integer multiples of the excitation frequency, e.g., $f_i = (25.25, 50.50, 75.75, 101.00, ...)$ kHz for $f_{\text{Drive}} = 25.25$ kHz, mixed frequencies given by:

$$f = |n_x f_x + n_y f_y + n_z f_z| \tag{2.44}$$

must be taken into account for multidimensional MPI [109], where $n_{x,y,z} \in \mathbb{Z}$ is the n-th harmonic of the respective excitation frequency $f_{x,y,z}$. This is exploited in the reconstruction process as these mixed frequencies yield valuable additional information about the tracer distribution in the FOV.

In the following section, the zero dimensional MPI or MPS that serves as one of the most important devices for the characterization of MNP regarding their MPI performance will be addressed.

2.3.2. Magnetic Particle Spectroscopy

This section addresses the characterization of magnetic nanoparticles with MPS. MPS is widely regarded as one of the most established modalities for the characterization of MPI tracers [8] [91] [86] [127]. Since the basic principle of signal generation

is equivalent to MPI, the section concerning the principle of MPS will be kept short. More importantly, it will explain how MPS is typically used to characterize tracers in terms of their MPI performance.

2.3.2.1. Basic principle Lacking the gradient field and therefore the spatial resolution, MPS is the zero dimensional and thus, spectroscopic version of MPI. This makes it a very valuable tool to explore the spectral response of MNP in the environment found in MPI. Just as in MPI, the tracers are excited by a drive field H_{Drive} at a frequency f that corresponds to the parameters at which an MPI scanner is typically operated. The drive field periodically magnetizes the tracers, yielding a magnetic moment in the temporal characteristic of a distorted sinusoidal signal. Since inductive coils are used for signal acquisition, the time derivative of the particle moment $\mathrm{d}m/\mathrm{d}t$ is measured. To suppress signals of the drive field in the detector, the fundamental frequency f_1 is filtered out, which leaves the harmonic spectrum beginning with the third harmonic.

Due to the same signal generation principle, the amplitudes of the MPS signal are regarded as an indicator of the suitability of MPI tracers [8].

2.3.2.2. Characterization of MPI tracers Lacking the spatial information, MPS yields the harmonic spectrum corresponding to the center of a 1D FOV where $B_{\text{off}} = 0$ mT. Since the gradient field only produces local offsets to scan different ranges of the respective dynamic magnetization curve, relatively high MPS spectra also yield relatively high MPI signals. This can be easily proven via (2.41) and (2.42), which state that the MPI signal in time domain can be written as the convolution of the tracer distribution in the FOV and the PSF. Written in frequency domain, (2.42) yields:

$$\mathcal{F}\left(\mathrm{IMG}(x_s(t))\right) = \mathcal{F}\left(c_{\mathrm{Fe}}(x)\right) \cdot \mathcal{F}\left(\dot{\mathcal{L}}\left(\frac{\mu_0 m}{k_B T} H_{\text{Drive}}(t)\right)\right) \tag{2.45}$$

where $\mathcal{F}\left(\mathrm{IMG}(x_s(t))\right)$ is the MPI signal divided by a constant factor and the velocity of the FFP, $\mathcal{F}\left(c_{\mathrm{Fe}}(x)\right)$ is the tracer distribution, and $\mathcal{F}\left(\dot{\mathcal{L}}\left(\cdot\right)\right)$ is the MPS spectrum, all in frequency domain. The MPI signal outside of the center of the FOV therefore directly depends on the MPS spectrum.

The lack of a gradient field, and therefore lack of a FOV, gives MPS the significant advantage in the characterization of MNP that it is considerably easier and less expensive to build than an MPI system. Additionally, it has a much higher sensitivity since the pickup coils are closer to the sample.

Typically, MPS measurements are performed at a drive field frequency of $f = 25$ kHz at field strengths between $B_{\text{Drive}} = 5$ mT and $B_{\text{Drive}} = 25$ mT as MPI is typically operated in this regime [8] [28]. Yet, since safety limits in MPI are still debated [113] [116], MPS has also been established as a valid tool to investigate the dynamic behavior of MNP at other frequencies [138] [75].

As the maximum dose of MNP that may be injected into the body is limited [142], it is not possible to just increase the particle concentration to maximize the signal indefinite. The aim is therefore to produce particles with large amplitudes of the MPS spectrum normalized to the iron content of the particles. The typical procedure of particle characterization in MPS is the comparison of the examined tracer with the established tracer Resovist, normalized to the iron content in $\text{Am}^2/\text{mol(Fe)}$ or $\text{Am}^2/\text{mg(Fe)}$. The tracer Resovist, as a clinically approved contrast agent, has been used for several studies since the beginning of the research on MPI [39] [142] and has been established as a gold standard for tracer characterization in MPI [1] [33] [92]. A tracer with an iron normalized harmonic spectrum larger than Resovist is considered a potentially suitable tracer. For an intuitive comparison of several spectra, often only the amplitude of the third harmonic is used [92] [127], enabling the comparison of tracers via a single parameter. The drawback of this comparison is the omission of the harmonic decay.

2.3.3. Magnetic Property Measurement System

The SQUID based MPMS is a well-established technique for the characterization of magnetic materials [29] [144] [136] under the exposure of a static magnetic field. This technique dates back to 1967 [19], shortly after the development of the Josephson junctions that are employed for the measurements.

2.3.3.1. Measurement principle The MPMS enables quasi-static measurements of MNP (or any other magnetic material) in a wide variety of temperatures and magnetic fields. The parameter space comprises a variable temperature between 2

K and 400 K at field strengths up to 7 T [9], enabling both $m(H)$ and $m(T)$ measurements that can be converted to $M(H)$ and $M(T)$ measurements by normalizing m to the volume of the material.

Contrary to the signal generation in MPI in section 2.3.1 or MPS in section 2.3.2, the static magnetic field of $M(H)$ measurements allows the particles to reach static equilibrium. Given a certain waiting time between applying the magnetic field and measuring the particle magnetization, MPMS measurements enable the acquisition of the steady state magnetization.

2.3.3.2. Tracer characterization In consequence to the static character of the method, dynamic influences can be ignored (at least for MNP in liquid suspensions) and the measured magnetization of MNP can be modeled as a superposition of magnetization curves given by the saturation magnetization M_{sat} and the Langevin function (2.3) and (2.4):

$$M(H) = M_{\mathrm{sat}} \int P(d_{\mathrm{c}}) \mathcal{L}(H, d_{\mathrm{c}}) \mathrm{d}d_{\mathrm{c}} \tag{2.46}$$

where $P(d_{\mathrm{c}})$ is the size distribution of magnetic core diameters. There are currently two established fit procedures to reconstruct $P(d_{\mathrm{c}})$ from magnetization measurements, both employing the Moment Superposition Model by Chantrell [16]: A fit with a fixed curve form, described by the mean (or median) core diameter μ and standard deviation σ on the one hand and a completely free reconstruction in a certain range of diameters on the other hand.
For the fixed curve fit, a log-normal distribution is usually presumed (among others in [28] and [92]), given by (2.6) and (2.7), which, for example, can be solved by employing the Levenberg-Marquardt algorithm [93]. Assuming that the saturation magnetization is reached, the inverse problem consists of five unknown variables for a bimodal distribution (μ_1,σ_1,μ_2,σ_2,β) and two variables for a monomodal distribution (μ_1,σ_1).

The free reconstruction describes the size distribution as a classic inverse problem with the measured magnetization M, a system function $\mathbf{A}$ and the unknown solution $P(d_{\mathrm{c}})$:

$$M(H) = \mathbf{A}(H, d_{\mathrm{c}}) P(d_{\mathrm{c}}) \tag{2.47}$$

The system function $\mathbf{A}$ is a matrix with i rows and j columns, where i is the number of data points of the magnetization measurements and j is the number of core sizes. This inverse problem can be treated, for example, with the SVD approach, as first done by Berkov [6]. In comparison, both approaches have advantages and disadvantages. The advantage of predefined distribution functions is the reduction of the solution space to the variables of the function. The disadvantage of this approach is the fixed curve form that might lead to inaccurate results, if the *a priori* assumptions are incorrect. For free reconstructions, the advantages and disadvantages are interchanged. They may have a large solution space and, in case of magnetization measurements, are ill-conditioned, giving rise to the need of heavy regularization of the singular values. On the other hand, it is possible to reconstruct the size distribution without *a priori* assumptions on the particles.

After having laid the foundations necessary for this thesis, the MNP used for all experiments will be presented and characterized via MPS and MPMS. Moreover, a reconstruction procedure will be presented to obtain the size distribution of particle cores without *a priori* assumptions or singular value regularization.

3. Magnetic characterization of tracers used in the thesis

For several years, the tracer Resovist® was a gold standard for MPI. At the time of the introduction of MPI by Gleich and Weizenecker [39], it was a commercially available and clinically approved contrast agent for Magnetic Resonance Imaging and also showed promising results in MPI. Since then, Resovist has been taken off the market in Europe, making it difficult to acquire Resovist® for experiments. An alternative is the tracer FeraSpin R by the Berlin based company nanoPET Pharma GmbH. This tracer has been shown to have nearly the same magnetic properties as Resovist® [37]. Additionally, differently sized fractions of FeraSpin R, named FeraSpin XS, S, M, L, XL and XXL, are available. These separated fractions of FeraSpin R have the same chemical composition as Resovist® and differ in their mean hydrodynamic diameter ranging between 20 nm and 70 nm [92]. Due to the commercial availability, the same chemical composition and the broad range of particle sizes, FeraSpin R and its 6 fractions have been chosen for all experiments in this thesis.

In the following chapters, the tracers will be characterized regarding their magnetic properties. Here, a characterization of their magnetic core sizes will be performed based on static magnetization measurements. Furthermore, the MPS will be used for the dynamic tracer characterization, yielding a first indication of the potential tracer performance in MPI.

3.1. Static magnetic characterization

The static $M(H)$ measurements were performed according to chapter 2.3.3, employing a commercial MPMS system from Quantum Design (USA). All measurements were performed at room temperature with applied fields between 0 T and 5 T. All samples were diluted to an iron concentration of $c_{\mathrm{Fe}} = 5$ mmol/L. To obtain the magnetic core size distribution, a fit procedure based on the iterative Kaczmarz algorithm, that will briefly be described here, was used.

3.1.1. Measurements

The results of the static $M(H)$ measurements can be seen in Fig. 24 and 25. Here, the results for the entire magnetization curve up to 5 T, as well as a limited magnetization curve up to ±25 mT, are depicted. The $M(H)$ measurement up to 5 T is the basis for the fit of the magnetic core size distribution, whereas the limited $M(H)$ measurements yields the static behavior in the field regime typical for MPI.

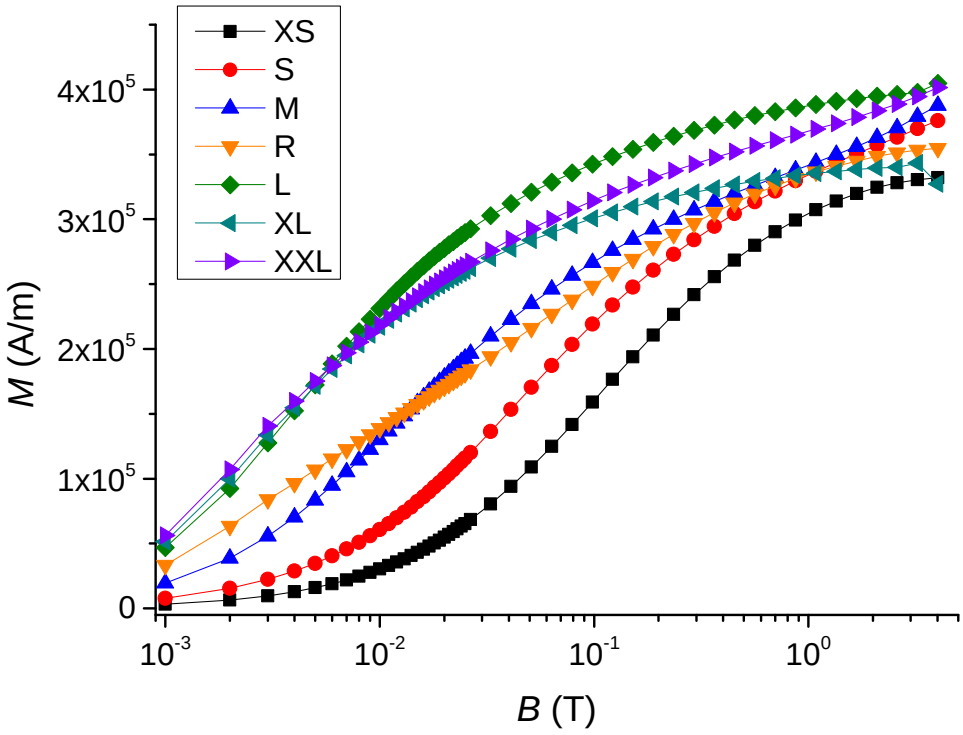

Figure 24: Magnetization curves of FeraSpin series.

It can be seen in Fig. 24 as well as in Fig. 25 how the differently sized particles have very different magnetization behaviors. While small particles, like FeraSpin XS and S, exhibit a very slow increase in magnetization that grows stronger for larger field strengths, the magnetization of large fractions, like FeraSpin L, XL and XXL, already exhibit a strong increase in magnetization at low field strengths. Some particles even show intersecting magnetization curves, like FeraSpin M and R. It has been demonstrated by Eberbeck et al. that this phenomenon may be attributed to the different mode sizes in a bimodal distribution of magnetic core sizes [28].

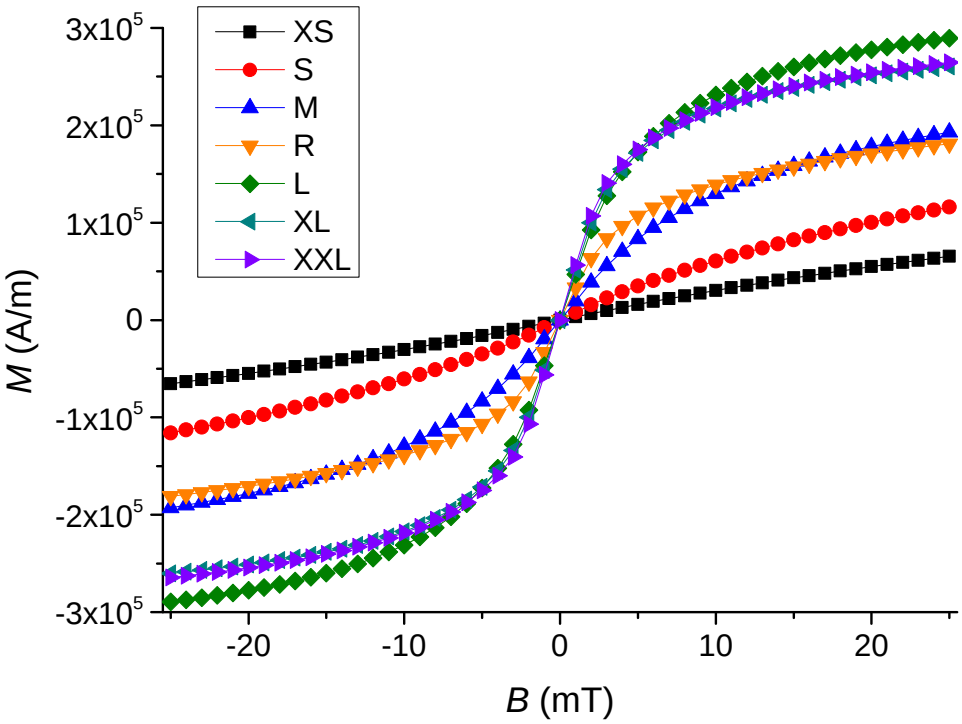

Figure 25: Limited magnetization curve in the boundaries $[-25\text{mT}, +25\text{mT}]$.

3.1.2. Fit procedure

In chapter 2.3.3, the current methods for a fit of the magnetic core size distribution were presented.

In general, the size distribution is reconstructed by solving the inverse problem in (2.47) for $P(d_c)$ with $\mathbf{A}$ as the system function of the magnetization measurement. Here, a free reconstruction will be presented that is based on the iterative Kaczmarz algorithm, which is also employed for MPI. This fitting procedure combines advantages of free estimations and fits based on a fixed curve form. It neither relies on predefined curve forms nor on singular value based regularization. Instead, the iteration number plays the role of the regularization parameter [53].

Corresponding to the system function in MPI, $\mathbf{A}$ describes the response of every particle core size to the applied magnetic field strength H_i (see Fig. 26).

The particle distribution in the FOV in (2.37), the size distribution is reconstructed via:

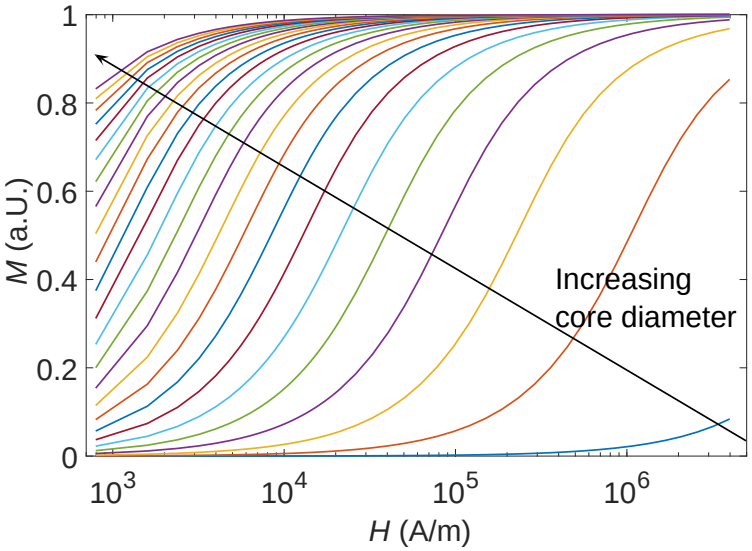

Figure 26: System function of the magnetic core size distribution fit employing magnetization measurements.

$$P_n = P_{n-1} + \frac{M_i - A_i^{\mathrm{T}} P_{n-1}}{||A_i||_2^2} A_i, i = 1...m \tag{3.1}$$

with m as the number of measured data points. Every iteration n therefore consists of a sweep through all measurement values, resulting in m subiterations. In each subiteration, the size distribution is reconstructed with the row of the system function A_i and the measurement point M_i. In accordance to results based on experiments and simulations [118], the reconstruction of $P(d_c)$ will be performed with $n = 1000$ iterations.

3.1.3. Fit results

The obtained size distributions are depicted in Fig. 27. FeraSpin R as the basis suspension has a large mode at core diameters around 7 nm and a small mode at core diameters around 25 nm. FeraSpin XS and S are the only suspensions with only one mode of particle diameters, both in the regime of the small particle mode of FeraSpin R. While FeraSpin S still consists of particle sizes up to 17 nm, FeraSpin XS solely consists of very small particles up to 12 nm. In the size distribution of FeraSpin M, two modes are evident, even though they are already very close to each

other and can nearly be treated as one very broad mode around 10 to 15 nm. The fractions FeraSpin L to XXL consist mainly of the larger mode of around 25 nm and only have very few small particles contributing to the magnetization curve.

FeraSpin R and its three large fractions all exhibit particle sizes of up to 34 nm. This result is in contradiction to earlier size fits where a slow decay of particles sizes up to 50 nm was found [92]. Still, those large particle sizes could not be observed via transmission emission microscopy, so this might be a more realistic representation.

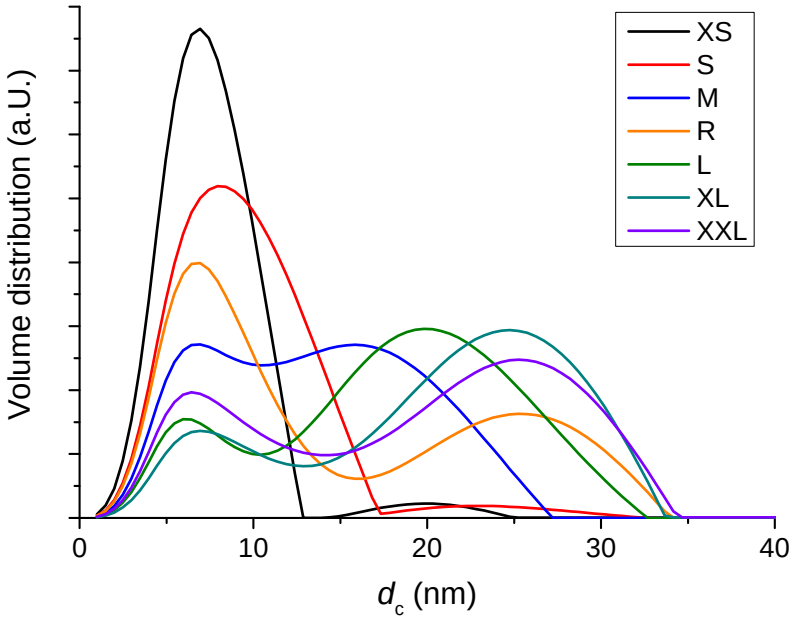

Figure 27: Magnetic core size distribution of FeraSpin Series.

In the following section, the results of the dynamic magnetic characterization are presented.

3.2. Dynamic magnetic characterization

The MPS characterization of the FeraSpin Series was performed with an iron concentration $c_{\mathrm{Fe}} = 50$ mmol/L, frequency $f = 25.25$ kHz, measurement time $t = 10$ s, and the drive fields $B_{\mathrm{Drive}} = [12, 25]$ mT.

The resulting spectra for both field strengths are in accordance to the static magnetization curves at $M(25mT)$ and their corresponding magnetic size distributions, as it is assumed that particles of $d_c > 20$ nm produce the strongest MPS signal [39] [33].

While the smallest fraction FeraSpin XS and S exhibit only a very weak spectrum that at some point drop below noise level, the harmonic amplitudes are much larger for bigger particles. While FeraSpin M already exhibits a similar spectrum like FeraSpin R at lower harmonics (especially for $B_{\mathrm{Drive}} = 25$ mT), its harmonic amplitudes drop much faster than for unfractioned FeraSpin R. For the weaker drive field $B_{\mathrm{Drive}} = 12$ mT, it nearly drops to the level of FeraSpin S of around the 31st harmonic. A similar behavior can be observed for FeraSpin L which drops to the level of FeraSpin R for $B_{\mathrm{Drive}} = 12$ mT at higher harmonics and nearly reaches the level of FeraSpin XL and XXL at $B_{\mathrm{Drive}} = 25$ mT at low harmonics. FeraSpin XL and XXL perform very similar at all applied drive fields.

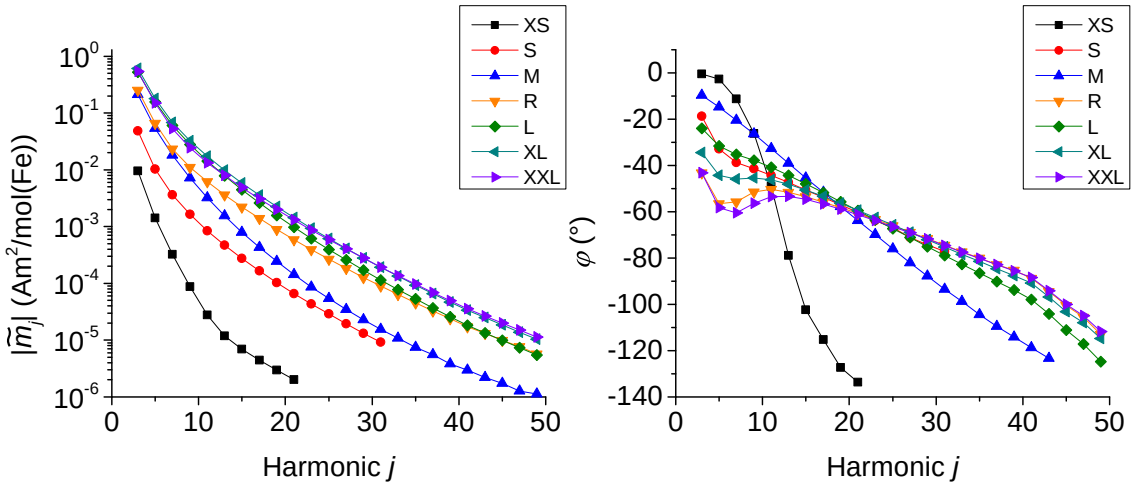

Figure 28: MPS characterization at $B_{\mathrm{drive}} = 12$ mT.

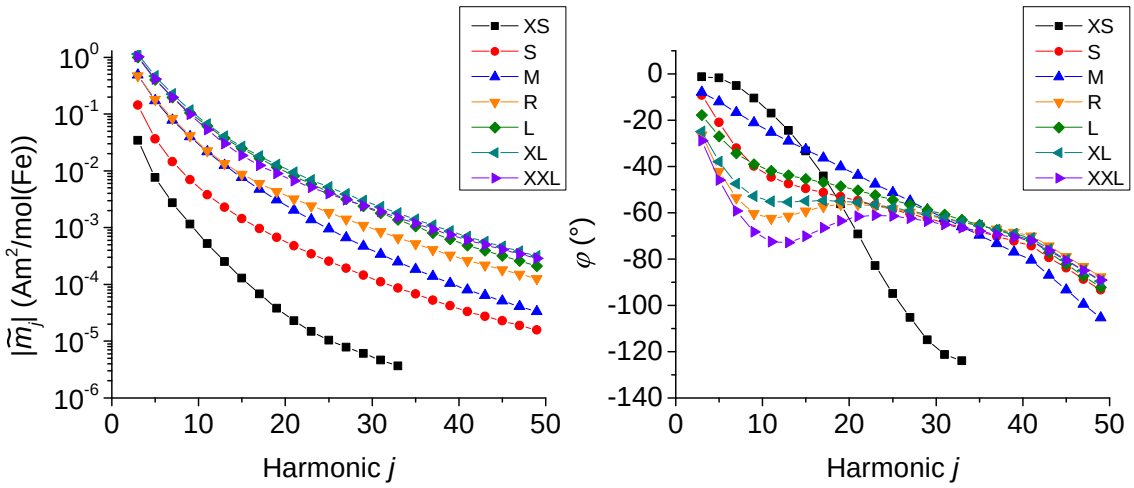

Figure 29: MPS characterization at $B_{\mathrm{drive}} = 25$ mT.

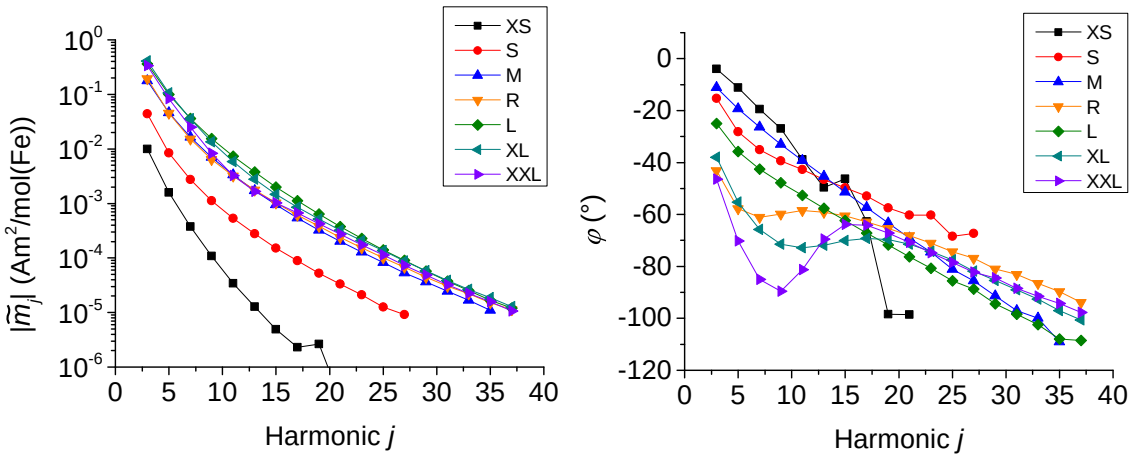

Figure 30: MPS characterization at $B_{\text{drive}} = 12$ mT of immobilized particles.

Furthermore, all particles were immobilized via freeze-drying to evaluate the ratio of Néel rotation and combined rotation via Néel and Brown for each suspension. The results are depicted in Fig. 30 and Table 1. In the latter, the ratio of the third harmonic amplitudes $|\tilde{m}_3|$ as well as the $|\tilde{m}_5|/|\tilde{m}_3|$ ratios for mobile and immobile particles are depicted. In accordance to section 2.1.5, the attenuation of harmonic amplitudes grows stronger with increasing particle sizes. The value of 1.03 for FeraSpin M can likely be attributed to agglomerations in the freeze-drying process or deviations from the measurement.

Tracer	$\frac{\lvert\tilde{m}_{3,\mathrm{N}}\rvert}{\lvert\tilde{m}_{3,\mathrm{NB}}\rvert}$	$\frac{\lvert\tilde{m}_{5,\mathrm{N}}\rvert\lvert\tilde{m}_{3,\mathrm{NB}}\rvert}{\lvert\tilde{m}_{3,\mathrm{N}}\rvert\lvert\tilde{m}_{5,\mathrm{NB}}\rvert}$
FeraSpin XS	1.00	1.00
FeraSpin S	0.92	0.90
FeraSpin M	0.94	1.03
FeraSpin R	0.77	0.90
FeraSpin L	0.70	0.91
FeraSpin XL	0.67	0.88
FeraSpin XXL	0.62	0.88

Table 1: Ratio of $|\tilde{m}_3|$ and $|\tilde{m}_5|/|\tilde{m}_3|$ of pure Néel rotation and combined rotation via Néel and Brown.

Based on these measurements, it can be assumed that FeraSpin L to XXL with comparably large core sizes will exhibit the most promising MPI performance, even though it can be observed that the harmonic amplitudes strongly decrease when Brownian rotation is supressed.

What these measurements cannot reveal is their quantitative performance. Therefore, two essential questions about the tracer performance arise that cannot be answered by MPS measurements alone:

- What is the achievable resolution under different noise conditions?
- What does an increase of the harmonic amplitudes quantitatively mean for the resolution improvement?

Before answering these questions, how the harmonics in general are related to the achievable spatial resolution in MPI will first be investigated.

4. Influence of the available harmonics on the achievable resolution

In this chapter, the concepts of PSF and MTF to evaluate the imaging performance as they were introduced in a general sense in section 2.2 are set in the context of MPI. Furthermore, a relation will be presented to calculate the achievable resolution in dependence on the SNR.

4.1. Spatial frequencies in MPI

It has been pointed out in chapter 2.2.2, that the MTF is the Fourier Transform of the PSF. Here, the PSF corresponds to the convolution kernel of X-Space MPI (2.42) and the MTF corresponds to the MPS spectrum. Their relation is depicted in Fig. 31, where both are given for $l_{\text{fov}} = 2$ cm.

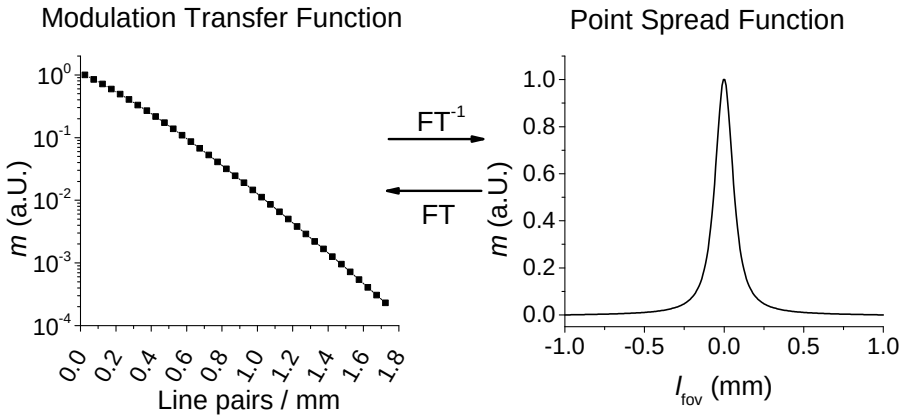

Figure 31: The MTF in MPI corresponds to the MPS spectrum. It is related to the PSF via a Fourier Transform (FT) and vice versa.

In consequence, MPS spectra may be plotted not only over the harmonic number but also over the cycles/mm of the spatial frequencies. As there is no FOV in MPS due to the missing field gradient, a hypothetical field gradient has to be presumed. Then, a theoretical FOV can be calculated via the relation:

$$l_{\text{fov}} = \frac{\mu_0 H_{\text{Drive}}^{\text{pp}}}{G} \tag{4.1}$$

where $H^{\mathrm{pp}}_{\mathrm{Drive}}$ is the peak to peak amplitude of the drive field. Given the theoretical FOV, the spatial frequency f_{spatial} in cycles per mm of the j-th harmonic can be easily derived via the relation:

$$f_{\mathrm{spatial},j} = \frac{j}{2l_{\mathrm{fov}}} = \frac{jG}{2\mu_0 H^{\mathrm{pp}}_{\mathrm{Drive}}}. \tag{4.2}$$

This can be proven in spatial- as well as in frequency domain. It can be seen in Fig. 32, that one period of the drive field with frequency f corresponds to one forward and backward scan of the FOV, hence $2l_{\mathrm{fov}}$. Since the harmonics of the PSF (the MPS spectrum) are multiples of the fundamental frequency $j \cdot f$, the j-th harmonic also has j periods over the course of two scans of the FOV. This principle is depicted with a PSF and its corresponding first, third and fifth harmonic.

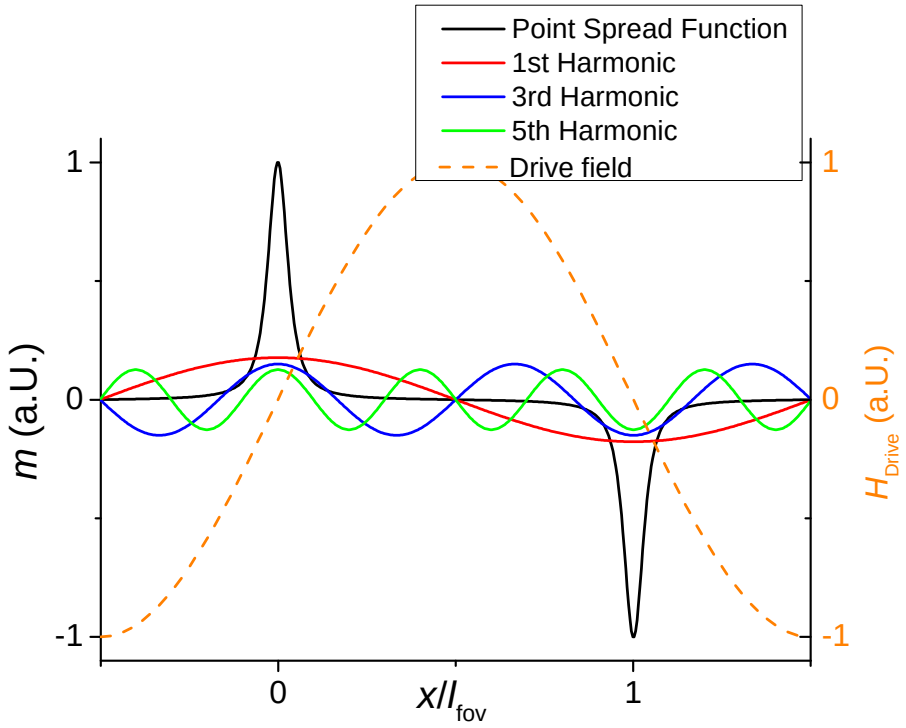

Figure 32: Spatial frequencies in time domain. The harmonic number j corresponds to the number of periods to scan the FOV twice.

Corresponding to the first harmonic, that has one period over the course of a forward and backwards scan, higher harmonics (here: the third and fifth harmonic) have three and five periods in two scans of the FOV, confirming the statement in equation (4.2).

In frequency domain, where the system function is employed for reconstruction (see section 2.3.1.3), the spatial frequencies can be derived from a measured as well as from a modeled system function. A modeled system function, split into odd and even harmonics and mapped over the normalized FOV, is depicted in Fig. 33.

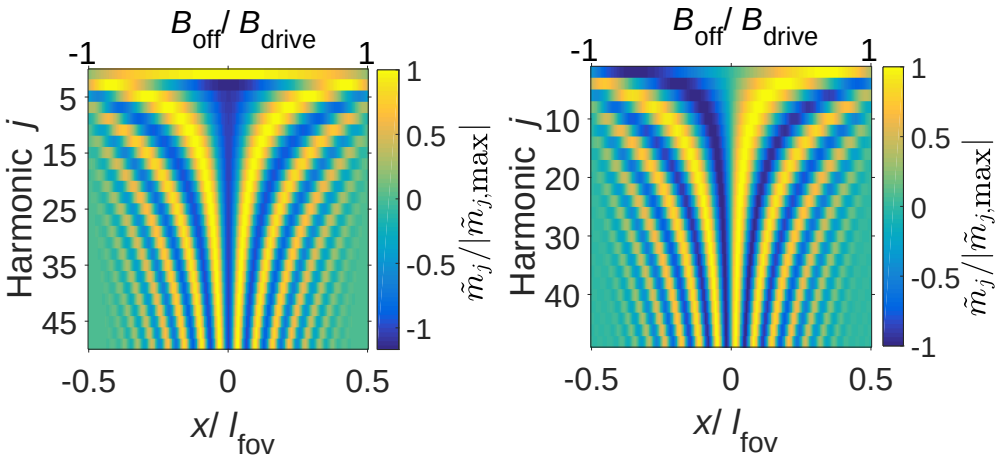

Figure 33: The row wise normalized amplitudes of odd (left) and even harmonics (right) in a Langevin modeled system function, mapped over the FOV. The spatial frequencies correspond to half of the harmonic number.

Here, the row wise normalized harmonic amplitudes up to the 49th harmonic are depicted over a normalized FOV and the corresponding offset fields $B_{\text{off}}/B_{\text{Drive}} = [-1, ..., 1]$. It can be seen, that due to the characteristic field offset over the FOV, a different harmonic spectrum is generated at each location. The maxima and minima of the harmonic amplitudes of each harmonic over the FOV are clearly visible as the yellow and blue areas. Moreover, it can be seen that the density of the maxima and minima over the FOV increases with every harmonic. The spatial frequencies can be derived in the same manner as they were from the PSF. The amplitudes of the first harmonic in Fig. 33 (left) span a half wave over one FOV, while the amplitudes of the third harmonic span 1.5 waves over the same distance. The same applies for the even harmonics in Fig. 33 (right), where the amplitudes of the second harmonic span exactly one period over the FOV. Therefore, the harmonic number can be directly attributed to the spatial frequencies according to (4.2) in the same manner as it was in spatial domain.

4.2. Intrinsic and extrinsic resolution

Having established the relation between spatial frequencies and the harmonic number in (4.2) as well as the relation between MPS spectrum and MTF, one can plot the MTF and set a factor marking the spatial frequency corresponding to the maximum loss in contrast, where two objects can barely be resolved as it was presented in section 2.2.2. This procedure is an absolutely valid approach and once having found a reliable threshold, it will be a trustworthy measure for the highest resolution achievable by the tracer. However, it is important to keep in mind that the safe maximum dose for the tracer Resovist was reported to be 2.2 mg Fe/kg [121]. Given the blood volume of about 77 mL/kg for men and about 65 ml/kg for women [120], one can calculate the maximum iron concentration in blood in the steady state for men to $c_{\mathrm{Fe,\,max}} = \frac{2.2\,\mathrm{mg/kg}}{77\,\mathrm{mL/kg}} = 0.029\,\mathrm{mg/mL} = 0.5\,\mathrm{mmol/L}$ and for women to $c_{\mathrm{Fe,\,max}} = 0.034\,\mathrm{mg/mL} = 0.6\,\mathrm{mmol/L}$, respectively. For an application in humans, it will therefore not be possible to increase the dose indefinite to improve the SNR, so one will need to include the noise level into considerations regarding the resolution.

The principle is visualized in Fig. 34. The MTF is the normalized MPS spectrum (in [70] the, MPS sprectrum is normalized to the maximum of the PSF) and due to this normalization, its shape and amplitude are independent from the iron concentration (assuming no particle interaction at higher concentrations). This does not apply for the noise level in the MTF. Depending on the iron content, the noise floor might reach completely different levels in the otherwise unchanged MTF. For low iron concentrations like the safe medical dose in the steady state, it is possible that a significant part of the harmonics (and therefore spatial frequencies) drops below the noise floor, including the resolution threshold, which makes these harmonics unusable for reconstruction. The SNR is therefore directly related to the achievable resolution, which makes the resolution a dynamic parameter depending on the particle properties and the iron amount per voxel in the FOV. Hence, two resolution definitions are presented here:

- Intrinsic resolution: Maximum achievable resolution depending on the shape of the MTF or PSF.
- Extrinsic resolution: Achievable Resolution under given noise conditions and iron concentration in dependence on the SNR.

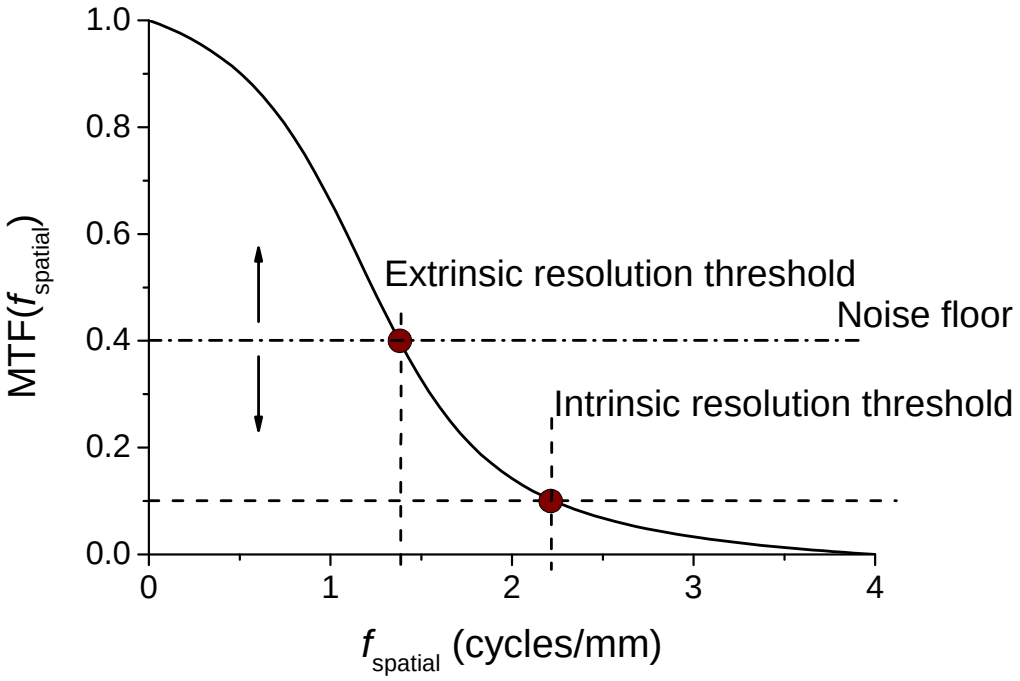

Figure 34: The Modular Transfer Function as a measure for the maximum resolution. The intrinsic resolution, derived from a defined contrast loss in the MTF, might differ significantly from the extrinsic resolution determined by the SNR.

To resolve two objects at a certain distance from each other in the reconstructed image, at least the corresponding spatial frequency (i.e. harmonic) is needed. A visualization of the influence of the available harmonic on the resolution is depicted in Fig. 35. Here, a simple tracer distribution consisting of two square objects next to each other is shown in comparison to the spatial frequencies of the 3rd and 9th harmonics. To image both objects, so that they can be distinguished from each other in the reconstructed image, the highest spatial frequency has to be close-meshed enough to resolve the objects. This principle is comparable to a spatial version of the Nyquist-Frequency (see section 2.2.3) with the extrema density of the highest available spatial frequency as the sample rate. Whether a harmonic is available for reconstruction mainly depends on the SNR, which is determined by the magnetic properties of the tracer, the tracer amount and the level of background noise. It is therefore not enough to consult the MTF for an estimation of the resolution, it is important to know the MPI signal and the harmonics above noise that can be employed for reconstruction. Using (4.2) with $f_{\text{spatial},j}(j_{\max})$ with $j_{\max}$ as the highest harmonic employed in reconstruction one can calculate its inverse R to obtain the

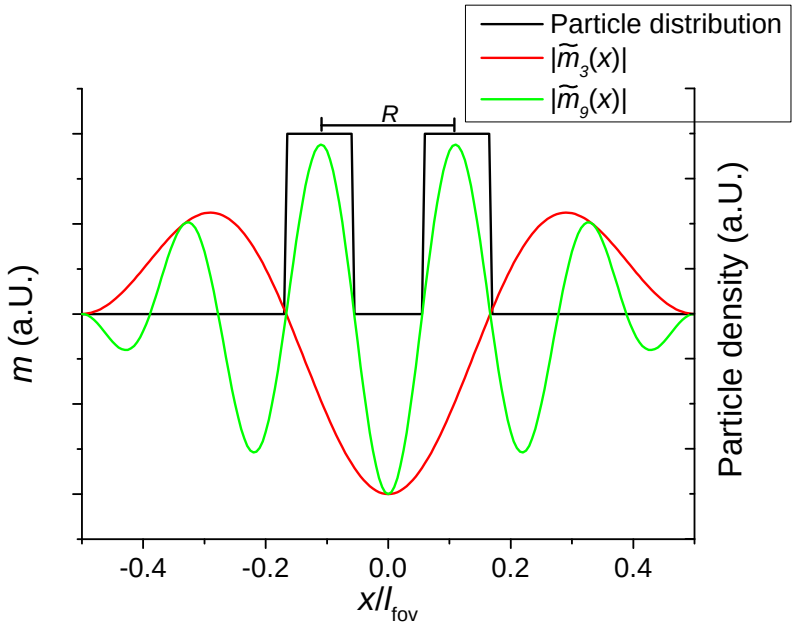

Figure 35: Spatial frequencies of the 3rd and 9th harmonic with a simple theoretical tracer distribution. The spatial frequency of the 3rd harmonic is too coarse-meshed to image the given tracer distribution. The spatial frequency of the 9th is close-meshed enough to distinguish between the two tracer clusters after reconstruction.

closest distance between two object centers that can still be resolved:

$$R = \frac{1}{f_{\text{spatial,max}}} = \frac{2l_{\text{fov}}}{j_{\max}} = \frac{2\mu_0 H^{\text{pp}}_{\text{Drive}}}{j_{\max} G}. \tag{4.3}$$

In the example above, the SNR must therefore be sufficiently high, so that the 9th harmonic can be employed for reconstruction. For the normalized FOV, the resolution is then calculated to $R = 2l_{\text{fov}}/9 = 0.22l_{\text{fov}}$, which is just the distance between the two object centers in Fig. 35.

4.3. Influence of the harmonic structure in spatial domain

So far, it has been presumed, that the extrema of the spatial frequencies in frequency domain, which determine the achievable spatial resolution, are equally distributed over the FOV. This would be correct, if the spatial frequencies were based on a simple trigonometric function $\sin(jx)$. Yet it has been proven in [108], that the

harmonic amplitudes in MPI over a 1D FOV are based on Chebyshev polynomials of the second kind and the amplitudes of the j-th harmonic are based on the $\ll j-1\gg$-th Chebyshev polynomial. Furthermore, the harmonics are modulated with the velocity of the FFP, as was proven in [42]. This yields for the modulated j-th Chebyshev polynomial of the second kind:

$$\tilde{U}_j(x) = \underbrace{\frac{\sin((j+1)\cos^{-1}(x))}{\sin(\cos^{-1}(x))}}_{\text{Chebyshev polynomial } U_j(x)} \underbrace{\cos\left(\frac{\pi}{2}x\right)}_{\text{FFP modulation}} . \tag{4.4}$$

Exemplary modulated Chebyshev polynomials according to (4.4) are depicted in

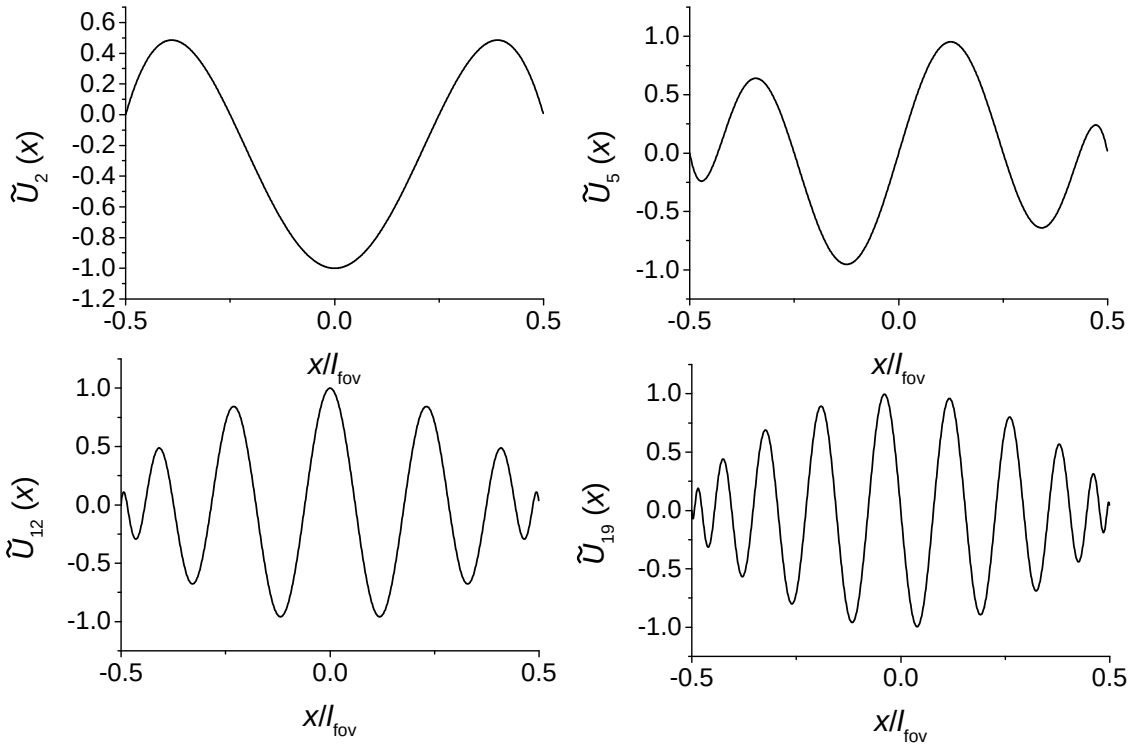

Figure 36: Modulated Chebyshev polynomials of the second kind. Clockwise from top left to bottom left: $\tilde{U}_2, \tilde{U}_5, \tilde{U}_{19}, \tilde{U}_{12}$, which corresponds to $j = 3, 6, 20, 13$.

Fig. 36. Here, an issue can be seen that so far has not been addressed. In the equation for the achievable spatial resolution in dependence on the highest available harmonic number, the density of extrema over the FOV was presumed to be equally distributed. Here, it can be seen that the distance between extrema $\Delta\epsilon = \epsilon_j - \epsilon_{j-1}$ actually varies over the FOV. This becomes even clearer in Fig. 37. Here, the distance of all extrema $\Delta\epsilon$ are depicted for the same Chebyshev polynomials as in

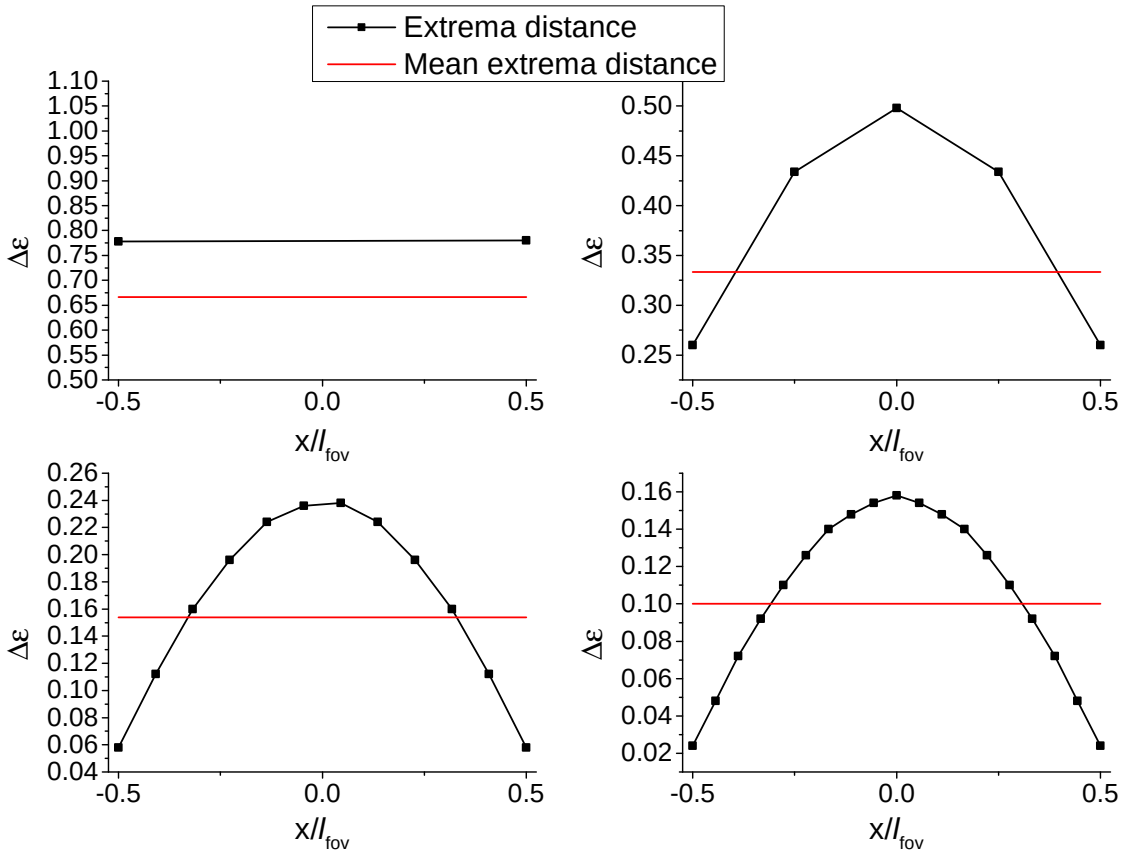

Figure 37: Extrema distance of Chebyshev polynomials in comparison to mean distance. Clockwise from top left to bottom left: $\tilde{U}_2, \tilde{U}_5, \tilde{U}_{19}, \tilde{U}_{12}$.

Fig. 36. So even though the mean value (i.e. the extrema density) is employed for the resolution, it should be kept in mind, that the extrema density is higher at the edges of the FOV. Yet at the same time, due to the modulation with the FFP velocity, the amplitude at the edges of the FOV is highly diminished. This reduces the number of measurable harmonics at the edges of the FOV in comparison to its center, compensating this effect. In order to have an easy-to-apply relation between maximum harmonic and achievable resolution, this effect will be neglected in following calculations.

After the influence of the harmonics on the achievable resolution was investigated in this chapter, the next chapter focuses on the question which parameters are best suited for MNP to yield the highest possible MPS spectrum.

5. Simulation of the optimum magnetic core size for MPI

The aim of the simulation is the description of the dynamic magnetic moment of magnetite MNP (Fe_3O_4) in a fast simulation environment, enabling the investigation of the influences of external parameters like the drive field B_{Drive}, frequency f, viscosity η and temperature T as well as the internal parameters magnetic core size distribution $P(d_{\mathrm{c}})$, saturation magnetization M_{sat}, effective anisotropy constant K and hydrodynamic shell thickness d_{h}.

5.1. Simulation method

The dynamic reaction of the total magnetic moment to an external magnetic field $H(t)$ of an ensemble of MNP can be described via a first order linear differential equation, based on the works of Shliomis [123] and Martsenyuk [94]. The differential equation denotes:

$$\vec{m}(t) = \chi V \vec{H}(t) - \tau \frac{\mathrm{d}\vec{m}(t)}{\mathrm{d}t} \tag{5.1}$$

with the magnetic moment m, magnetic field strength H, susceptibility χ, sample volume V and measurement time t. According to later reports regarding the field dependency of the relaxation time (then called rotational dynamics, as explained in section 2.1.7), the equation has to be extended accordingly and therefore reads:

$$\vec{m}(t) = V\vec{M}(\vec{H}(t)) - \tau(\vec{H}(t))\frac{\mathrm{d}\vec{m}(t)}{\mathrm{d}t}. \tag{5.2}$$

The numerical discretization for just one cartesian direction of (5.2) yields:

$$m_i = m_{i-1} + (m_{i,\mathrm{eq}}(H_i) - m_{i-1})\left(1 - \exp\left(-\frac{\Delta t}{\tau(H_i)}\right)\right) \tag{5.3}$$

where m_{eq} is the equilibrium magnetic moment without dynamic influences, Δt is the time increment and $\tau(H)$ is the timescale of the rotational dynamics in dependence on H as described in [119]. The principle is also visualized in Fig. 38 for the first

three discrete steps and shows how the dynamic magnetic moment is treated as the static equilibrium moment delayed by a damping parameter given by the rotational dynamics. In the discretized approach, the steady state moment is updated every Δt s, causing the dynamic moment to exponentially approach the new value of m_{eq}, which is updated every Δt s. The damping parameter $\tau(H)$, that is also updated after every Δt s, determines how fast m_{eq} can be approached.

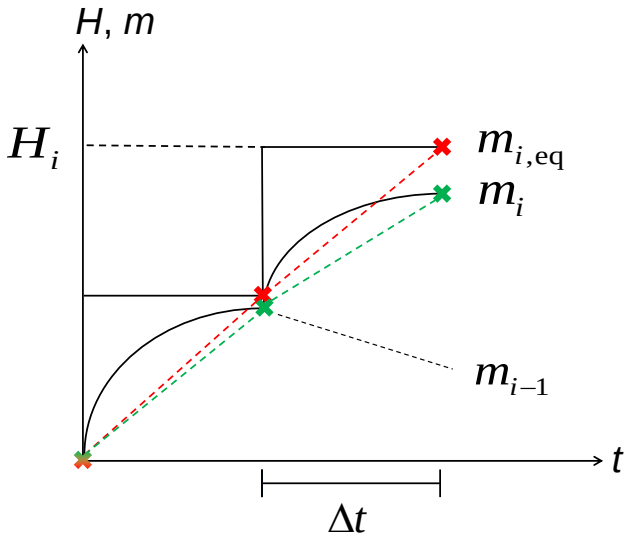

Figure 38: Visualization of the simulation principle. The dynamic magnetic moment (green) is expressed as the equilibrium moment (red), delayed by a time lag. The crosses represent the discrete values with the dashed lines being linear interpolations between them.

Using (5.3), the dynamic magnetic moment of a single particle can be calculated. For the calculation of the total magnetic moment of an ensemble of MNP with a volume weighted size distribution and a certain iron concentration and sample volume, the number of particles of each core size in the presumed range has to be calculated first. This becomes necessary as 1 mol iron of 5 nm particles corresponds to another total number of particles than 1 mol iron of 25 nm particles.

Given a certain sample volume V and an iron concentration c_{Fe}, one can easily calculate the amount of particles in mol iron via:

$$N_{\mathrm{mol}} = V c_{\mathrm{Fe}}. \tag{5.4}$$

Based on the iron densitiy $\rho = 7874 \cdot 10^3\,\mathrm{g/m^3}$ and the particle volume V_c, the mass of one particle is calculated via:

$$m_\mathrm{mass} = \rho V_\mathrm{c} \tag{5.5}$$

to obtain the number of particles per mol iron N_p employing the molar mass of iron $M_\mathrm{molar} = 55.85$ g/mol via:

$$N_\mathrm{p} = \frac{M_\mathrm{molar}}{m_\mathrm{mass}}. \tag{5.6}$$

With the number of particles per mol iron, the absolute number of particles in mol and the size distribution $P(d_\mathrm{c})$, the number of particles for each core diameter N_P can be obtained (see Fig. 39 for the normalized number of magnetite particles) via:

$$N_\mathrm{P} = 3N_\mathrm{p}N_\mathrm{mol}P(d_\mathrm{c}) = \frac{3M_\mathrm{molar}}{\rho}\frac{VcP(d_\mathrm{c})}{V_\mathrm{c}} \tag{5.7}$$

where three is the number of iron atoms in one magnetite molecule (Fe_3O_4).

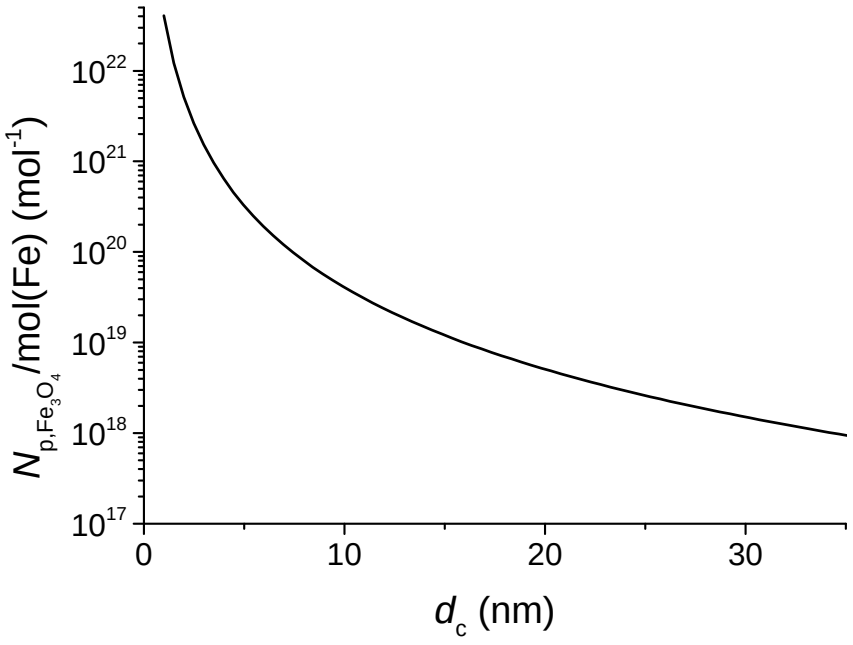

Figure 39: The number of magnetite particles per mol Fe.

The discretized differential equation therefore denotes as follows:

$$m_{\mathrm{i,total}} = \sum_{n=d_{\mathrm{c},1}}^{d_{\mathrm{c,max}}} N_{\mathrm{P},n}(P(d_{\mathrm{c}})) \left(m_{n,i-1} + (m_{n,i,\mathrm{eq}}(H_i) - m_{n,i-1}) \left(1 - \exp\left(-\frac{\Delta t}{\tau_n(H_i)} \right) \right) \right) \tag{5.8}$$

In the next sections, first the particle behavior in equilibrium state m_{eq} will be simulated, followed by the dynamic magnetic moment.

The following simulations will all be performed using the following parameters:

- $c = 5$ mmol/L
- $V = 30\,\mu\mathrm{L}$
- $B_{\mathrm{Drive}} = [5, 12, 25]$ mT
- $f = [25, 125]$ kHz
- $T = 300$ K
- $\tau_0 = 1 \cdot 10^{-10}$ s
- $M_{\mathrm{sat}} = 4 \cdot 10^5$ A/m
- $\Delta t = \frac{1}{400f}$

5.2. Calculation of the static moment

In this chapter, the magnetic moment will be calculated according to the Langevin function, that was introduced in section 2.1.3. This will not reflect a realistic dynamic behavior (at least in the core size regime important for MPI), but it will yield the static magnetic moment m_{eq} that is needed for the simulation of m_{dyn} via (5.8). The static magnetic moment is simulated for core sizes $d_{\mathrm{c}} = 1...35$ nm and the mentioned core parameters via:

$$m_{\mathrm{eq}}(d_{\mathrm{c}}, B_{\mathrm{Drive}}) = mN_P(d_{\mathrm{c}}) \left(\coth(\xi) - \frac{1}{\xi} \right) \tag{5.9}$$

and:

$$\xi = \frac{mB_{\mathrm{Drive}}}{k_B T} = \frac{M_{\mathrm{sat}}\pi/6 d_{\mathrm{c}}^3 B_{\mathrm{Drive}}}{k_B T}. \tag{5.10}$$

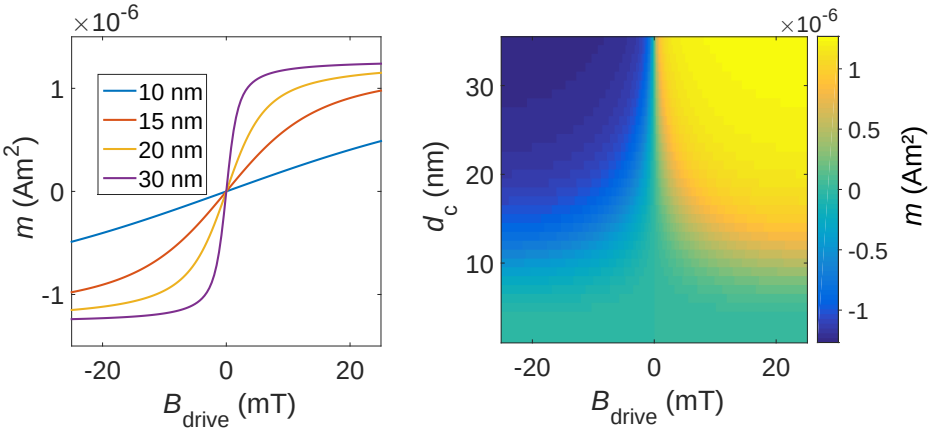

Figure 40: Static magnetic moment of an ensemble of monodisperse particles with $V = 30\,\mu\mathrm{L}$ and $c_{\mathrm{Fe}} = 5$ mmol/L. Left: The static magnetic moment for four different core diameters; Right: Surface plot of the static magnetic moment for all core diameters between 1 and 35 nm.

Ignoring all dynamic effects, the steepness of the magnetization curve increases with the core size of the MNP. While small particles of up to $d_{\mathrm{c}} = 10$ nm still behave nearly linearly up to $B_{\mathrm{Drive}} = 25$ mT, the magnetic moment increases rapidly for larger particles until it is nearly in saturation at $B_{\mathrm{Drive}} = 25$ mT for $d_{\mathrm{c}} = 30$ nm (Fig. 40). As it has already been clarified, this is not the behavior of MNP at quickly changing magnetic fields, where the rotation time due to Néel and Brownian movement have to be taken into account. This will be simulated in the following chapter via a magnetic moment lagging behind the steady state moment that was calculated here.

5.3. Simulation including rotational dynamics

In this simulation of the dynamic magnetic behavior of MNP under MPS conditions, single core particles (see section 2.1.8) are being modeled with the aim of finding a core diameter to maximize the amplitudes of the harmonic spectrum, which would increase the SNR and, hence, improve the MPI resolution. To that end, spherical monodisperse particles are modeled under the influence of different effective anisotropy constants K and shell thicknesses d_h. The zero field Néel relaxation time τ_N is varied via d_c and K. The zero field Brownian relaxation time is varied via d_c and d_h, whereby it depends on the hydrodynamic volume $V_\mathrm{H} = \pi/6(d_\mathrm{c} + 2d_\mathrm{h})^3$. Employing the zero field relaxation times, the rotational dynamics for Néel and Brownian rotation can be obtained in dependence on the Langevin argument ξ according to (2.17) and (2.19) (Fig. 41).

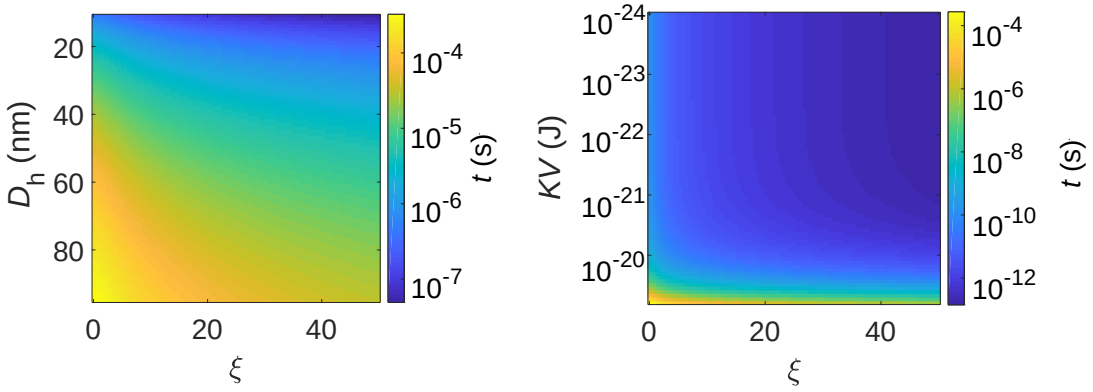

Figure 41: Field dependent rotational dynamics of Brownian (left) and Néel (right) rotation with $D_\mathrm{h} = d_\mathrm{c} + 2d_\mathrm{h}$.

Before simulating MNP to find the optimum core sizes for MPI, it will first be attempted to reproduce the MPS spectra of the FeraSpin series with Néel and Brownian rotation (see section 3.2 for MPS characterization of the tracers) to test the suitability of the simulation method. Hence, the obtained volume weighted size distribution from section 3.1 (Fig. 27) is converted to a number weighted size distribution via (5.7). By the right choice of K and d_h, the corresponding MPS spectra are fitted so that the deviation between simulation and measurement is minimized.

The result can be seen in Fig. 42 and Tab. 2 for all seven tracers from the FeraSpin series in absolute values, normalized to the iron content. It can be seen, that for all seven tracers, it was possible to find a $[K, d_\mathrm{h}]$ combination that fits well with at least the first odd harmonics, often even with higher harmonics that contribute little to the overall signal and are therefore especially difficult to reproduce. A limiting factor is the missing possibility to simulate distributions of the effective anisotropy constants and the hydrodynamic shell thickness as well as the option to simulate particles not only as single core but also as multi core particles which might be necessary for the FeraSpin series [92].

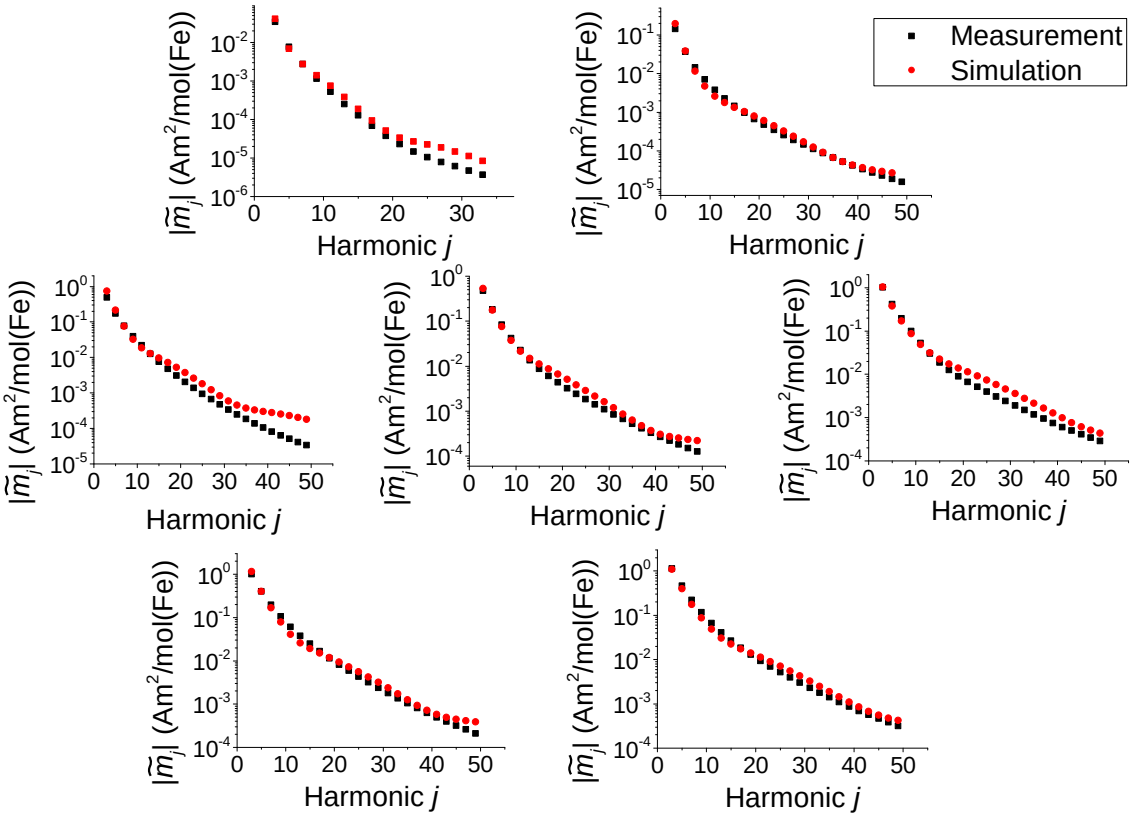

Figure 42: Comparison of measured and simulated MPS spectra of the FeraSpin series. Top row: FeraSpin XS and S; Middle row: FeraSpin M, R and L; Bottom row: FeraSpin XL and XXL.

After having confirmed the ability to reproduce actual MPS spectra, the parameter space for the simulation study will be defined next. In the early stage of the development of MPI, the optimum particle size was estimated in the regime of 30 nm [39]. Later on, it was suspected to be in the regime of about 25 nm, depending on the excitation frequency [34] [131] [31]. To cover this range of potentially suitable

particle sizes, core diameters up to 35 nm will be considered.

Tracer	K(J/m^3)	d_h (nm)
FeraSpin XS	15000	5
FeraSpin S	7000	15
FeraSpin M	8500	15
FeraSpin R	6500	20
FeraSpin L	6500	20
FeraSpin XL	5000	30
FeraSpin XXL	5500	30

Table 2: Fit parameters for FeraSpin series.

Regarding the effective anisotropy, a wide range is taken into account. Besides the effective anisotropy of bulk magnetite of about $K = 10000$ J/m^3 to $K = 13000$ J/m^3 [22] [46] [2], there have also been reports about the effective anisotropy of uniaxial MNP to be much larger with values of up to nearly 50000 J/m^3 [22] [46] [26]. Regarding MNP specially designed for MPI, there have been reports about effective anisotropies smaller than bulk [91]. Due to these many different reports of effective anisotropy constants the parameter space comprises $K = 3000...35000$ J/m^3.
For the hydrodynamic shell thickness there have been reports of thicknesses of about $d_h = 20$ nm for particles, that seem very suitable for MPI [91] [86] [131]. A report of Ferguson claims that the hydrodynamic diameter is typically 10 to 20 nm greater than the magnetic core size [31], so in this simulation the hydrodynamic shell thickness will be defined between 5 nm and 30 nm. There were also reports of even thinner shells of 2.5 nm [81]. However, these particles had core diameters of the same size, so shell thicknesses this small are not taken into account. Given these considerations, the parameter space for the simulation reads as follows:

- $d_\mathrm{c} = 1...35$ nm (index i)
- $K = 3000...35000$ J/m^3 (index j)
- $d_\mathrm{h} = 5...30$ nm (index p)

The principle of this parameter study is depicted in Fig. 43. For all [d_c,K] and [d_c,d_h] combinations, the matrices of Néel and Brownian zero field relaxation times

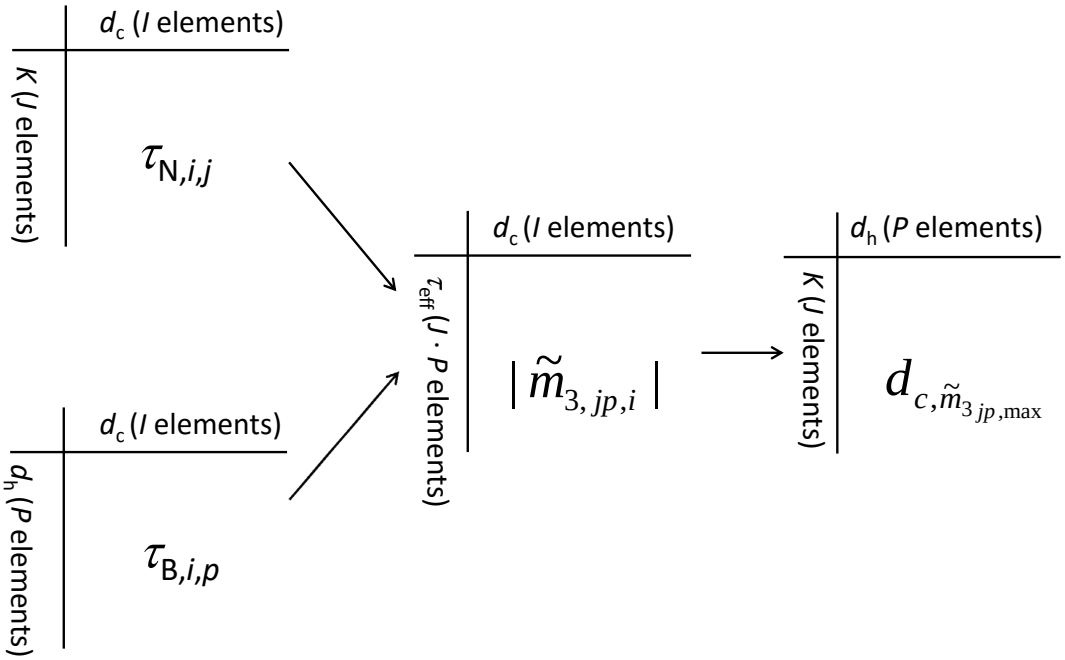

Figure 43: Principle of the parameter study for an optimized core size: Each $[d_c,K]$ and $[d_c,d_h]$ combination yields a specific Néel or Brownian relaxation time (left). For every $[d_c,d_h,K]$ combination the dynamic magnetic moment can be calculated, yielding a certain $|\tilde{m}_3|$ for every combination (middle). Picking the highest $|\tilde{m}_3|$ for each row, one obtains the optimum core diameter for every $[d_h,K]$ combination (right).

are calculated, yielding a $J \times I$ and a $P \times I$ matrix of relaxation times. Then, the dynamic magnetic moment is simulated for all parameter combinations $(J \cdot P) \times I$, given by the $J \cdot P$ effective relaxation times and I core diameters (Fig. 43 middle). Afterwards, a Fourier transformation is performed to obtain the harmonic spectra. The third harmonic amplitude $|\tilde{m}_3|$ was chosen as an indicator for a high harmonic spectrum. Thus, the core diameter that maximizes the third harmonic for each $[d_h,K]$ combination is found (right).

The simulation was performed for $f = 25$ kHz and $f = 125$ kHz, as well as for $B_{\mathrm{Drive}} = 5$ mT, $B_{\mathrm{Drive}} = 12$ mT and $B_{\mathrm{Drive}} = 25$ mT. The results of the simulations

for $B_{\mathrm{Drive}} = 25$ mT are depicted in Fig. 44 and Fig. 45 (the other results can be found in Appendix A) in maps of the potential $[d_{\mathrm{h}},K]$ combinations in the boundaries given earlier with the color maps indicating the optimum core size in nm (left) and their respective $|\tilde{m}_3|$ in Am^2 (right). It can be seen, that the resulting core size maps are split in two parts: The major part of the maps is independent of d_{h} and is only influenced by the effective anisotropy constant K. The second part is the area with high effective anisotropies and thin shell thicknesses. This area is largest at low frequencies and low drive fields (see Appendix A) and consists solely of the largest particle cores that were simulated. Those two areas represent the Néel and Brownian rotation.

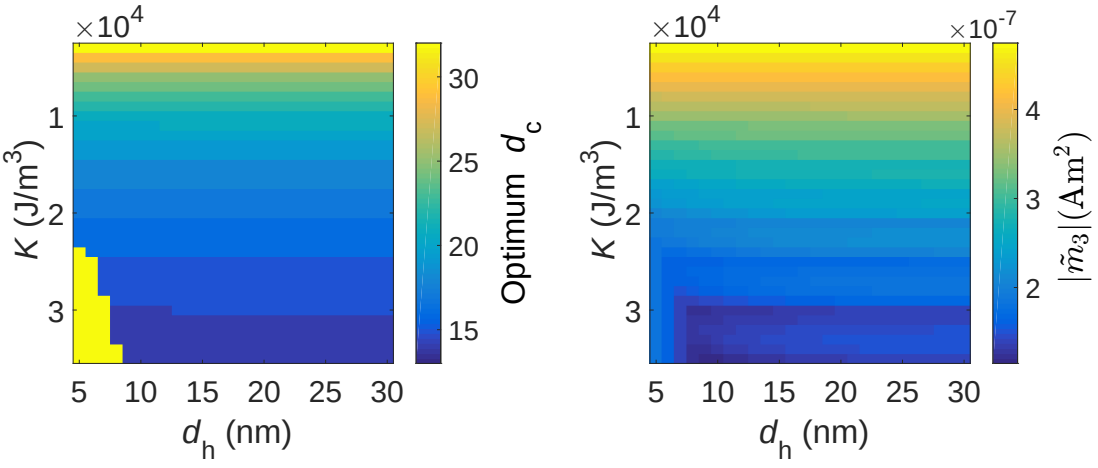

Figure 44: Optimum tracers for $f = 25$ kHz and $B_{\mathrm{Drive}} = 25$ mT. Left: Core sizes with the highest third harmonic amplitude $|\tilde{m}_3|$ for every combination of effective anisotropy constant and hydrodynamic shell thickness; Right: Third harmonic amplitude $|\tilde{m}_3|$ of respective optimum particle core sizes.

The particles with the largest $|\tilde{m}_3|$ are located in the area that rotates via the Néel mechanism and depend on the effective anisotropy constant. At an effective anisotropy constant of bulk magnetite $K = 10000\,\mathrm{J/m^3}$, particles of the size of about $d_{\mathrm{c}} = 21$ nm performed best, while for $K = 6000\,\mathrm{J/m^3}$ core sizes of about $d_{\mathrm{c}} = 25$ nm for $f = 25$ kHz and $d_{\mathrm{c}} = 24$ nm for $f = 125$ kHz are found to yield the highest $|\tilde{m}_3|$. Should it be possible to synthesize MNP with even lower effective

anisotropies, particle core diameters of up to $d_c = 35$ nm yield even stronger third harmonic amplitudes.

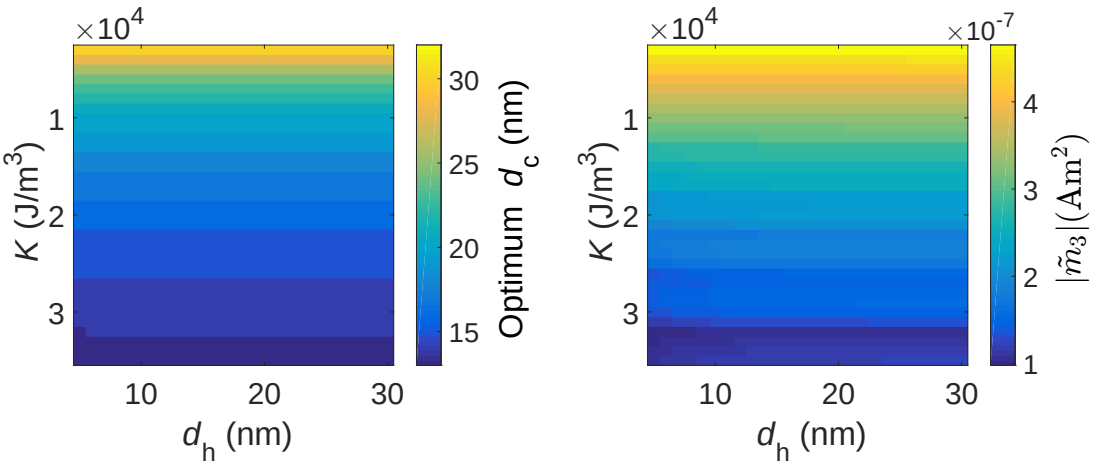

Figure 45: Optimum tracers for $f = 125$ kHz and $B_{\mathrm{Drive}} = 25$ mT. Left: Core size with the highest third harmonic amplitude $|\tilde{m}_3|$ for every combination of effective anisotropy constant and hydrodynamic shell thickness; Right: Third harmonic amplitude $|\tilde{m}_3|$ of respective optimum particle core size.

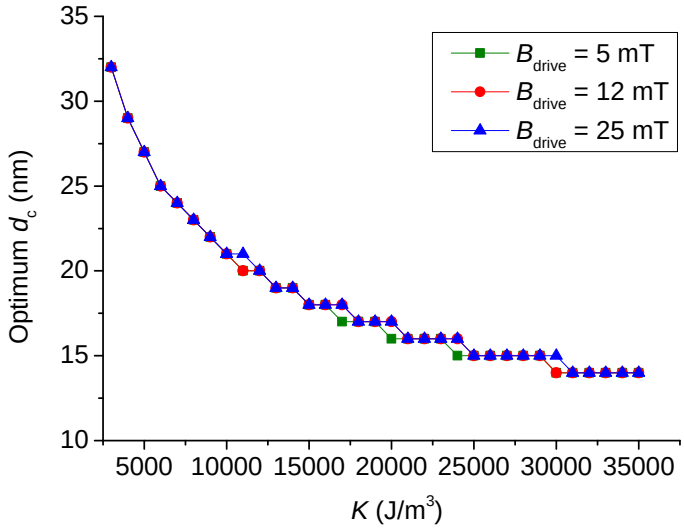

Figure 46: Difference in the optimum particle size for $f = 25$ kHz at different drive fields.

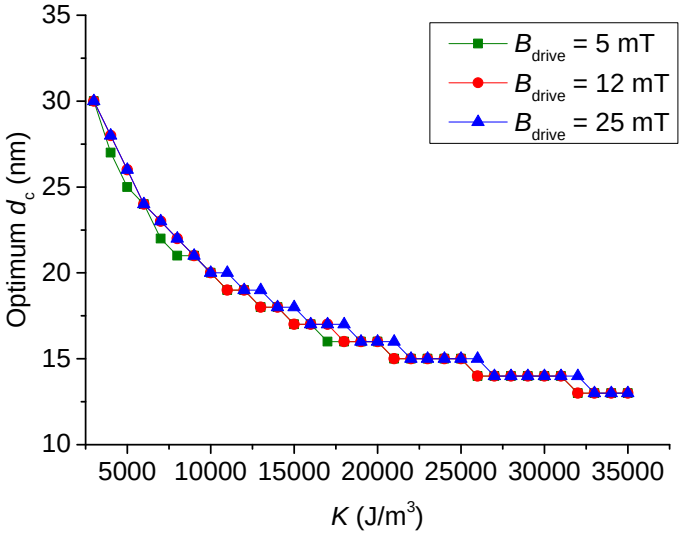

Figure 47: Difference in the optimum particle size for $f = 125$ kHz at different drive fields.

In direct comparison between the different drive field strengths and frequencies of the particles purely rotating via Néel (Fig. 46 and Fig. 47) it can be seen that the optimum particle size decreases for smaller drive fields as well as for larger frequencies. This should not come as a surprise as it was shown in (2.17) to (2.19) that the rotation time for Néel as well as for Brown decreases with stronger drive fields, therefore enabling larger particles to follow a strong field faster than a weak field. Simultaneously, a higher frequency means less available time for the rotation, making slightly smaller particle sizes preferable.

Given the reported effective anisotropy constant of $K = 6000\,\mathrm{J/m^3}$ of suitable MPI tracers [91], this seems like a realistic value to exemplarily investigate the full harmonic spectrum of monodisperse particles as well as of narrowly distributed monomodal particles with a small standard deviation $\sigma = 0.1$. This was done for $f = 25$ kHz, $B_{\mathrm{Drive}} = 25$ mT and $d_{\mathrm{h}} = 20$ nm. It was first investigated, how the spectrum in general and the $|\tilde{m}_3|$ in particular change over the core diameter for this comparably low, but still accessible, effective anisotropy constant. In Fig. 48, the absolute amplitudes of the third harmonic are plotted over d_{c}. It is conspicuous, that the $|\tilde{m}_3|$ slowly increases to a maximum at 25 nm and then suddenly drops by a factor of about 10 at 30 nm. This can be attributed to the exponential increase of the Néel relaxation time over V_{c} which results in a small regime of high particle performance where the magnetic moment on the one hand is large enough to generate a considerable signal but on the other hand the Néel reversal of the moment is still

fast enough to follow the drive field. In Fig. 49, it can be seen how the harmonic amplitudes of the whole spectrum, normalized to the respective maximum of each harmonic, change over the diameter. In the case of $K = 6000\,\mathrm{J/m^3}$, there is a fairly broad peak for lower harmonics, which gets sharper for higher harmonics. Furthermore, a shift in the maximum amplitude to smaller particles for higher harmonics can be observed. This indicates that core diameters slightly below the one yielding the highest $|\tilde{m}_3|$ may generate the shallowest decay of harmonic amplitudes and would therefore be better suited for MPI.

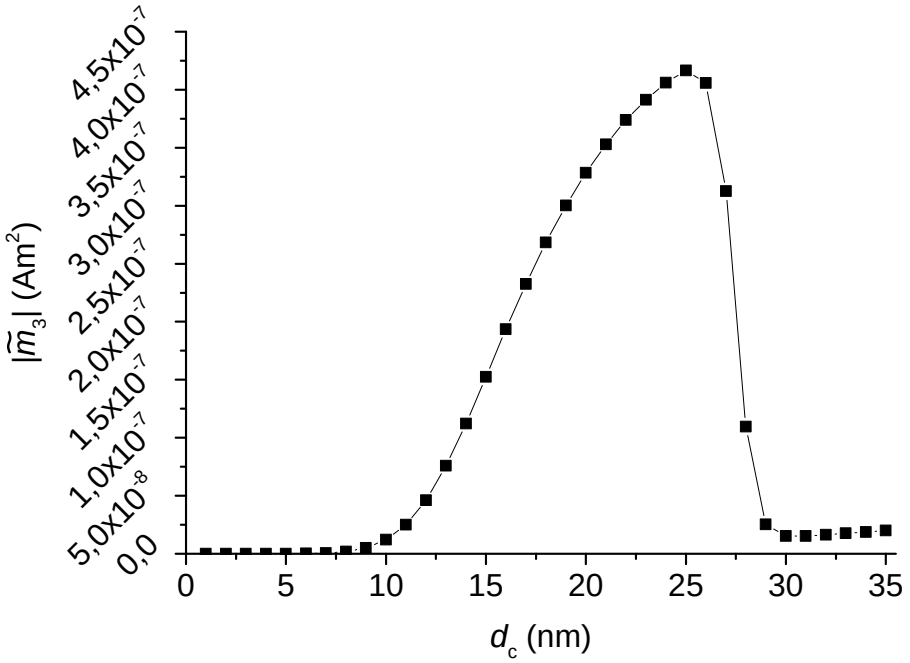

Figure 48: $|\tilde{m}_3|$ over the core diameter at $K = 6000\,\mathrm{J/m^3}$, $f = 25$ kHz, and $B_{\mathrm{Drive}} = 25$ mT.

Since the core sizes with the largest lower harmonics do not necessarily yield the largest higher harmonics, the complete harmonic spectra around the optimum core diameter for $|\tilde{m}_{3,\mathrm{max}}|$ were also investigated. The spectra of particles around this core size are depicted in Fig. 50 with monodisperse particles (left) and narrowly distributed monomodal particles (right). The spectra of 24 nm, 25 nm and 26 nm particles, all very similar in their $|\tilde{m}_3|$, have completely different harmonic decays with the 24 nm particles being the most shallow. For monomodal distributions of particle cores with a standard deviation of $\sigma = 0.1$, the distribution with a median of $\mu = 25$ nm does neither yield the shallowest spectrum nor the highest $|\tilde{m}_3|$, even though at this particle size it was largest for monodisperse particles. This is due

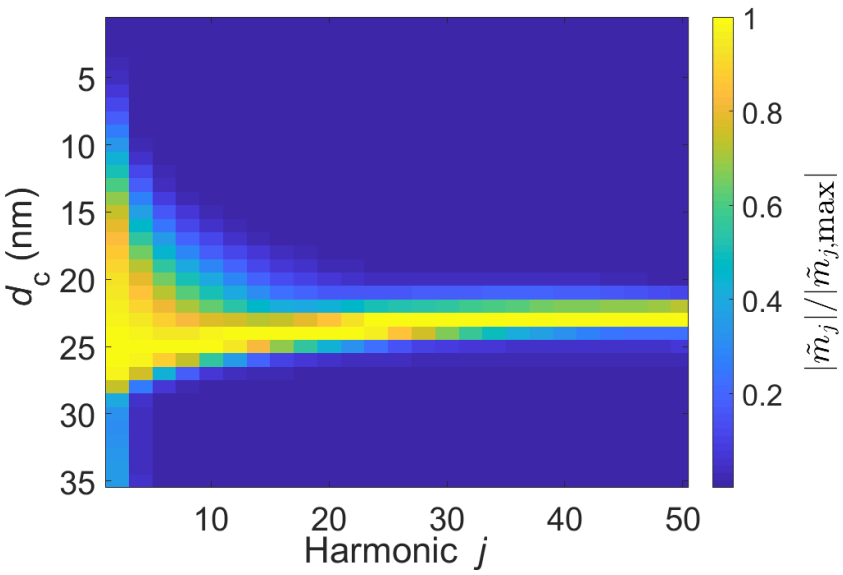

Figure 49: Normalized harmonic amplitude at $K = 6000\,\mathrm{J/m^3}$ and $B_{\mathrm{Drive}} = 25$ mT for $d_c = [1...35]$ nm.

to the sudden drop in amplitude visualized in Fig. 48 and the general decay of the harmonic amplitudes at this size. For the given parameters $K = 6000\,\mathrm{J/m^3}$, $B_{\mathrm{Drive}} = 25$ mT, $f = 25$ kHz $d_{\mathrm{h}} = 20$ nm and $\sigma = 0.1$, a median diameter of $\mu_{\mathrm{c}} = 23$ nm yields the highest $|\tilde{m}_3|$ and shallowest spectrum.

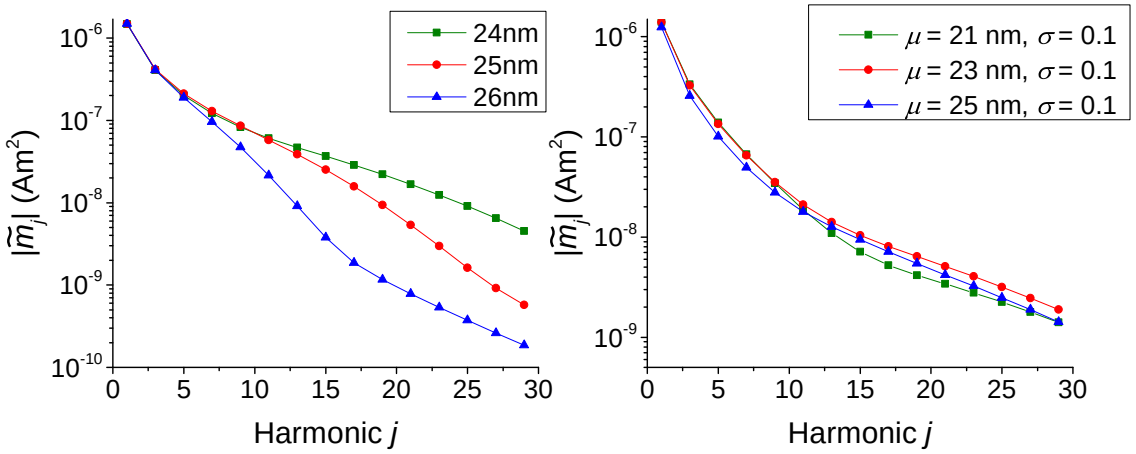

Figure 50: Simulated spectra in the optimum size range. Left: Monodisperse particles; Right: Narrowly distributed particles.

Since the assumption of narrowly distributed particles is far more realistic [56] [128], it was investigated how the $|\tilde{m}_3|$ and the $|\tilde{m}_5|/|\tilde{m}_3|$ ratio (as a measure for the harmonic decay) are influenced by the median core diameter for $\sigma = 0.1$. Furthermore, to better estimate the maximum MPS signal possible for the given parameters, the $|\tilde{m}_3|$ is normalized to the amount of iron. The result for $B_{\mathrm{Drive}} = 25$ mT can be seen in Fig. 51.

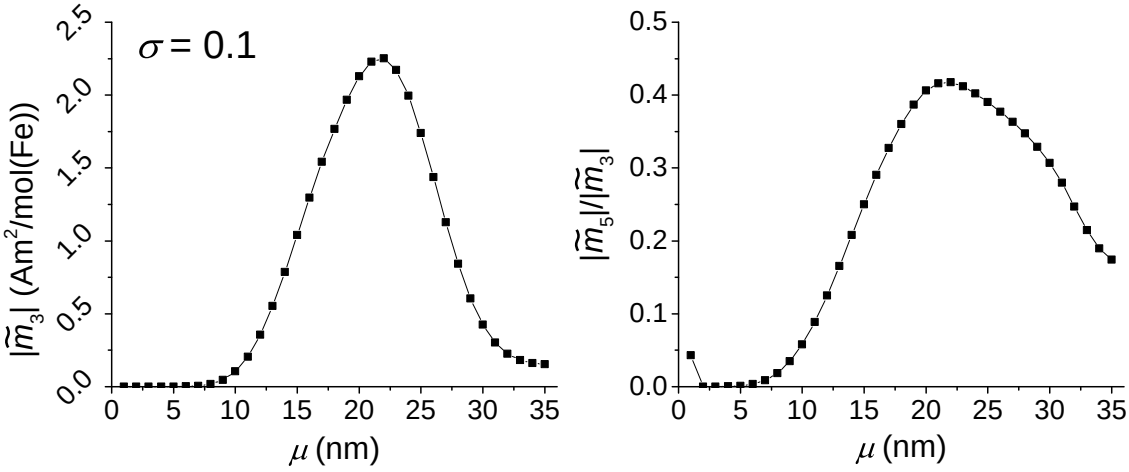

Figure 51: Left: Third harmonic amplitude over median diameter for narrowly distributed particle core sizes; Right: Ratio of fifth and third harmonic amplitude over median diameter for narrowly sized particle distributions

Maxima can be found between $\mu = 22$ nm and $\mu = 23$ nm for $|\tilde{m}_3|$ as well as for the $|\tilde{m}_5|/|\tilde{m}_3|$-ratio. The largest values that were reached for $K = 6000\,\mathrm{J/m^3}$ and $d_{\mathrm{h}} = 20$ nm were $|\tilde{m}_{3,\mathrm{max}}| = 2.25\,\mathrm{Am^2/mol(Fe)}$ and $|\tilde{m}_5|/|\tilde{m}_3|_{\mathrm{max}}$=0.42. This third harmonic amplitude corresponds to the 4.7 fold of FeraSpin R at $B_{\mathrm{Drive}} = 25$ mT or the 5.7 fold at $B_{\mathrm{Drive}} = 12$ mT. Given an MNP system with a so far unprecedented effective anisotropy constant $K = 1000\,\mathrm{J/m^3}$, a median diameter $d_{\mathrm{c}} = 39$ nm and a standard deviation $\sigma = 0.1$, the $|\tilde{m}_3|$ could be increased by a factor of 15.8 for 10 mT and 7.1 for 25 mT.

5.4. Extraction of parameter set for optimized MPI particles

The simulation of the dynamic magnetic moment to optimize particles for MPI has shown that the by far best performing particles can be found in the regime of Néel rotation. Depending on the external parameters frequency and drive field

as well as structural parameters, especially the effective anisotropy constant, the best results were obtained with particle cores around 25 nm. Given the values of $K = 6000\,\mathrm{J/m^3}$, $f = 25$ kHz and $B_{\mathrm{Drive}} = 25$ mT, the core diameter $d_{\mathrm{c}} = 25$ nm was made out to yield the largest third harmonic amplitude whereas $d_{\mathrm{c}} = 24$ nm yielded the shallowest harmonic decay.

It could also be observed that the harmonic spectrum dropped rapidly for particles slightly larger than the optimum diameter which is caused by the exponential increase of the Néel rotation time over the core volume. This is important for the more realistic assumption of at least narrowly distributed particle sizes rather than a perfectly homogeneous, monodisperse particle ensemble. Here, better results were obtained for distributions with a median diameter slightly below the optimum. The obvious reason is that a distribution of particle core sizes around the optimum diameter would also include particle cores above the optimum diameter, which have very limited contribution to the overall harmonic spectrum.

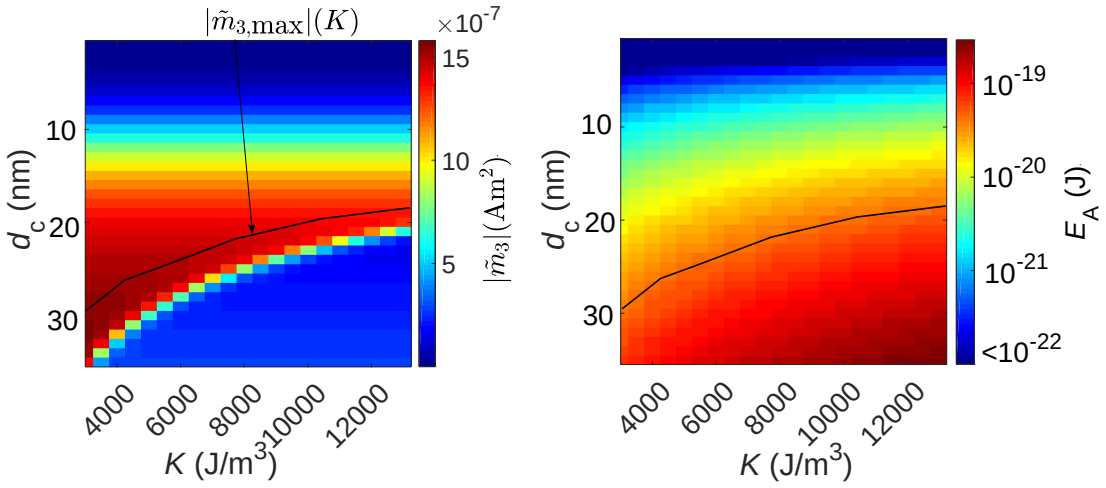

Figure 52: Maps of the third harmonic amplitude and effective anisotropy constant for $B_{\mathrm{Drive}} = 25$ mT and $f = 25$ kHz. Left: Third harmonic amplitude in dependence on core diameter and effective anisotropy constant. Along the black line are the largest third harmonic amplitudes for the respective value of K. Right: Anisotropy energy in dependence on the core diameter and effective anisotropy constant. The marked largest third harmonic amplitudes correspond to a nearly constant value of E_{A}.

.

Since the best results were obtained with particles following the Néel rotation, a strong dependency on the effective anisotropy constant was found. Given the equation for the zero field Néel relaxation time (2.8), the numerator of the expression, i.e. the anisotropy energy $E_\mathrm{A} = KV_\mathrm{c}$, needs to be minimized for the moments to quickly realign to the external field while simultaneously having a large core volume V_c to maximize the magnetic moment. This trade-off is visualized in Fig. 52. Here, the $|\tilde{m}_3|$ (left) and E_A (right) are depicted for a parameter set of core sizes and effective anisotropy constants up to $K = 13000\,\mathrm{J/m^3}$. The black line in both graphs represents the maximum achievable third harmonic amplitude for each value of K. Right, it can be observed that this value $|\tilde{m}_{3,\mathrm{max}}(K)|$ is always based on nearly the same anisotropy energy $E_\mathrm{A} \approx 5 \cdot 10^{-20}\,J$, which is therefore named the optimum anisotropy energy and the starting point of an analysis to obtain a generalized parameter set for optimized MPI particles.

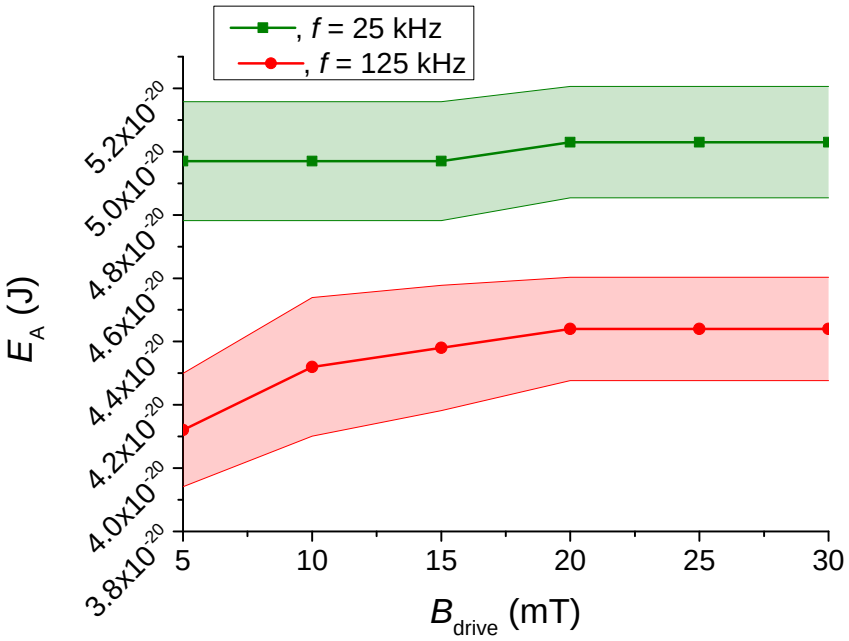

Figure 53: Mean optimum anisotropy energy and its standard deviation of ideal particle diameters to maximize $|\tilde{m}_3|$ at different drive fields amplitudes.

Of all the anisotropy energies along the black line in Fig. 53, a mean value and a standard deviation can be calculated. This procedure was repeated for applied drive field amplitudes $B_\mathrm{Drive} = 5...30$ mT and frequencies $f = [25, 125]$ kHz. For all $[B_\mathrm{Drive}, f]$ combinations, the mean value and standard deviations of the optimum anisotropy energy values were calculated and depicted in Fig. 53. In this depiction,

it can be observed that the respective mean values of E_A remain nearly constant over the drive field for each frequency and stay in very close boundaries of ±5% of its mean value.

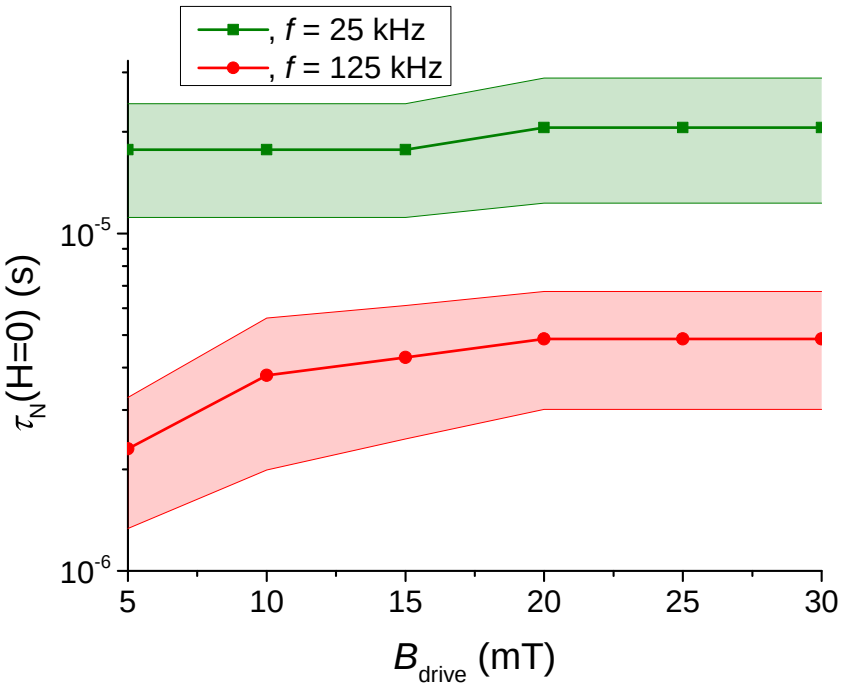

Figure 54: Zero field Néel relaxation times of optimum particles in dependence on the drive field amplitudes.

Based on these insights, all obtained values of the optimum anisotropy energy can be used to calculate the mean values and standard deviations of the respective zero field Néel relaxation times in dependence on the drive field (Fig. 54). Obviously, the relaxation times for higher frequencies need to be lower than for low frequencies as they have less time to realign to the external field. Therefore, the relaxation times for $f = 125$ kHz vary between 1 µs and 5 µs whereas they vary between 5 µs and 20 µs for $f = 25$ kHz. Again, the relaxation times remain in very close boundaries and except for $\tau_N(f = 125\,\text{kHz}, B_{\text{Drive}} = 5\ \text{mT})$ remain nearly constant over B_{Drive}.

The zero field relaxation times were employed to calculate the ratio between the characteristic frequency $f_{\text{char}} = 1/(\tau_N(H = 0))$ and the excitation frequency f (Fig. 55). Now the resulting values for f_{char}/f superpose each other for the two tested frequencies for $B_{\text{Drive}} > 5$ mT, yielding a general frequency independent parameter for the optimum MPI particles. The mean value of the necessary ratio remains nearly constant between 2 and 3 with decreasing standard deviations for larger drive fields.

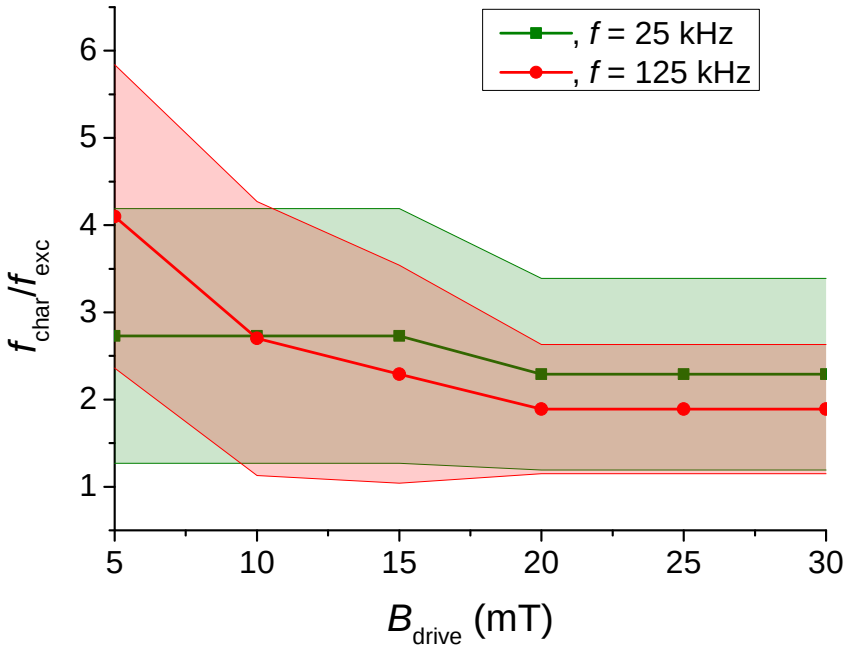

Figure 55: Ratio between characteristic frequency and excitation frequency.

Overall, this factor emerged as frequency- and mostly drive field independent parameter, that should be aimed for to maximize the particle performance in MPI. Ideally, this is achieved by minimizing the effective anisotropy constant and maximizing the particle diameter and thus, the magnetic moment.

5.5. Comparison with literature/Discussion of the results

This work was not the first to investigative the optimum size of MNP for MPI which is why it is crucial to compare these results to the ones in literature.

The most prominent works in literature concerning optimum particle sizes for MPI are done by Ferguson et al. [31] [32] [33] [34] [35] , mainly in terms of synthesis but also in terms of simulations. A consistency check with those works is therefore of utter importance to substantiate the results obtained here.

In one of their earlier works they predicted an optimum core size of $d_c = 15$ nm for $K = 25000\,\mathrm{J/m^3}$, $f = 50$ kHz and $B_{\mathrm{Drive}} = 10$ mT [35]. This frequency was not subject to this simulation study but when applying the mentioned parameters, the $|\tilde{m}_3|$ over d_c shows a clear peak at $d_c = 15$ nm exactly like predicted in literature.

In [34], they simulated the particle response for different effective anisotropy constants. For $K = 20000\,\mathrm{J/m^3}$, they found a maximum in the particle signal at a core size of around $d_c = 15$ nm, followed by a minimum and another increase of the signal. The same behavior was found in this work, where $|\tilde{m}_3|$ exhibits two maxima for large effective anisotropy constants, one for Néel rotation and one for Brownian rotation.

Since this group is very active in the field of particle synthesis [66] [65] [67], findings from this simulation are also compared to their experimental findings concerning optimum particle performance. In [31], they compared narrowly distributed ($\sigma = 0.2$) particles to each other to experimentally find the optimum particle size. Here they found optimum particle sizes at $d_c =\sim 25$ nm for $f = 25$ kHz, which they could confirm in [32]. Assuming an effective anisotropy constant that was found in [91] for particles that were synthesized by this group, this corresponds very well with the findings in this work as it was shown in Fig. 48. Another finding of their work in [31] indicated a negligibility of the Brownian rotation which was confirmed here, at least for particle configurations that are of interest for MPI. Overall, their findings in experiment and simulation match very well with this simulation.

When simulating the behavior of MNP (especially under the influence of quickly alternating fields) it should be kept in mind what the simulation method is capable of and which parameters and effects are ignored or simplified via effective values. In the case of this simulation, the shell thickness and the anisotropy, but also the composition of particle cores, were simplified. In chapter 2.1.8, the composition of particles as either single core or multi core particles, was introduced. Here, only non-interacting single core particles were simulated, but it was shown in [89] that single and multi core particles may exhibit different behaviors. This should be kept in mind, given that multi core particles may also be used as MPI tracers [27].

In terms of the hydrodynamic shell, a fixed thickness was presumed to limit the number of potential parameter combinations. However, the hydrodynamic shell thickness was often found to be a distribution of shell thicknesses just like the particle core size distribution [143] [101] [92] [86]. Still it should be kept in mind that the findings in this simulation, as well as the findings of Ferguson et al., indicate, that particles that are suitable for MPI primarily rotate via internal reversal of the magnetic moment and the Brownian rotation (which is directly affected by the hydrodynamic diameter) is mostly negligible.

The anisotropy directly influences the reversal of the magnetic moment via Néel rotation. For this simulation, an effective value of the anisotropy has been presumed like it is typically done for the characterization of for MPI tracers [92] [88]. Due to this simplification an effect can not be reproduced that was simulated by Weizenecker [141]: He showed that not only can a small anisotropy increase the MPI signal, the signal is also influenced by the ratio between easy and hard anisotropy axis. Furthermore was the possibility of a distribution of effective anisotropy constants *a priori* excluded and replaced by a fixed value.

These simplifications on the other hand enable a nearly instantaneous calculation of several periods of the magnetic moment, whereas a more sophisticated approach like the Landau-Lifshitz-Gilbert-Equation is far more CPU-intensive [80], making a parameter study like this very difficult.

In the next chapter, a method will be proposed that enables the characterization of MPI tracers regarding their potential spatial resolution without time consuming MPI phantom experiments. It will therefore now be investigated how the zero offset MPS spectrum, that was simulated in this chapter, influences the resolution quantitatively.

6. Resolution characterization of MPI tracers employing offset field supported MPS

In the last chapters, the roles of the MPS spectrum and the MTF were examined, leading to the conclusion that in MPI, a direct relationship between achievable resolution and SNR is present. Furthermore, the dynamic behavior of single-core MNP was simulated to find a particle size that yields the highest possible MPS spectrum dependent on the effective anisotropy constant and hydrodynamic shell thickness and therefore maximizes the SNR. In this chapter, a method will be presented for a quantitative characterization of MPI tracers regarding the line resolution dependent on the SNR, which will be applied on the tracers characterized in Chapter 3. To that end, the basic concept of the imaging characterization method will be presented, followed by the development of suitable software phantoms. Besides the characterization, the method will further be applied on an imaging setup where the system function differs from the MPI signal due to changes of the tracer behavior. Lastly, the principle will be applied on a 2D setup and a comparison to actual MPI phantom experiments will be performed to validate this method.

6.1. Development of an offset field supported imaging characterization

It has been shown in the last chapters that the MPI imaging performance and the MPS spectrum are correlated, meaning that a shallow MPS spectrum with large amplitudes (normalized to the iron content) indicates a potentially suitable MPI tracer. However, lacking the field gradient of MPI, it is not possible to make quantitative predictions about the potential resolution just based on MPS measurements. In the measurement technique presented here, the lack of the field gradient is compensated with the application of static offset fields, mimicking the field gradient employed in 1D MPI imaging. This approach corresponds to the Hybrid System Function approach [49], which has already been used to reconstruct 1D MPI data [51].

6.1.1. Concept

The fundamental idea of the offset field supported MPS measurements is visualized in Fig. 56. The magnetic field gradient G in an MPI setup describing the continuous location dependent offset field $B_{\text{off}}(x) = -Gx$ (left) can be approximated by a series of step functions with the center of each step plateau being located at the center of an image voxel (right) [49] [51]. Given that in MPI the offset fields at the edges of

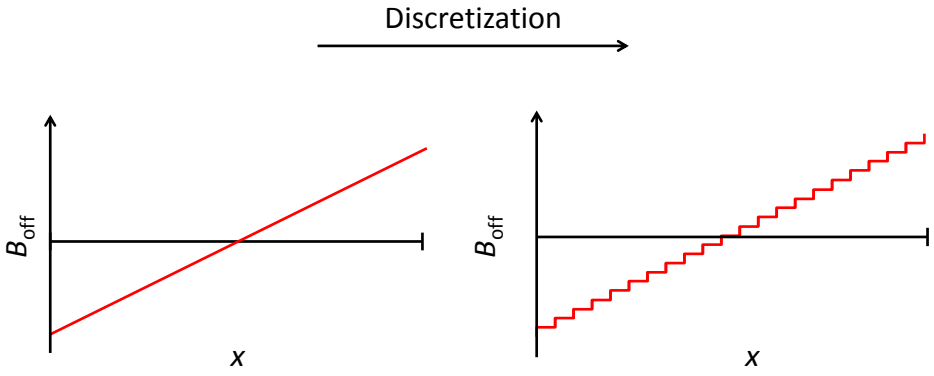

Figure 56: Discretization approach for sequential system function measurement. A sequence of step functions mimics the gradient field by forming a quasi-continuous gradient field.

the FOV correspond to the positive and negative drive field amplitude

$$B_{\text{off}}\left(\pm\frac{1}{2}l_{\text{fov}}\right) = \pm B_{\text{Drive}} \tag{6.1}$$

a 1D system function may also be compiled from a series of MPS measurements in the presence of static magnetic offset fields covering this field range. System functions obtained by MPS will exhibit a much better signal to noise ratio (SNR) due to the lower background noise level W of the MPS device, which in this case is about $W = 2 \cdot 10^{-12}\text{Am}^2$.

With the characteristic response at every location in the FOV, the spectra can further be employed to simulate 1D MPI signals of synthetic particle distributions.

In Fig. 57, the principle is depicted for a simple particle distribution consisting of a broad dot with decreasing particle density at the edges (top left). In this example, the gradient field is discretized into 31 step functions of different offset fields (bottom left). Therefore, the artificial MPI signal can be described by the superposition of 31 measured spectra at the respective offset fields, weighted with the iron amounts $N_{\mathrm{mol},1}...N_{\mathrm{mol},31}$, corresponding to the amount of particles at every discretized location (right).

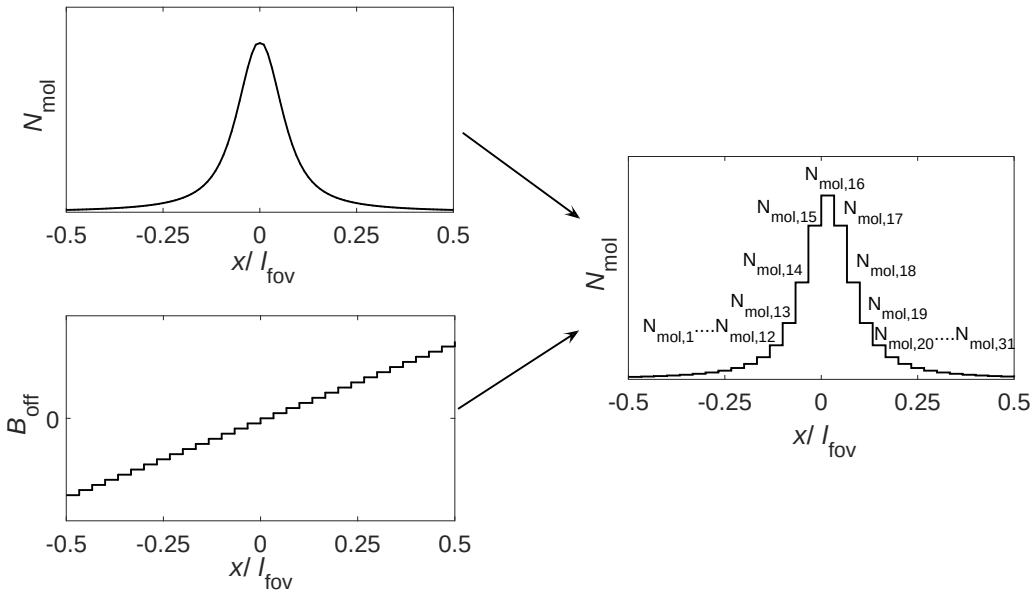

Figure 57: Generation of the synthetic MPI signal. A defined particle distribution (top left) is discretized according to the discretization mesh of the gradient field (bottom left). The synthetic MPI signal is generated by summing up the measured spectra at the respective offset fields, weighted with the corresponding particle amount N_{mol} (right).

Hence, the generation of the synthetic MPI signal s can be described via:

$$s_{\mathrm{MPI}} = \sum_{i=1}^{I} N_{\mathrm{mol},i} \frac{A_i}{V c_{\mathrm{Fe}}} + W \tag{6.2}$$

with $N_{\mathrm{mol},i}$ as the iron content at the location i of the virtual particle distribution, A_i as the corresponding row of the MPS measured system function, V and c_{Fe} as volume and iron concentration of the measured reference sample, and W as the artificially amplified noise if the MPI signal is to be simulated under certain noise conditions.

For this method, a close-meshed system function is ideal to also be able to generate MPI software phantoms of small details and to ensure a smooth tracer distribution without sharp edges. However, the reconstruction should not be performed using the same system function to avoid an inverse crime [62]. Therefore, a second, reduced system function is measured to reconstruct the tracer distribution. The number of spectra in this reduced system function corresponds to the number of voxels of the reconstructed image. Henceforth, the two system functions will be called signal generation system function $\mathbf{A}_1$ and reconstruction system function $\mathbf{A}_2$.

Having established a principle to generate synthetic MPI signals of defined particle distributions based on MPS measurements under influence of an adjustable offset field, next, how the principle may be used to obtain imaging parameters will be discussed.

6.1.2. Phantom development

Having established the basic method of measuring the 1D system function with an MPS that is equipped with an offset magnet and generating synthetic MPI signals based on these measurements, it is also important to define phantoms and a simulation procedure to characterize the imaging performance of a tracer.

A simple phantom to test the resolution consists of two separate objects with a gap in between. The objects are then moved towards each other and the resolution is defined as the gap that barely allows the objects to be distinguished in the reconstructed image. This procedure may be done at different SNRs to identify its relationship with to resolution. However, if the feasibility to reconstruct fine structures is to be tested, it may be necessary to vary the tested object sizes not only to investigate smaller structures, but also to take the lower iron content into account. A phantom that incorporates both methods is the Line Pair Gauge in Fig. 58, a resolution phantom that is well-established in medical imaging, including Magnetic Resonance Imaging [57], X-Ray [124], or Fluoroscopy [132]. The two

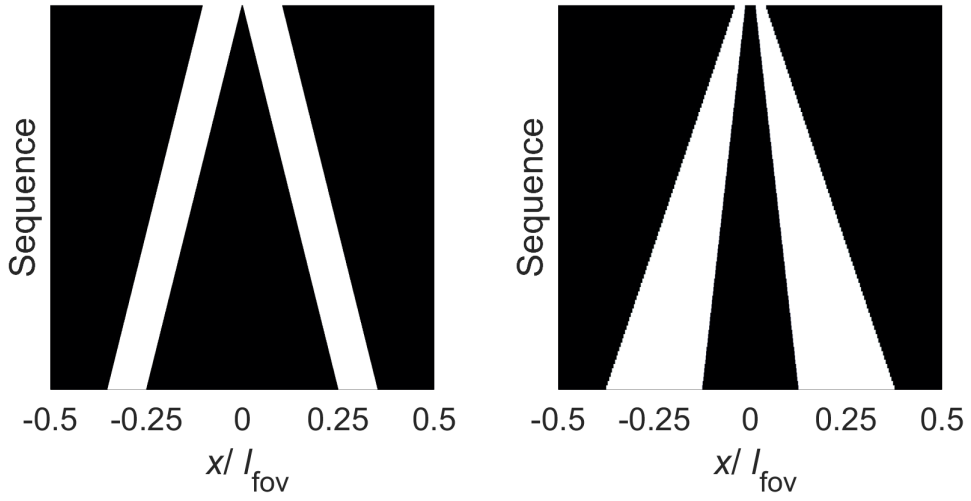

Figure 58: Line Pair Gauge resolution phantom without (left) and with (right) variable object diameter.

possible phantom types depicted here are: 1) a phantom with a constant object size independent of their distance (Fig. 58, left); and 2) a phantom with variable object size equivalent to the gap width (Fig. 58, right).

In the 1D case, the full 2D Line Pair gauge obviously cannot be imaged at once. It is therefore necessary to split the phantom into several 1D cross-sections of the Line Pair Gauge that are successively reconstructed to obtain the line resolution. This raises the question of how to handle the 1D character of the sequences in terms of a virtual volume.

According to (6.2), each measured spectrum is weighted with the corresponding iron content at the FOV location. Hence, a virtual height and depth of each cross-section will be presumed to take the iron content of the virtual distribution into account. This is visualized in Fig. 59. The particle filled parts of each cross-section have a certain width a along the FOV. This width is also assumed for a virtual depth and height, yielding two cubic objects with an edge length a as well as distance between each other for each cross-section. The virtual volume of each simulated particle cube is therefore a^3. The iron amounts $N_{\mathrm{mol},i}$, with which each spectrum is weighted, depend on the volume of each slab, indicated via the dashed lines. When a decreases with each cross-section like in Fig. 58 (right), the respective iron content per line pair decreases with $N_{\mathrm{mol},i}$ as well as with the number of slabs per cross-section, decreasing the SNR in the process.

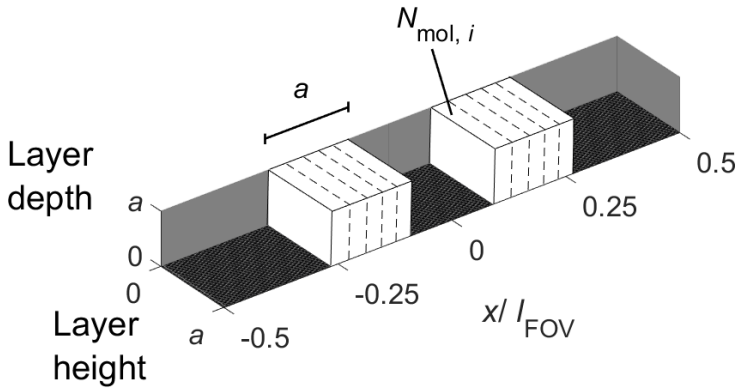

Figure 59: Simulation of a single 1D sequence. Left: Magnification of the first sequences of the Line Pair Gauge with the first one being selected. Middle: Selected cross-section in 1D side view. The virtual height corresponds to the width a which, in turn, depends on the sequence of the Line Pair Gauge. Right: The 1D sequence is treated as a 3D sequence with a virtual depth and height a. The virtual volume of each simulated particle filled object is therefore a^3.

Employing this volume, the iron amount $N_{\mathrm{mol},i}$ for each discrete location can be calculated under the assumption of a location dependent dimensionless filling factor F_i that is varied between 0 and 1 and an iron concentration $c_{\mathrm{Fe},i}$ that is to be assumed in the phantom segment i:

$$N_{\mathrm{mol},i} = F_i \frac{l_{\mathrm{fov}}}{I} a^2 c_{\mathrm{Fe},i} \tag{6.3}$$

Inserting (6.3) into (6.2), one obtains

$$s = \sum_{i=1}^{I} \Bigg(\underbrace{F_i \quad \underbrace{\frac{l_{\mathrm{fov}} a^2}{VI}}_{\text{Volume ratio}} \quad \underbrace{\frac{c_{\mathrm{Fe},i}}{c_{\mathrm{Fe}}}}_{\text{Concentration ratio}}}_{\text{Prefactor } \kappa_i} A_{1,i} \Bigg) + W. \tag{6.4}$$

The total synthetic MPI signal is therefore composed of the summed up measurement spectra, each weighted with a prefactor κ_i which depends on the filling factor F_i of the FOV segment in the virtual volume, as well as the volume and concentration ratio between FOV segment and MPS reference measurement. For practical

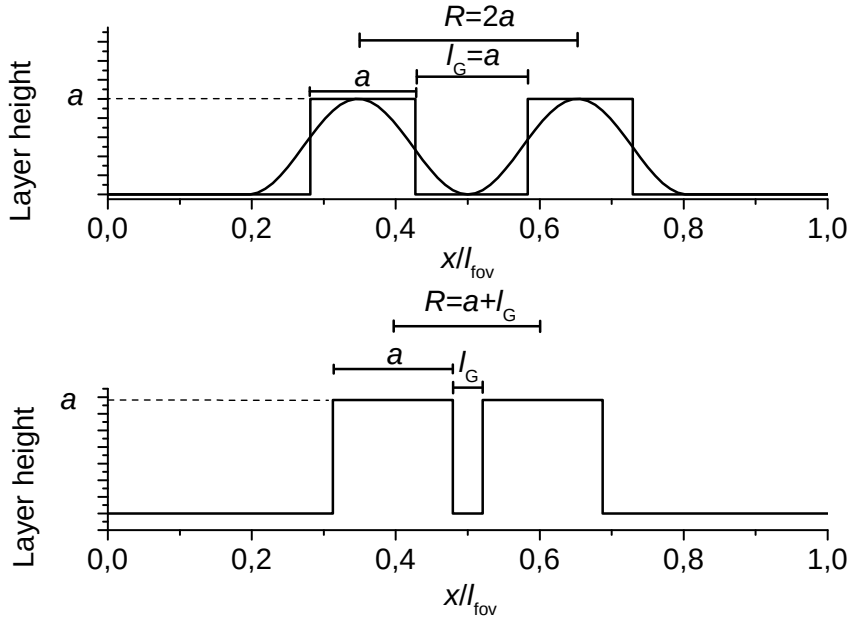

Figure 60: Top: Sinusoidally-shaped distribution in comparison to square-shaped distribution. The edge length (or width at half the maximum in case of the sinusoidally-shaped phantoms) always corresponds to the gap between the objects. The resolution R corresponds to the distance between the object centers or twice the gap length l_{G}. Bottom: Phantom with constant edge length. The distance between the object centers is $R = a + l_{\mathrm{G}}$.

reasons, the Line Pair Gauge usually consists of square waves when used as a physical phantom. However, the Line Pair Gauge is used here as a software phantom and the shapes can be changed at will. Since it has been reported in [125] that the square wave Line Pair Gauge slightly overestimates the resolution, the characterization with variable object size will also be performed using sinusoidally-shaped distributions (see Fig. 60 top). The resolution R is defined as the distance between the centers of the two virtual objects, corresponding to the length of one line pair (one full positive and one full negative contrast) or twice the length of the gap l_{G} between the objects. The characterization with phantoms with constant object sizes will be performed with square-shaped phantoms only. Contrary to the phantoms with variable object size, the gap width l_{G} is not scaled with the phantom width a

(Fig. 60 bottom). Here, a definition of the resolution as the distance between the object centers does not seem appropriate. To keep the definitions consistent, it will still be called R, but the characterization will additionally include l_{G}.

The virtual depth and height of sinusoidally-shaped phantoms is defined as the width at half the maximum that corresponds to the width of the cubic objects. Using this definition for the phantom volumes, the volumes of the cubic and sinusoidal waves are nearly identical (Fig. 61).

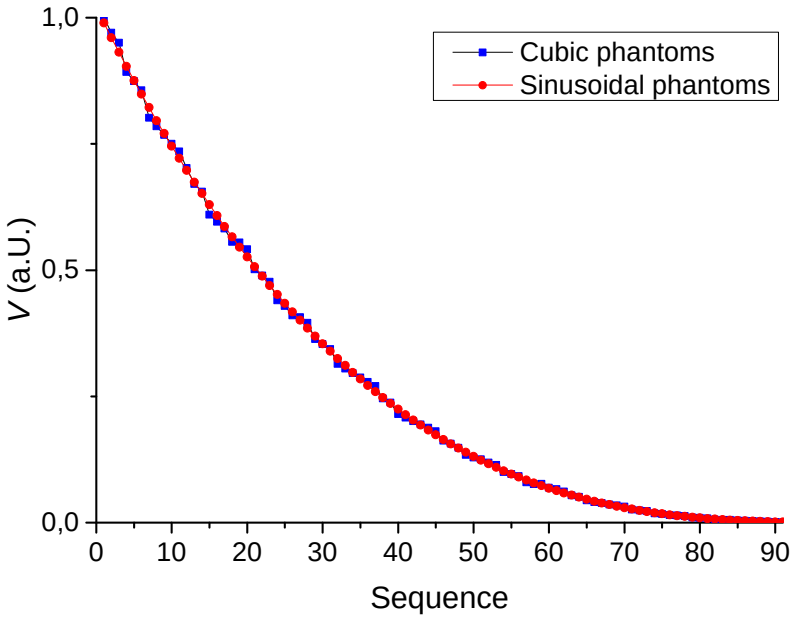

Figure 61: Comparison of tracer volume per sequence of the Line Pair Gauge for cubic and sinusoidal phantoms.

6.1.3. Characterization procedure

Of these particle distributions, synthetic MPI signals of tracers with a given concentration are generated. The signals are then artificially contaminated with Gaussian noise and the harmonics of the MPI signal that dropped below noise level are cut off. See Fig. 62 for an exemplary MPI signal: In this case, the spectrum drops at approximately the 22nd harmonic below noise and only harmonics lower than that are included in the reconstruction. Then, the resolution limit for this noise level is investigated by analyzing all reconstructed sequences of the Line Pair Gauge. By gradually raising the noise level, different resolution limits for different SNRs are obtained, yielding a characteristic resolution in dependence on the noise for a certain

tracer concentration. The final result of the characterization procedure may then be plotted as the mentioned resolution over noise or as the reconstructed image of the full Line Pair Gauge to obtain an optical impression of the achievable image quality at a given noise level.

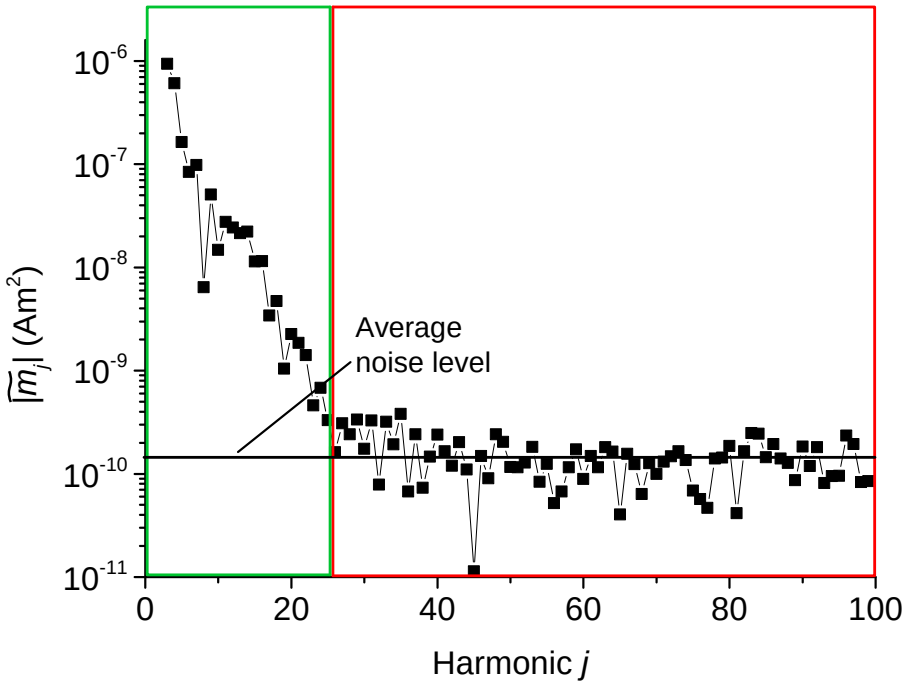

Figure 62: Choice of the number of harmonics in the reconstruction process. Harmonics that drop below noise level are not considered for reconstruction (red).

To reconstruct the particle distribution from MPI signals that contain noise, a criterion was defined to select harmonics to be employed for reconstruction by evaluating the SNR in the reconstructed images. Thus, a ratio is calculated between the maximum nominal particle content $\rho_{\max}$ (dashed line in Fig. 63) and the mean reconstructed particle content at the edges of the FOV that are known to nominally be particle free. For this ratio, a threshold was set to $\vartheta > 10$, which is arbitrary but seemed reasonable, and had to be satisfied by the reconstructed particle distribution at the resolution limit. If this threshold was violated (Fig. 63 top) and the reconstructed image exhibits several artifacts, the highest harmonic of the noise contaminated signal were truncated until the threshold was satisfied (Fig. 63 bottom).

As a summary of this section, a block diagram of the procedure is depicted in Fig. 64.

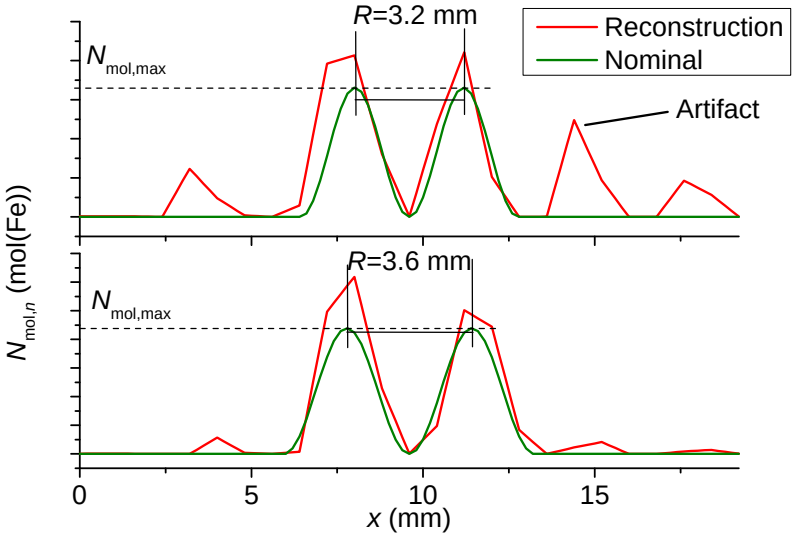

Figure 63: Two reconstructions with different noise contaminations. Top: High noise contamination with clearly visible artifacts. This reconstruction would not be considered for the evaluation. Bottom: Low noise contamination with slightly lower resolution. This reconstruction would be considered for evaluation.

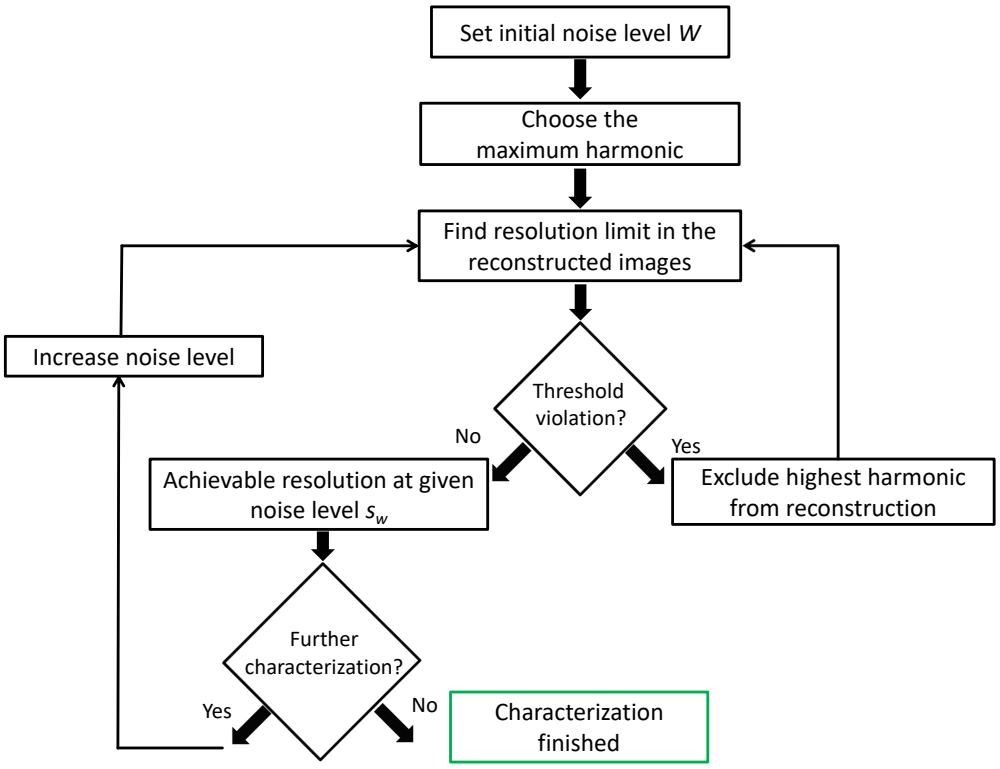

Figure 64: Block diagram of the characterization procedure.

6.2. 1D tracer characterization

In this section, the seven tracers of the FeraSpin series will be characterized regarding their potential resolution with the characterization method described above. The MPS measurements are performed using the following parameters:

- $c_{\mathrm{Fe}} = c_{\mathrm{Fe},i} = 50$ mmol/L
- $V = 30$ µL
- $B_{\mathrm{Drive}} = 12$ mT
- $f = 25.25$ kHz
- $T = 310$ K

For the characterization, a gradient strength of $G = 1.25$ T/m is assumed. Employing (4.1), the size of the virtual one-dimensional FOV is given by $l_{\mathrm{fov}} = 24/1.25\frac{\mathrm{mT}}{\mathrm{T/m}} = 19.2$ mm. The reconstruction is performed employing the nonnegative Kaczmarz algorithm (2.37) with 20 iteration steps. The system functions for signal generation

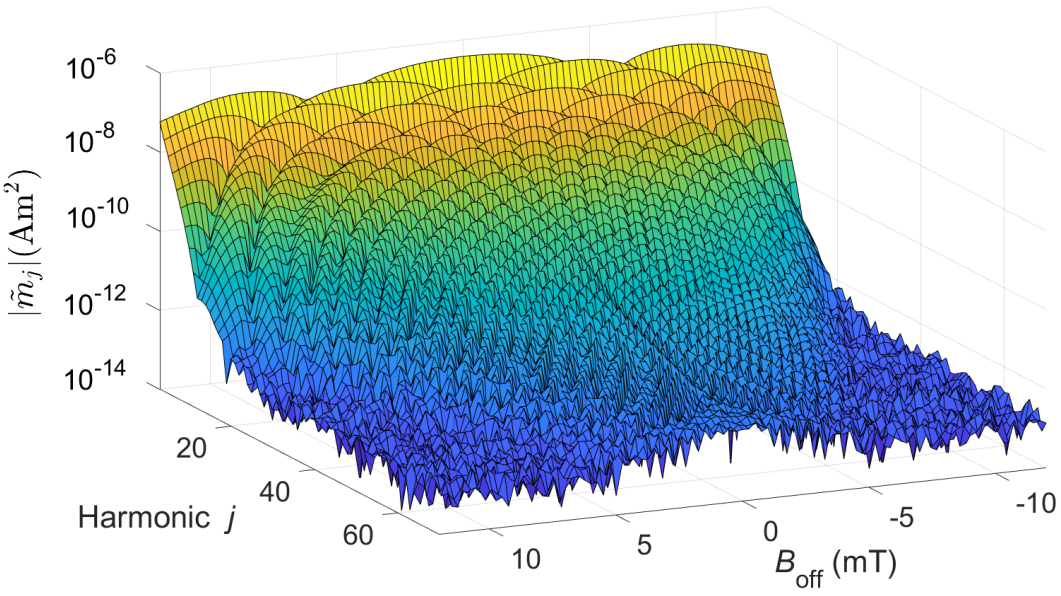

Figure 65: Measured 1D system function of FeraSpin R. The color map is used to better distinguish the harmonics from each other.

$\mathbf{A}_1$ and for reconstruction $\mathbf{A}_2$ are discretized with increments of $B_{\text{incr},1} = 0.25$ mT and $B_{\text{incr},2} = 1.00$ mT and measured separately, corresponding to 97 spectra and 25 voxels. Thus, structures as small as $19.2\,\text{mm}/25 = 0.768$ mm could theoretically be reconstructed, which corresponds to three signal generating spectra.

In Fig. 65, the system function $\mathbf{A}_1$ of FeraSpin R, consisting of 97 spectra, can be seen. In this depiction, the magnitude of each harmonic is plotted over the offset field. In comparison with the simulated system function in Fig. 20, a strong agreement of the general curve shape can be observed. The color map is used to better distinguish the harmonics from each other.

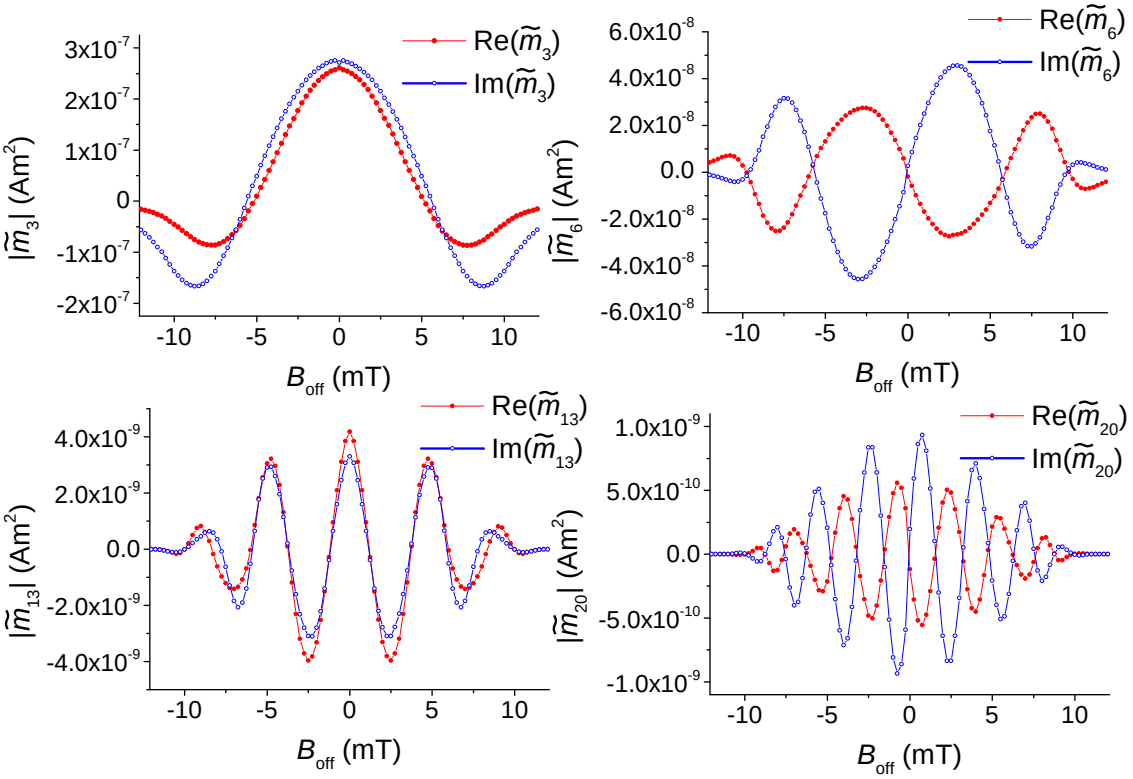

Figure 66: Real and imaginary part of 3rd, 6th, 13th, and 20th harmonic, measured at different offset fields.

In Fig. 66, the real and imaginary values of single harmonics from the measured system function of the tracer FeraSpin R are depicted. These measured harmonics are plotted over the offset field, but may as well be projected on a FOV. From the number of extrema (or corresponding to that: the harmonic number) of the highest harmonic included in the reconstruction, the extrinsic resolution can be calculated using the principle described in section 4.2. To validate this theory, the

following characterizations will be compared with predictions based on the spatial frequencies.

Before beginning with the characterization of different tracers, the prediction of the resolution based on spatial frequencies is performed without added Gaussian noise by generating synthetic MPI signals according to (6.2) and removing one harmonic at a time. FeraSpin R and the sinusoidal shapes with variable sizes were used as a phantom.

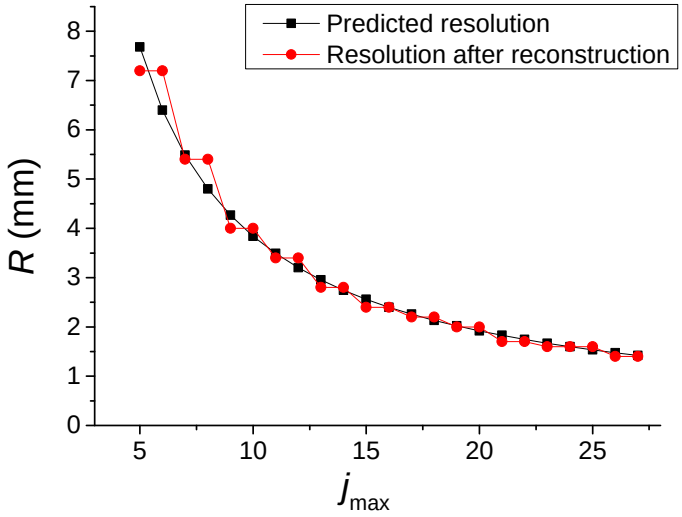

Figure 67: Achievable resolution in dependence on the number of employed harmonics. The Line Pair Gauge procedure is applied without addition of noise. Instead, the achievable resolution was evaluated by repeatedly removing harmonics from the signal prior to reconstruction.

The result can be seen in Fig. 67. By repeatedly removing the highest harmonic of the MPI signal, the achievable resolution was found to decrease with each reconstruction and fits very well with the theoretical prediction according to (4.3). The mean deviation between reconstructed and predicted resolution was found to be 4%.

6.2.1. Characterization results for phantoms with variable object sizes

The results of the resolution characterization of FeraSpin R of both sinusoidal and cubic phantoms are depicted in Fig. 68. The results for the other six tracers can be found in Appendix B. Here, the predicted resolution based on the highest

harmonic included in the reconstruction (under the condition of $\vartheta > 10$ for the SNR in the reconstructed images between maximum nominal iron amount and mean reconstructed iron amount at the edges of the FOV) can be seen in comparison with the experimentally derived resolution for the sinusoidal and square phantoms. In comparison with the noiseless case, the deviations between reconstruction and prediction when subjected to Gaussian noise were only very slightly higher than in the noise-free case. For the sinusoidally-shaped distributions, a mean deviation of 5% was found, whereas the mean deviation for square phantoms was found to be approximately 6.4%. The deviations grew larger with a higher noise level at approximately $W = 1 \cdot 10^{-8}\,\mathrm{Am}^2$ (best seen in the results in the appendix). A tendency that the square Line Pair Gauge overestimates the resolution, as reported in [125], could not be reproduced and sinusoidal as well as square phantoms resulted in similar resolutions.

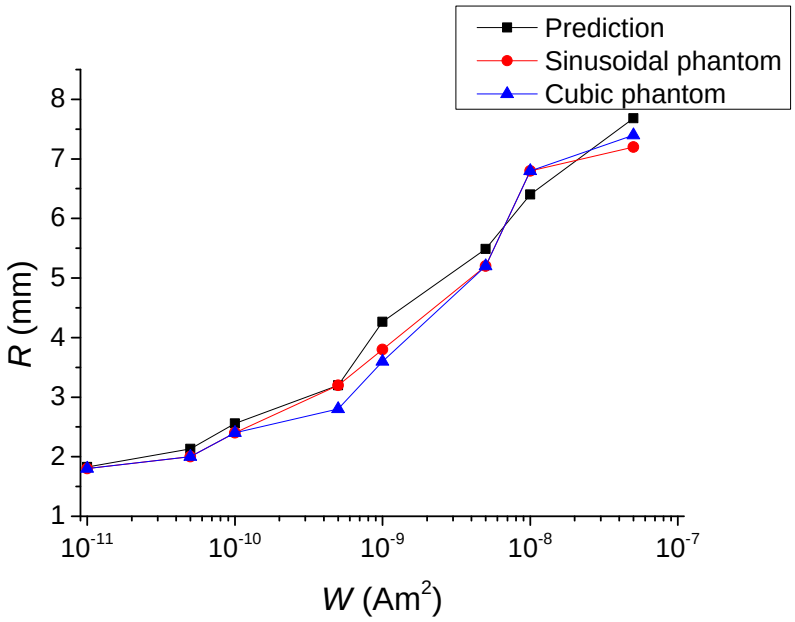

Figure 68: Resolution characterization of FeraSpin R.

To explore the limits of the resolution for a realistic set of parameters at the given field and gradient strength, the measured resolutions obtained here are further compared with simulated particles based on the results from section 5.3. Here, the log-normally distributed particles were simulated with the following parameter set:

- $K = 6000\,\mathrm{J/Am}^3$
- $d_\mathrm{h} = 20$ nm

- $\mu = 23$ nm
- $\sigma = 0.1$

The result can be seen in Fig. 69. In comparison with the other characterized particles, the improvement in the resolution is not as large as one might have expected since the $|\tilde{m}_3|$ is nearly three times as high as the one of FeraSpin XL and nearly six times higher than the one of FeraSpin R. Still, it should kept in mind that harmonic amplitudes six times higher means they tolerate a noise level six times higher for the same SNR. Given a drop of harmonic amplitudes over several decades over the course of the first 20 harmonics, a factor of six might only result in a few additional harmonics in the reconstruction process for a given noise level and therefore only a slight improvement of the resolution.

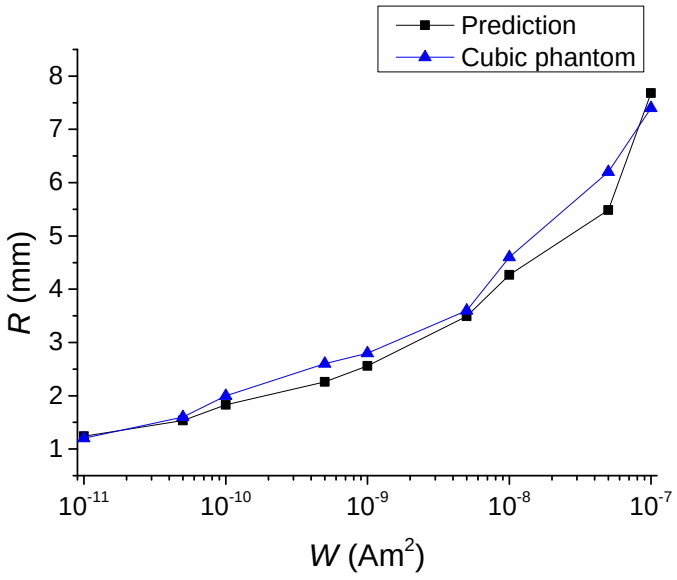

Figure 69: Resolution characterization for simulated particles.

An overview of the highest tolerated noise level as well as the results for chosen noise levels of the sinusoidal phantoms can be found in Tab. 3, where it should again be noted that the given resolutions describe the distance between the centers of two objects. The achievable resolution improved from FeraSpin XS to FeraSpin L, XL, and XXL. FeraSpin XS reached the maximum noise level to be able to resolve at least the most distant objects of the Line Pair Gauge at $W = 1 \cdot 10^{-10}\,\mathrm{Am}^2$. For FeraSpin S, this limit was reached at $W = 1 \cdot 10^{-9}\,\mathrm{Am}^2$ and for FeraSpin M, no phantom was resolvable at $W = 1 \cdot 10^{-8}\,\mathrm{Am}^2$. With FeraSpin L to XXL, it was

possible to resolve at least the most distant objects for the entire range of tested noise levels up to $W = 1 \cdot 10^{-7}\,\mathrm{Am}^2$.

Tracer	Max. tolerated noise (Am^2)	$R(W = 1 \cdot 10^{-11})\,(\mathrm{Am}^2)$ (mm)	$R(W = 1 \cdot 10^{-9})\,(\mathrm{Am}^2)$ (mm)
FeraSpin XS	$1 \cdot 10^{-10}$	4.4	-
FeraSpin S	$1 \cdot 10^{-9}$	2.6	7.6
FeraSpin M	$1 \cdot 10^{-8}$	1.9	4.2
FeraSpin R	$5 \cdot 10^{-8}$	1.8	3.8
FeraSpin L	$1 \cdot 10^{-7}$	1.4	3
FeraSpin XL	$1 \cdot 10^{-7}$	1.4	3
FeraSpin XXL	$1 \cdot 10^{-7}$	1.4	3
Simulation	$1 \cdot 10^{-7}$	1.2	2.8

Table 3: Characterization results for sinusoidally-shaped phantoms for chosen noise levels.

A way to evaluate the image quality at a given noise level directly in the image is shown in Fig. 70. Here, the whole Line Pair Gauge, composed of all reconstructed sequences, is depicted for a noise level of $W = 1 \cdot 10^{-10}\,\mathrm{Am}^2$. When only very large objects of several mm edge length are reconstructed, there is already a very strong influence of the noise on the reconstruction with FeraSpin XS; whereas there is nearly no difference in the reconstruction for S to XXL at this particular noise level. However, for smaller details, beginning at about sequence number 60, the results begin to differ and FeraSpin S and M reach their respective resolution limit at about sequence 65. While FeraSpin R reaches its resolution limit at sequence 80, the Line Pair Gauges of FeraSpin L to XXL can be nearly completely reconstructed at this noise level.

In the next section, a general evaluation of the results obtained here will be performed.

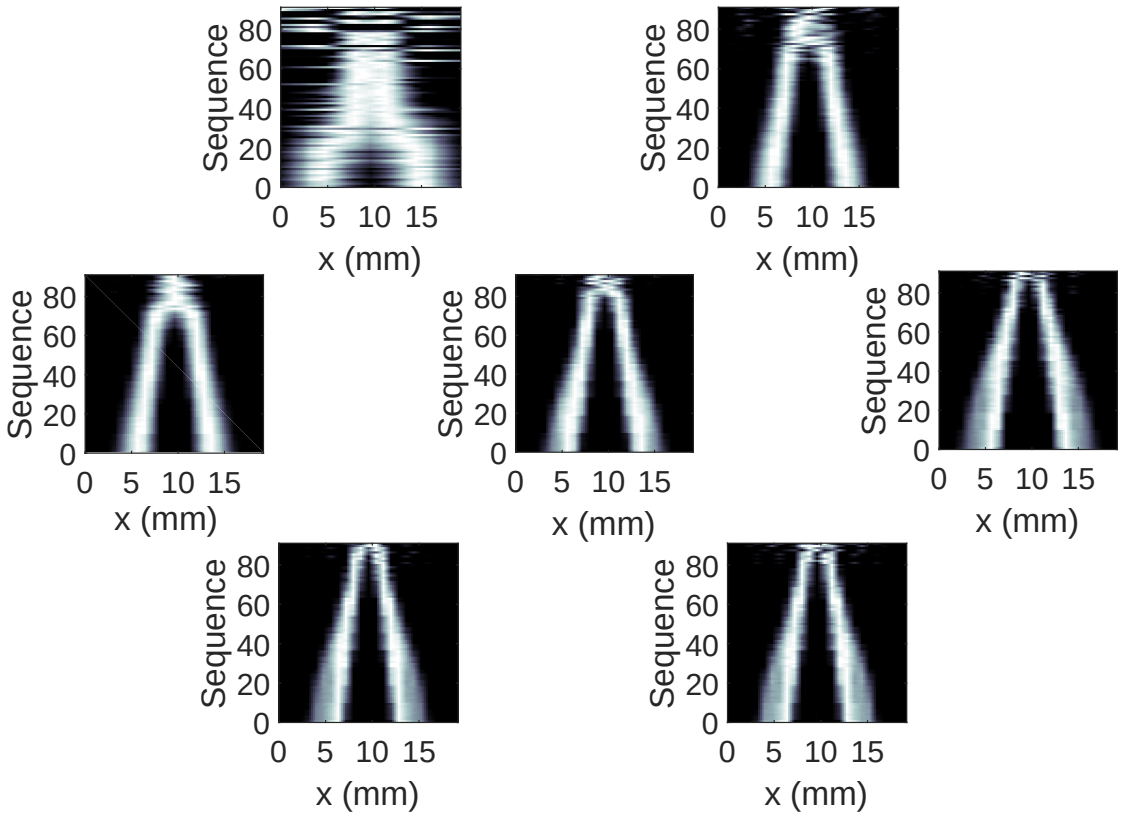

Figure 70: Comparison of the row-wise normalized reconstructed Line Pair Gauge with the FeraSpin series at $W = 1 \cdot 10^{-10}\,\mathrm{Am}^2$. Top row: FeraSpin XS and S; Middle row: FeraSpin M, R, and L; Bottom row: FeraSpin XL and XXL.

6.2.2. Evaluation of phantoms with variable object sizes

In general, the results correspond well with the third harmonic amplitude $|\tilde{m}_3|$ of the tracers with FeraSpin XS having the lowest and FeraSpin L to XXL having the largest $|\tilde{m}_3|$. However, contrary to the standard MPS measurements, the offset field supported MPS also yields quantitative values of the achievable resolution.

So far, the characterizations were performed with a concentration of $c_{\mathrm{Fe}} = 50$ mmol/L and a variable noise level. To generalize these results, Fig. 71 shows the comparison of the predicted resolutions (that were shown to correspond very well with experimental results in the last section) over the ratio between noise level and iron concentration $c_{\mathrm{Fe},i} = 50$ mmol/L.

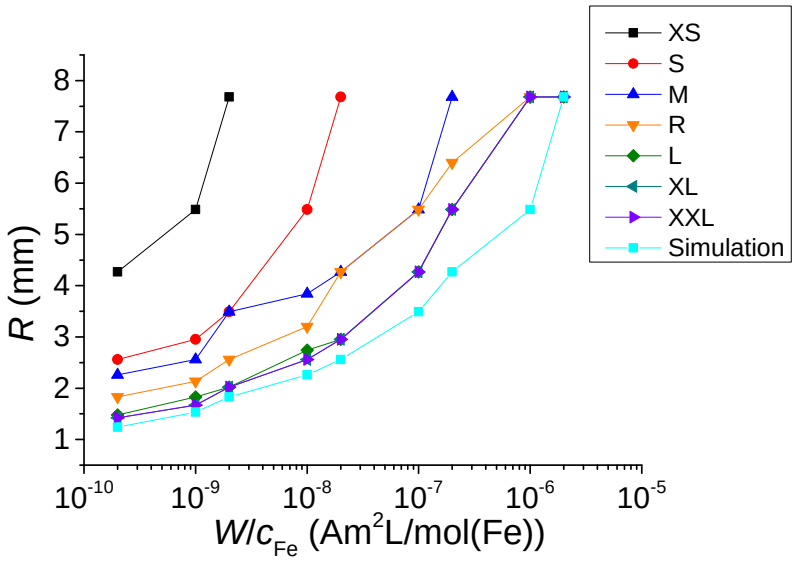

Figure 71: Predicted resolution in dependence on the ratio W/c_{Fe}.

Now, the achievable resolution can be obtained for each respective tracer at $B_{\mathrm{Drive}} = 12$ mT and $G = 1.25\,\mathrm{T/m}$ in dependence on the ratio W/c_{Fe}. From this plot, several ways can be derived to achieve a certain resolution. When a resolution of $R = 3$ mm should be achieved, one way might be to use FeraSpin S and an iron concentration that satisfies $c_{\mathrm{Fe}} \geq W \cdot 1 \cdot 10^9\,\mathrm{mol(Fe)/(Am^2L)}$, which results in a necessary iron concentration of $c_{\mathrm{Fe}} = 100\,\mathrm{mmol/L}$ for a background noise of $W = 1 \cdot 10^{-10}\,\mathrm{Am^2}$. On the other hand, when switching the tracer to FeraSpin XL only $c_{\mathrm{Fe}} \geq W \cdot 5 \cdot 10^7\,\mathrm{mol(Fe)/(Am^2L)}$ would need to be satisfied, reducing the necessary iron concentration for $W = 1 \cdot 10^{-10}\,\mathrm{Am^2}$ to $c_{\mathrm{Fe}} = 5\,\mathrm{mmol/L}$.

Another possibility to generalize the experimental result is depicted in Fig. 72 and 73. Here, the obtained resolutions of a tracer at every tested noise level W_n are normalized to the corresponding achievable resolution of FeraSpin R at the same noise level. Of these relative improvements or deterioration, the mean value $\overline{R/R}_{\mathrm{FeraSpin\ R}}$ was calculated for all tracers, yielding one value describing the mean increase or decrease of the resolution relative to FeraSpin R and independent of the noise:

$$\overline{R/R}_{\mathrm{FeraSpin\ R}} = \frac{1}{n} \sum_n \frac{R(W_n)}{R_{\mathrm{FeraSpin\ R}}(W_n)}. \tag{6.5}$$

.

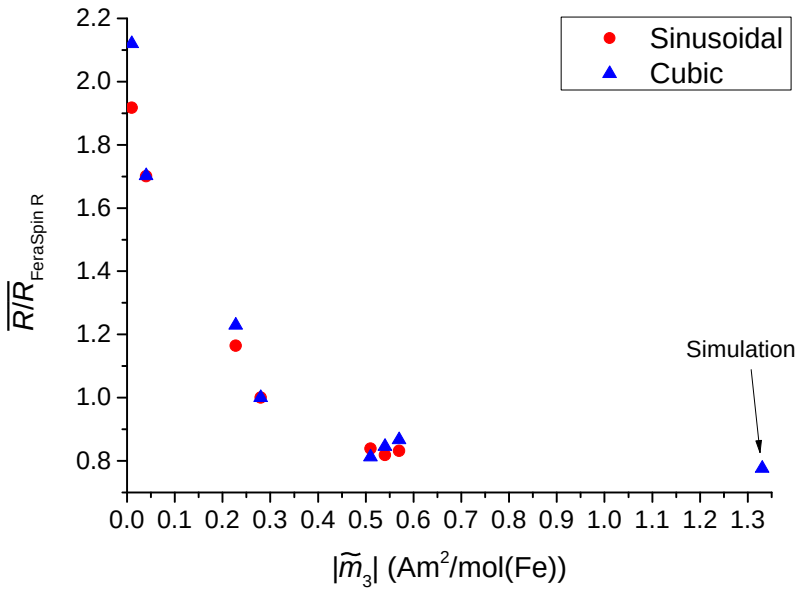

Figure 72: Mean resolution relative to FeraSpin R dependent on the third harmonic amplitude.

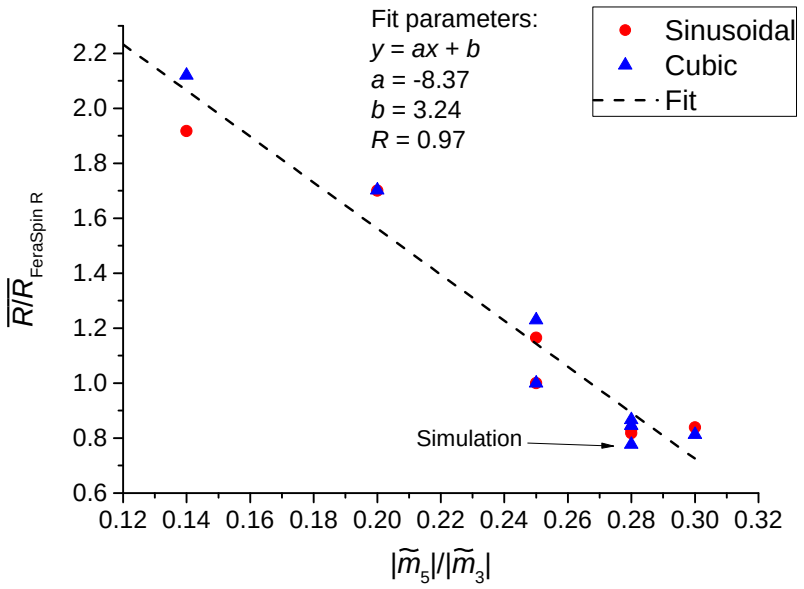

Figure 73: Mean resolution relative to FeraSpin R dependent on the ratio of fifth and third harmonic amplitude.

While no linear relationship could be found between the relative resolution and the $|\tilde{m}_3|$, the relationship between the relative resolution and $|\tilde{m}_5|/|\tilde{m}_3|$ appears to be very linear, at least in the regime of values tested here. Obviously, the relative resolution cannot reach negative values and at some point, a saturation effect will set in. Still, this relationship indicates that a shallow decay of the harmonic spectrum (here represented via the $|\tilde{m}_5|/|\tilde{m}_3|$) is more important for the resolution than just a large $|\tilde{m}_3|$. The reason for this behavior is most likely that tracers with a large $|\tilde{m}_5|/|\tilde{m}_3|$-ratio also exhibit large amplitudes at higher harmonics, which remain usable for reconstruction at higher noise levels. This would not apply to MNP that exhibit a very large $|\tilde{m}_5|/|\tilde{m}_3|$-ratio but a very low $|\tilde{m}_3|$. However, as no such particles have been observed so far, this relationship seems like a valid rough indication for the necessary values of the $|\tilde{m}_5|/|\tilde{m}_3|$-ratio to reach certain improvements in the relative resolution.

In the following chapter, the results of resolution tests with constant object sizes will be presented.

6.2.3. Characterization results for phantoms with constant object sizes

The main difference between this phantom type and the one used in the last section is the constant iron amount in all sequences. Consequently, phantoms with a small gap still have a strong synthetic MPI signal, as the size of the objects does not decrease with the gap in between. Therefore, the sequences of the phantom at a certain noise level are more comparable to each other. This improved comparability is at the expense of characterizing the ability to image small details. Moreover, characterizations at different object sizes a obviously also yield different results. The result for FeraSpin R of this characterization with $a = 3$ mm can be seen in Fig. 74. Further results of this characterization are depicted in Appendix C. The reconstructed resolution R corresponds to the distance between the object centers and the reconstructed gap l_G corresponds to the space in between.

Besides the general trend of the improving resolution from FeraSpin XS to L, XL, and XXL that could already be observed in section 6.2.1, it is conspicuous that for all tracers except FeraSpin XS, the reconstructed resolution remains constant over the course of several different noise levels. This is because for all of these noise levels, the closest objects of the Line Pair Gauge could still be reconstructed with a

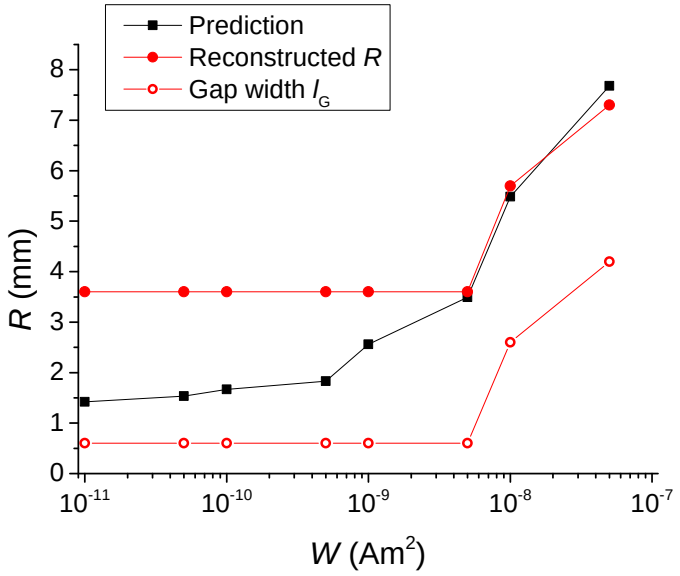

Figure 74: Resolution characterization of FeraSpin R with constant object size of $a = 3$ mm.

visible reduction in contrast in between. At the point where the predicted resolution exceeds the distance between the closest object centers in the Line Pair Gauge, the reconstructed resolution corresponds well with the prediction.

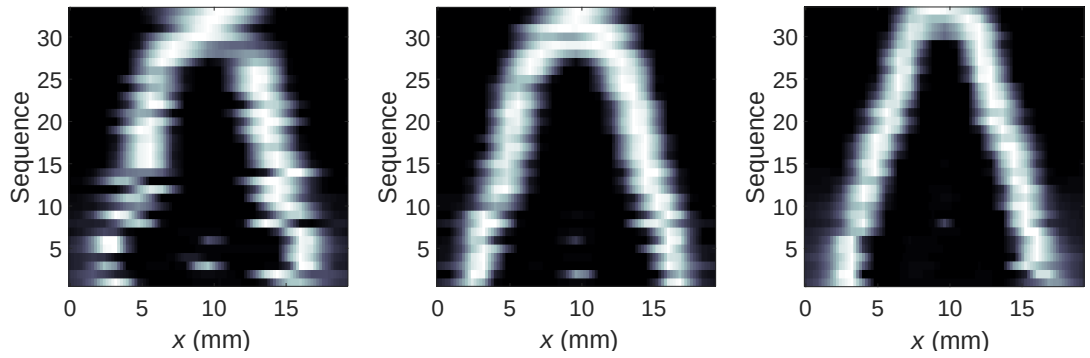

Figure 75: Line Pair Gauge of FeraSpin M (left), R (middle), and L (right) in comparison at $W = 1 \cdot 10^{-8}\,\mathrm{Am}^2$.

Fig. 75 depicts the reconstructed Line Pair Gauge at $W = 1 \cdot 10^{-8}\,\mathrm{Am}^2$ for FeraSpin M, R, and L. It can be seen that it is possible to reconstruct most of the sequences with all three tracers, with FeraSpin L yielding the clearest image with nearly no artifacts. Here, another effect can be observed that so far has been ignored: The signal strength of the harmonics decreases at the edges of the FOV, which can also be observed in the system function of FerasSpin R in Fig. 65. This explains why

the image quality tends to decrease when the objects are close to the edges of the FOV. This is most prominent in the image based on FeraSpin M, which had the lowest harmonic amplitudes in the general MPS characterization of the three tracers depicted here. In the image based on FeraSpin L, which had the highest harmonic amplitudes of the three tracers, the effect is weakest with only slight blurring effects at the edges of the FOV.

6.2.4. Evaluation of phantoms with constant object size

In direct comparison to the phantoms with variable object sizes, it is remarkable that the sequence of the Line Pair Gauge with the closest objects can be reconstructed for a wide range of applied noise levels. The explanation for this observation is visualized in Fig. 76. To reconstruct a tracer distribution and resolve the two

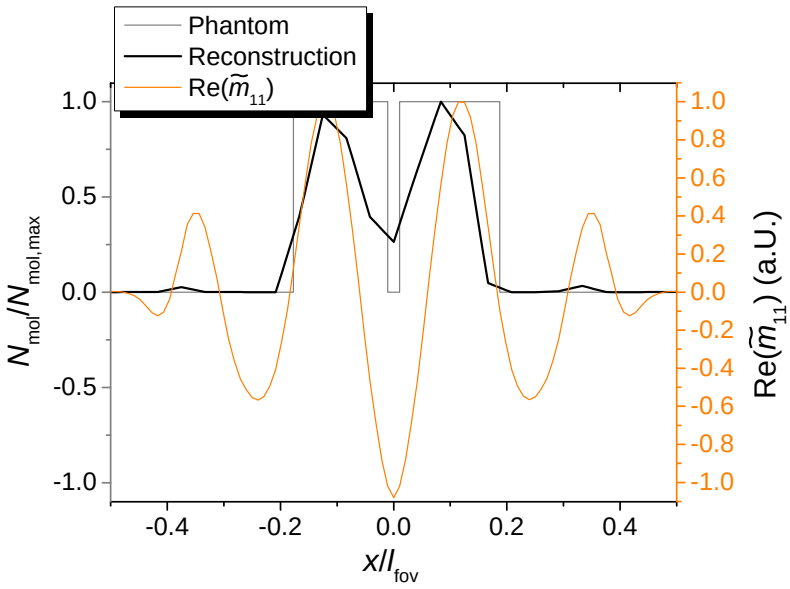

Figure 76: Reconstructed phantom with constant object sizes in comparison to the real part of the highest harmonic employed for reconstruction.

simulated objects from each other, it is necessary to have a spatial frequency that is sufficiently close-meshed. This is the case when two neighboring maxima of a spatial frequency superpose the centers of two objects that are to be reconstructed. In the case outlined here, the highest spatial frequency that just satisfies this criterion was given by the 11th harmonic. In comparison to the phantoms with a variable object diameter and gap width, the distance between the centers is much higher,

which enables the reconstruction with lower harmonics. Apart from the harmonic structure, the resolution of small gaps is also limited by the widening effect of the PSF as well as by the voxel size. Here, the reconstructed gap was even smaller than the voxel size. As a result, it is easily visible but appears to be much wider than it actually is.

Apart from this behavior, the results are similar to the ones of section 6.2.1 with FeraSpin L to XXL being able to tolerate the full tested range of noise levels up to $W = 1 \cdot 10^{-7}\,\mathrm{Am}^2$, where they reach a distance between the object centers of approximately 7.7 mm.

After the characterization of the FeraSpin series employing two different phantom types, in the following sections, potential (advanced) applications for the offset field supported MPS characterization will be introduced.

6.2.5. Advanced 1D characterizations

To this point, the focus of the imaging characterization has been on the influence of the SNR on the resolution. Another possible application for the offset field supported MPS, that shall briefly be introduced here, is the investigation of the influence of MPI signals that do not ideally correspond to the system function. For the characterizations performed in the previous sections, the MPI signals and the reconstruction matrix were based on the same particle suspension, differing only in the offset increment B_{incr}. However, should the tracers differ in their present state from the reference suspension, for example due to immobilization or precipitation, the image quality would supposedly be influenced. As examples for advanced applications of this method, the influence of different immobilized or precipitated tracers on the image quality will be presented in this section. As this is only a brief introduction into the possibilities of advanced applications with this method, the results obtained here will be kept short.

6.2.5.1. Immobilized particles So far, the signal generation system matrix $\mathbf{A}_1$ and the reconstruction system matrix $\mathbf{A}_2$ were obtained from the same sample, a particle suspension in deionized water. Here, $\mathbf{A}_1$ consists of spectra obtained from the offset field supported MPS measurement of particles that were immobilized by freeze-drying, whereas $\mathbf{A}_2$ consists of the spectra obtained from the standard particle

suspension. While it has been shown in Chapter 5 that MNP with the strongest signal align their magnetic moment via Néel, currently many of the best performing tracers still have a notable amount of particles with Brownian rotation due to the broad distribution of particle sizes, which is inhibited by the freeze-drying.

The Line Pair Gauge with square objects and variable object diameters was used as a phantom. The parameters l_{fov}, f, B_{Drive} and G were equivalent to the regular resolution characterization. To suppress any potential influence of the noise, the reconstruction was performed without additional Gaussian noise and only by including the first 10 or 15 harmonics, respectively, in the reconstruction. This was done for FeraSpin S, R, and XXL as examples of different Brownian contributions to the particle rotation. In Fig. 30 and Tab. 1, it was shown that the spectrum of freeze-dried FeraSpin S remains nearly unchanged whereas the spectrum of freeze-dried FeraSpin R and XXL show stronger deviations from the spectrum of the suspension due to the larger particles and therefore stronger influence of Brownian rotation.

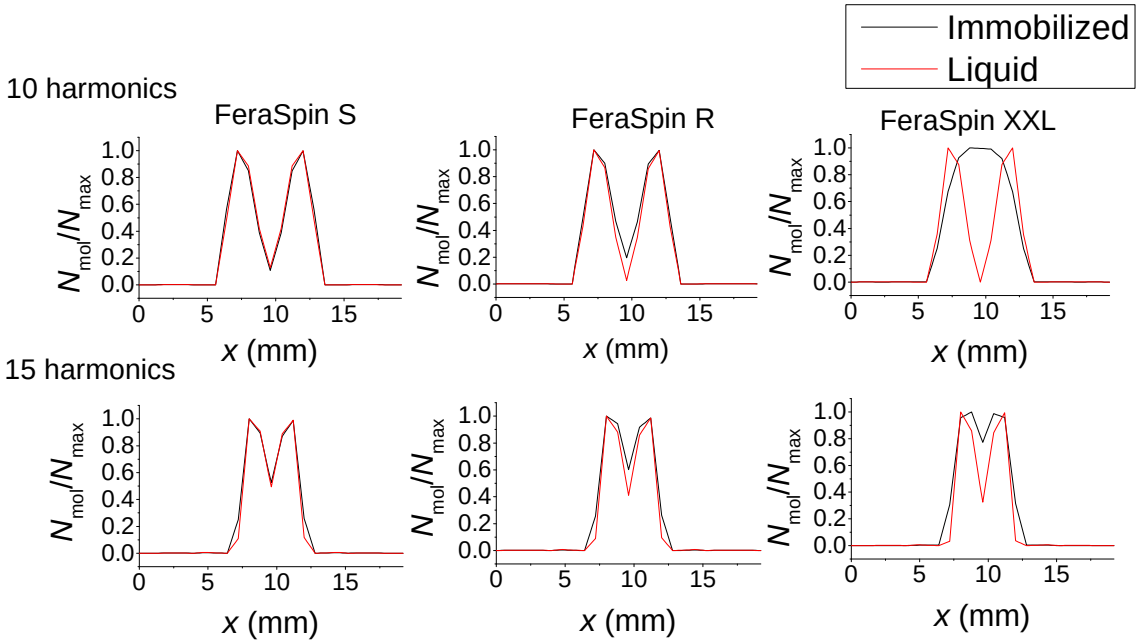

Figure 77: Influence of the mobility of MPI tracers on the resolution. The achievable resolution decreases dependent on the fraction of Brownian particles.

This consequently results in the reconstructions depicted in Fig. 77. Here, reconstructions with 10 and 15 harmonics are presented. For FeraSpin S, nearly no influence can be observed. This was expected since those particles have very small core sizes (see Fig. 27) and therefore primarily rotate via Néel. Accordingly, only

very small changes were observed in comparison between suspension and immobilization. This effect becomes stronger with FeraSpin R, where the two objects can still be separated from each other, but with a clearly weaker contrast. FeraSpin XXL, which had the largest fraction of Brownian particles, reveals the strongest influence of the immobilization. Here, it is not possible to resolve the two objects from each other when using 10 harmonics and only with a very weak contrast for 15 harmonics.

How precipitation of tracers can influence the image quality will be presented in the next section.

6.2.5.2. Precipitated particles MNP begin to precipitate when the salt concentration in the suspension is high enough to remove the repulsion barrier between the particles, which may lead to irreversible coagulation (see [78] for further details on that topic).

To investigate the influence of precipitated particles, the system functions $\mathbf{A}_1$ and $\mathbf{A}_2$ were measured employing MPS with additional offset fields. While the MPI signal generation system matrix $\mathbf{A}_1$ was based on the measured spectra of precipitated particles, the reconstruction system matrix $\mathbf{A}_2$ was based on the standard tracers in a deionized suspension.

Here, Sodium Chloride (NaCl) was used to cause precipitation of FeraSpin R. The NaCl concentration in the human blood of healthy adults is $136-145$ mmol/L [104]. To ensure precipitation, an NaCl concentration of $c_{\mathrm{NaCl}} = 250$ mmol/L was used. The effect on the MPS spectrum can be seen in Fig. 78 and corresponds with the effects of attenuation and amplification of certain harmonics observed in differently concentrated particle suspensions [83]. It can be seen that up to the 9th harmonic, the harmonic decay steepens, while beginning with the 11th harmonic, the decay becomes highly nonlinear with a wavelike form. Since only one tracer type was analyzed, the comparability between the sequences of the Line Pair Gauge was important. Therefore, a constant object size of $a = 3$ mm was presumed.

In Fig. 79, the entire reconstructed Line Pair Gauge is plotted for four different cases: In the horizontal direction, $\mathbf{A}_1$ is varied between FeraSpin R in a deionized suspension and FeraSpin R with NaCl. In the vertical direction, the reconstruction is varied between 10 and 20 harmonics.

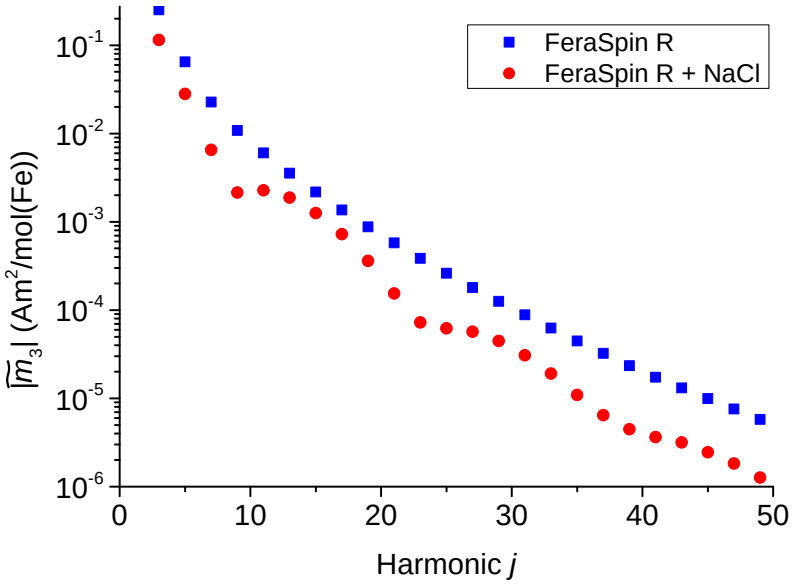

Figure 78: MPS spectra of FeraSpin R and FeraSpin R + NaCl of $c_{\mathrm{NaCl}} = 250$ mmol/L.

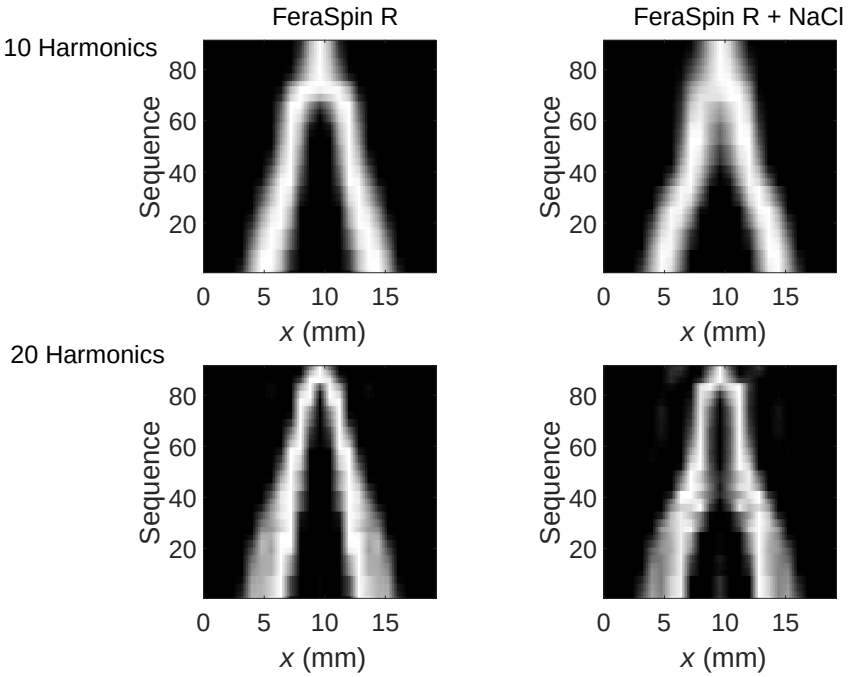

Figure 79: Influence of NaCl on the image quality of FeraSpin R. Left: Regular reconstruction of all sequences of the Line Pair Gauge with FeraSpin R. Right: Reconstruction when $\mathbf{A}_1$ is based on FeraSpin R with NaCl concentration $c_{\mathrm{NaCl}} = 250$ mmol/L.

It is evident that the effects observed here differ depending on the number of harmonics used in the reconstruction. When 10 harmonics were used, a blurring effect could be observed, effectively leading to a decreasing resolution. When 20 harmonics were used, this effect is much less pronounced. Instead, emerging artifacts can be observed.

6.2.5.3. Evaluation It was presented here how the offset field supported MPS characterization may also be used to investigate the influence of changes in the particle behavior on the image quality. This was done via immobilized as well as precipitated particles. It could be observed in both cases that the image quality may be influenced drastically via decreasing resolution and contrast as well as by artifacts in the reconstruction.

This method may therefore also be a valuable tool to investigate the influence of signal altering effects in MPI, as in [73], or even investigate advanced MPI methods like mobility MPI [137] or multi-color MPI [135], when no suitable scanner is available.

6.3. 2D tracer characterization

To this point, the characterization procedure was done in 1D due to the limitation of the MPS setup, consisting only of one excitation and receive coil. The approach therefore lacked the mixed frequencies occurring in multidimensional MPI as described in section 2.3.1.5. To overcome this limitation, the characterization was also performed with measurement data of FeraSpin R obtained with a 2D MPS, built at the Institute of Medical Engineering, Universität zu Lübeck [47]. This MPS consists of two perpendicular excitation and receive coils and was operated at two frequencies $f_\mathrm{x} = 25.25$ kHz and $f_\mathrm{y} = 26.04$ kHz with drive field strengths $B_{\mathrm{Drive}x,y} = 12$ mT. By sweeping through the offset fields in x- and y- directions between 0 mT and 12 mT with an increment of $B_\mathrm{incr} = 0.25$ mT, a total of 49 x 49 spectra were measured (Fig. 80). To obtain the spectra for all four quadrants, the measured spectra of the system function were mirrored according to [139], yielding a total of $97 \times 97 = 9409$ spectra. The same procedure was applied to obtain the reconstruction system function with $B_\mathrm{incr} = 1.00$ mT, yielding 25×25 voxels after mirroring.

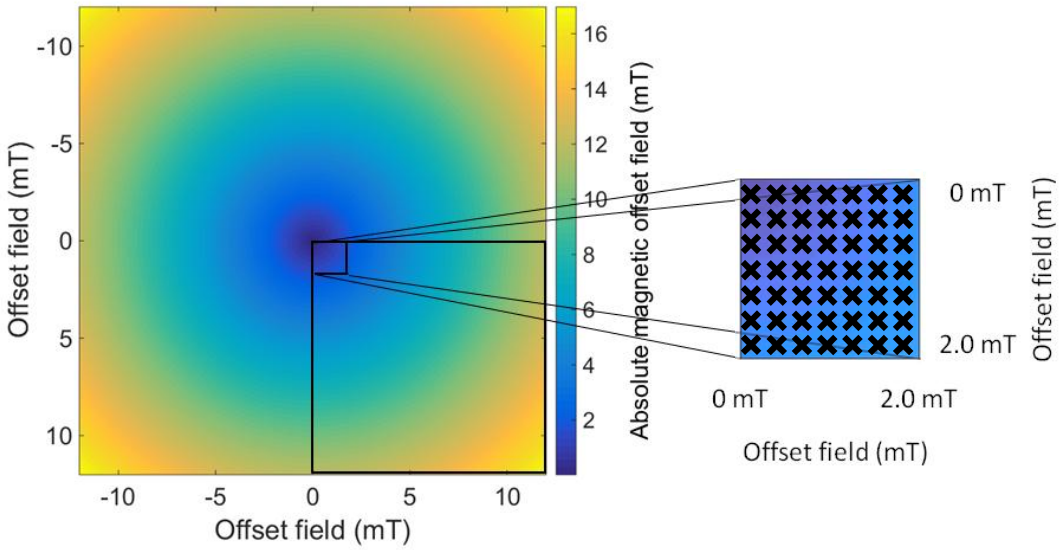

Figure 80: Division of the offset field in 0.25 mT increments. Large image: The frame depicts the measured quadrant with offset fields between 0 mT and 12 mT in x- and y-direction. Small image: Magnification of the measurement grid. Each cross represents an offset field combination where an MPS spectrum was obtained.

Fig. 81 shows the relationship between the measured spectra for three exemplary offset combinations (left) and frequency components (right) mapped over the offset fields. The harmonic amplitudes at a certain frequency of all offset combinations can be combined to one characteristic image of the frequency component. Here, the relationship is visualized for the frequencies marked 1, 2, and 3 at the field offsets a, b, and c.

Before a characterization using the 2D MPS can be performed, the zero offset MPS spectra of both devices should be compared to evaluate, if the spectra change when the tracers are excited by two instead of one drive field. Since it was shown that the ability to resolve small details in the FOV depends on the availability of suitable spatial frequencies, a change in the harmonic amplitude of higher harmonics would

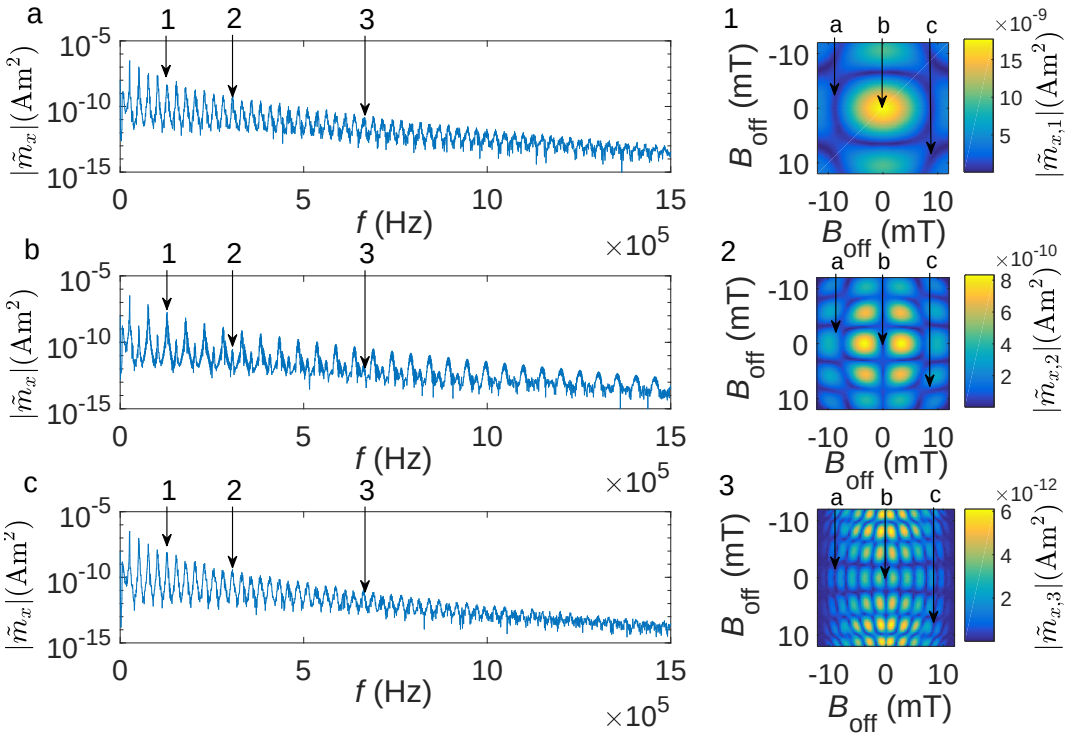

Figure 81: Principle of MPS employing two excitation and receive coils. Left: Spectra of the x-axis receive coil at x-y-offset combinations $B_{\mathrm{off,a}} = [-6, -2]$ mT, $B_{\mathrm{off,b}} = [0, 0]$ mT and $B_{\mathrm{off,c}} = [8, 8]$ mT; Right: Exemplary frequency components of all offset combinations for $B_{\mathrm{off},x,y} = [-12, ..., +12]$ mT, obtained with the x-axis receive coil. The three frequency components correspond to the marked frequencies 1, 2, and 3 on the left.

also influence the achievable resolution.

This comparison is depicted in Fig. 82. The harmonic spectrum of the 2D MPS with two-coil excitation exhibits a steeper decay than the single-coil excitation MPS. This might be due to differences in the calibration of the device, but might also be caused by the influence of the 2D excitation that effectively distributes the particle energy on more frequencies. This decay of higher harmonics will most likely result in decreased resolutions compared to the 1D case.

In Fig. 83, the software phantom for the 2D experiments is depicted. It corresponds to the 1D experiments with an edge length a of each phantom block that is equivalent to the gap between the blocks. In 1D, only distinct spectra in y-direction were available and the virtual phantom extent in x- and z-direction was achieved by

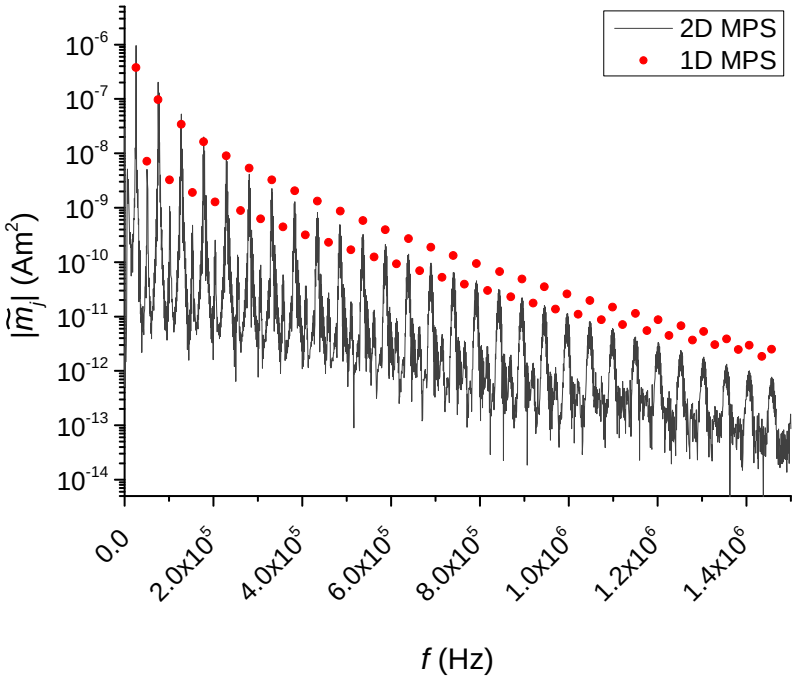

Figure 82: Comparison of FeraSpin R measurement employing a standard and a 2D MPS.

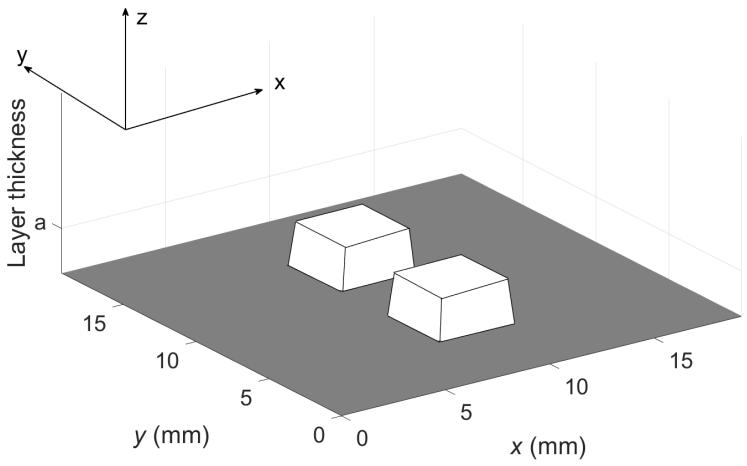

Figure 83: Phantom for the 2D resolution estimation.

scaling the corresponding y-spectrum according to the virtual volume. In 2D, there are distinct spectra in x- and y-direction and only the virtual extent of the phantom in z-direction is achieved via scaling the corresponding (x,y)-spectrum.

The experiments were performed with an assumed gradient strength of $G_{x,y} = 1.25$ T/m and therefore with a FOV $l_{\mathrm{fov},x,y} = 19.2$ mm. The phantom edge length (as well as the gap) was defined as $a_1 = 2.4$ mm, $a_2 = 3.2$ mm, and $a_3 = 4.0$ mm. The signal generation was equivalent to the 1D experiments, only with $I = 97^2 = 9409$ instead of $I = 97$ spectra. The artificial MPI signal was generated according to (6.2) and the noise level W was raised until the resolution limit of each phantom was reached. At the noise level, where the two blocks were barely resolvable, the frequency components that were included in the reconstruction process were analyzed for the highest spatial frequency. In contrast to the 1D experiments, now not only pure harmonics j, but also the mixed frequencies (see (2.44)) were taken into account. Therefore, the spatial frequency as well as the resolution were not derived from the harmonic number j, but from the highest number of spatial periods $\tilde{f}_{\max}$ of all frequency components included in the reconstruction:

$$R = \frac{l_{\mathrm{fov}}}{\tilde{f}_{\max}} = \frac{1}{f_{\mathrm{spatial,max}}}. \tag{6.6}$$

This was compared to the actual distance between particle blocks.

The result can be seen in Fig. 84. Here, the phantoms (left), the reconstruction at the highest tolerated noise level (middle), and the spatially resolved frequency component with the highest spatial frequencies at this noise level (right) are depicted. In contrast to the resolution estimation in 1D, each frequency component enables a certain resolution in x- and y-direction, depending on the number of extrema in each direction. In the case of the phantoms evaluated here, the spatial frequency in y-direction is therefore the one that determines the resolution. For example, the predicted resolution of the 2.4 mm phantom can be calculated via $R = 19.2/3.5 = 5.5$ mm, since the seven white dots indicate seven extrema and therefore 3.5 spatial periods.

The results for the three phantom sizes are summarized in Tab. 4. It seems that the prediction based on the spatial frequency slightly underestimates the actual achievable resolution with deviations between 6% and 17%. This is less accurate than it was observed in the 1D characterization, but still in good agreement with the predictions based on the frequency components.

It is conspicuous that the achievable resolution is decreased in comparison to the 1D characterization. This was expected due to the steeper harmonic decay that

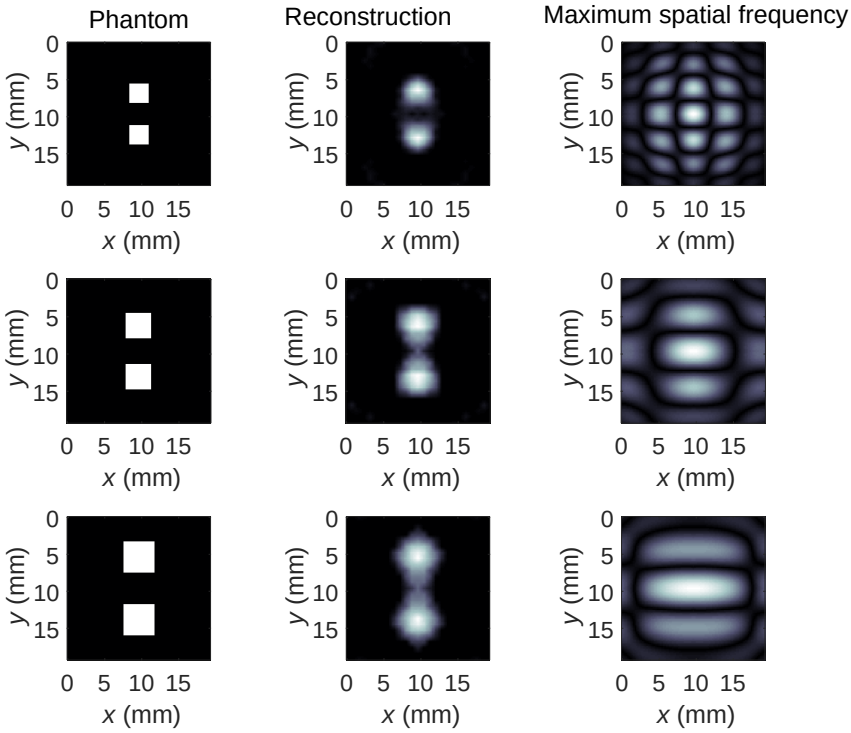

Figure 84: Reconstructed phantoms and the frequency component with the highest spatial frequency. Left: Cubic phantom of the sizes 2.4 mm, 3.2 mm, and 4.0 mm; Middle: Reconstructed image at highest tolerated noise level; Right: Absolute values of the spatially resolved amplitude of the frequency component with highest spatial frequency in a vertical direction.

was observed at 2D excitation in comparison with the 1D excitation. Whether this phenomenon is based on the spectrometer calibration or on particle physics is yet to be investigated.

In the following section, the results obtained so far will be compared to actual MPI phantom experiments.

Center distance	Prediction	Tolerated noise level
4.8 mm	5.5 mm	$3 \cdot 10^{-10}\,\mathrm{Am}^2$
6.4 mm	7.7 mm	$1 \cdot 10^{-9}\,\mathrm{Am}^2$
8.0 mm	8.5 mm	$6 \cdot 10^{-9}\,\mathrm{Am}^2$

Table 4: Distance between square phantom centers and resolution prediction based on the highest spatial frequency

6.4. MPI phantom experiments

In the last sections, the resolution estimation of the FeraSpin series was performed with an MPS employing single-coil excitation as well as with a 2D MPS with x- and y-directional excitation. Here, the results of MPI phantom experiments will be presented and compared with the 1D experiments. Moreover, challenges of the resolution characterization in MPI and their comparison to the results obtained here will be discussed.

6.4.1. Phantom preparation

The MPI phantom experiments were all performed with the tracer FeraSpin R, which was also employed for the 1D and 2D characterization. To cover a broad range of different iron contents, the experiments were performed with diameters of $a = [2, 3, 4, 5]$ cm and iron concentrations of $c_{\mathrm{Fe}} = [1, 10, 25, 50]$ mmol/L. The phantoms were made of acrylic glass with cylindrical bores, as cubic bores were not feasible. In contrast to the offset MPS experiments, where the simulated objects were cubic, the volume of the MPI phantoms are thus not $V = a^3$ but $V = \frac{\pi}{4} d^2 h = 0.79 a^3$ with $d = h = a$. All phantoms were sealed with oil to prevent evaporation of the suspension medium.

6.4.2. Phantom experiment results

The phantom experiments were performed at the Universitätsklinikum Eppendorf (Hamburg) with a commercial preclinical MPI scanner (Bruker/Philips). The image acquisition was performed with a drive field $B_{\mathrm{Drive},x,y,z} = 14$ mT and gradient fields $G_{x,y} = 0.75$ T/m and $G_z = 1.5$ T/m.

Fig. 85 shows the results of the phantom experiments in the x-y plane. Every image depicts a combination of phantom diameter and concentration. It can be seen that the phantoms with $c_{\mathrm{Fe}} = 1$ mmol/L are all nearly indistinguishable from the background noise, whereas all phantoms with $c_{\mathrm{Fe}} = 50$ mmol/L showed a very clear image, only with the smallest 2 mm phantom slowly beginning to become blurred. A combination that strongly suggests being close to the resolution limit is the phantom with $a = 2$ mm (and distance between the objects) and $c_{\mathrm{Fe}} = 25$ mmol/L. It can further be observed that the combination of $a = 2$ mm and $c_{\mathrm{Fe}} =$

10 mmol/L is below the resolution limit whereas $a = 3$ mm and $c_{\mathrm{Fe}} = 10$ mmol/L still allows a clear distinction of the two objects. The resolution limit for $c_{\mathrm{Fe}} = 10$ mmol/L is therefore suspected to be located somewhere between 4 mm and 6 mm distance between object centers. For larger objects, the resolution limit seems to be between concentrations of $c_{\mathrm{Fe}} = 1$ and $c_{\mathrm{Fe}} = 10$ mmol/L.

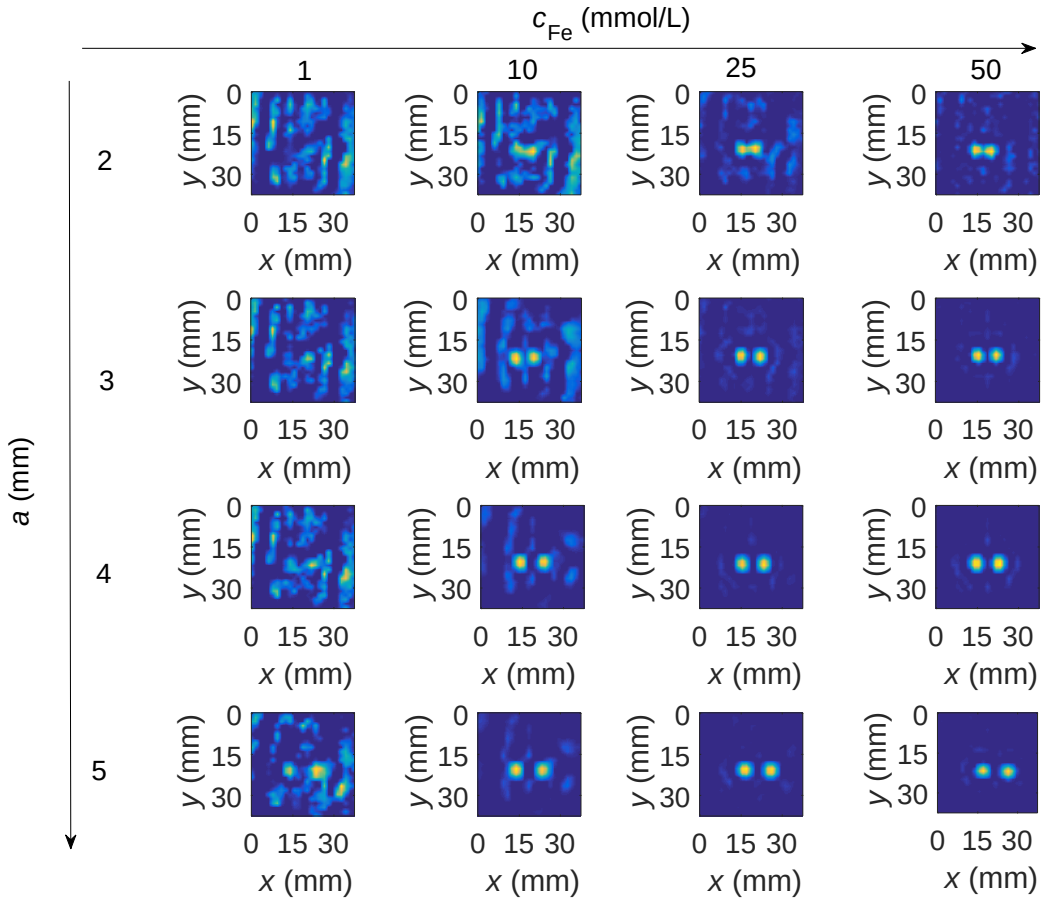

Figure 85: MPI phantom experiment results. The images are sorted by phantom diameter and concentration.

The following comparison between offset MPS and MPI phantoms will therefore focus on the 2 mm / 25 mmol/L phantom as well as the resolution limit for an iron concentration of $c_{\mathrm{Fe}} = 10$ mmol/L.

6.4.3. Comparison of offset MPS and MPI

To compare the offset field supported MPS characterization with the MPI phantom experiment at $B_{\mathrm{Drive}} = 14$ mT, a new 1D system function of FeraSpin R was

measured with MPS in an offset field. Furthermore, the volume of the virtual cubic phantom with an iron amount corresponding to the bore volume was calculated, since projecting a cylinder on a 1D phantom did not seem feasible. The cylindrical phantom with a diameter and height of $a = 2$ mm has a volume of $V = 6.28$ µL, which corresponds to a cube with an edge length of $a = 1.84$ mm.

An essential challenge in the validation of the offset MPS method is the noise level W present in an MPI scanner. As the scanner used for the experiments does not yield the measured magnetic moment but only a signal in arbitrary units, other ways have to be found to establish a comparable noise level to apply on the offset MPS characterization. An indicator to estimate the noise level is the detectability of a tracer sample in the FOV. In earlier experiments with the scanner, it was determined that a Resovist sample (that magnetically behaves like FeraSpin R [37]) with a volume $V = 20$ µL and an iron concentration $c_{\mathrm{Fe}} = 1$ mmol/L was not detectable whereas a sample of the same volume and $c_{\mathrm{Fe}} = 2$ mmol/L could still be localized. Based on these findings, the noise level at the detection limit for said parameters was investigated with the MPS setup. A first rough approximation based on a zero offset MPS measurement can be made using the third harmonic amplitude $|\tilde{m}_3|$. A tracer volume $V = 30$ µL and concentration $c_{\mathrm{Fe}} = 50$ mmol/L yields a third harmonic amplitude $|\tilde{m}_3| = 4.55 \cdot 10^{-7}\,\mathrm{Am}^2$ at $B_{\mathrm{Drive}} = 14$ mT. Assuming perfectly linear scalability, the third harmonic of $V = 20$ µL and $c_{\mathrm{Fe}} = [1, 2]$ mmol/L can be calculated to $|\tilde{m}_3| = 6.07 \cdot 10^{-9}\,\mathrm{Am}^2$ and $|\tilde{m}_3| = 1.21 \cdot 10^{-8}\,\mathrm{Am}^2$, respectively. It was therefore assumed, that the noise level is located somewhere in this area. To find an estimation for the noise level in the MPI scanner, the sample localization described for MPI was repeated with a software phantom and spectra measured with the MPS setup. The tracer volume was placed in the center of the virtual FOV and the artificial MPI signal was constructed. After addition of gaussian background noise, the particle distribution was reconstructed. This procedure was repeated ten times per noise level and for each noise level, the correlation coefficients between input distribution and reconstruction were calculated from the ten reconstructions. The results are visualized in Fig. 86 via the mean values and standard deviations of the 10 correlation coefficients per noise level. It can be seen that the resolution limit can be clearly attributed to $W = 1 \cdot 10^{-9}\,\mathrm{Am}^2$, which was therefore applied for the experiment.

With the noise level being set to $W = 1 \cdot 10^{-9}\,\mathrm{Am}^2$, the comparison between MPI and offset field supported MPS was performed. This was done with a threshold

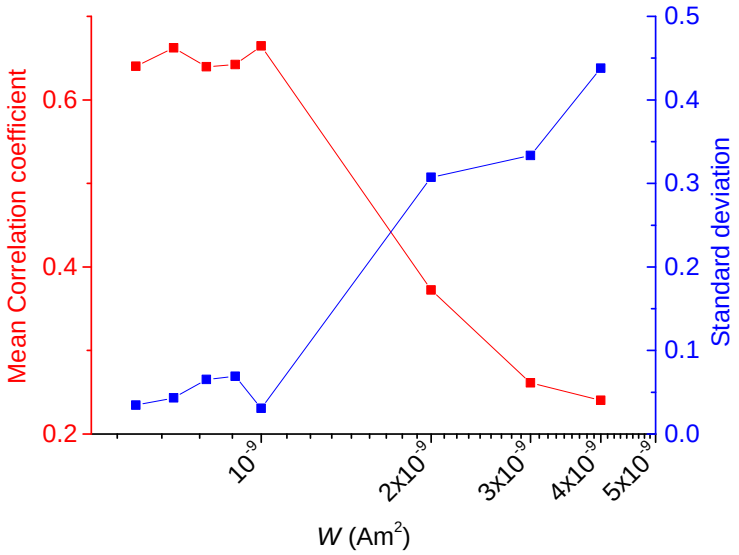

Figure 86: Mean correlation and standard deviation of 10 reconstructions per noise level when localizing a central particle volume with $c_{\mathrm{Fe}} = 2$ mmol/L and $V = 20$ µL.

ratio between maximum nominal iron amount and mean reconstructed iron amount at the edges of the FOV $\vartheta > 10$ and the Line Pair Gauge sequence with decreasing object sizes. The latter prevents the exact reproduction of the combination of iron amount N_{P} and gap length l_{G} since the cylindrical volume corresponds to a cube with $a = 1.84$ mm and the bore had a gap length $l_{\mathrm{G}} = 2$ mm. On the other hand did this ensure particle distributions where the l_{G} always corresponds to the object diameter.

Simulating a particle concentration of $c_{\mathrm{Fe}} = 25$ mmol/L, the resulting reconstructions around the resolution limit are depicted in Fig. 87. The distributions are sorted from top to bottom from largest to smallest gap or highest to lowest iron content. Moreover, the ratios between iron content of the software phantom and the MPI phantom $N_{\mathrm{MPS}}/N_{\mathrm{MPI}}$ are depicted. It can be seen that the two top particle distributions can still be reconstructed, while the three distributions at the bottom have a gap and an iron content that does not allow a distinction between the two objects in the reconstruction.

The closest objects that were still resolvable have a distance of $l_{\mathrm{G}} = 1.94$ mm and 92% of the iron content that was present in the MPI experiment. It can also be seen that an iron content that is only slightly lower already inhibits the reconstruction of both objects.

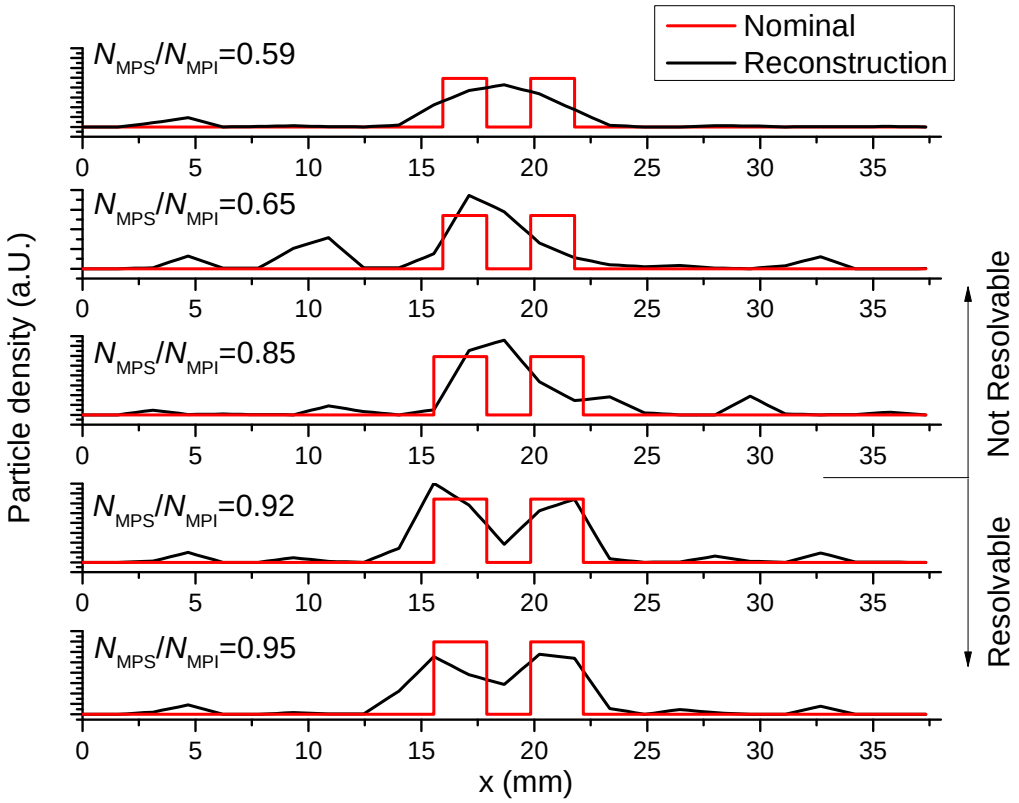

Figure 87: Reconstructed 1D particle distributions around the resolution limit. The objects in the top two distributions are resolvable, the bottom three distributions are not resolvable. The closest objects that were still resolvable have a distance of 1.94 mm and 92% of the iron content present in the MPI experiment.

A second $[l_G, c_{Fe}]$ combination that was noteworthy is the [3 mm, 10 mmol/L] combination, that was the closest tested distance to be resolvable at this concentration. A resolution limit would therefore be expected between 4 mm and 6 mm center distance.

To that end, the offset field supported MPS was employed to simulate the resolution dependent on the noise with the field parameters of this study and $c_{Fe} = 10$ mmol/L as it was done in sections 6.2.1 and 6.2.3. The results of this simulation as shown in Fig. 88 indicate that the resolution limit at $W = 1 \cdot 10^{-9}\,\mathrm{Am}^2$ was made out to be 5.83 mm between the phantom centers and thus, lies in the regime in which it was expected due to the phantom experiments. In conclusion, the resolution limits that were found in this MPI phantom study could be reproduced in an MPS setup for an approximated noise level of the MPI setup.

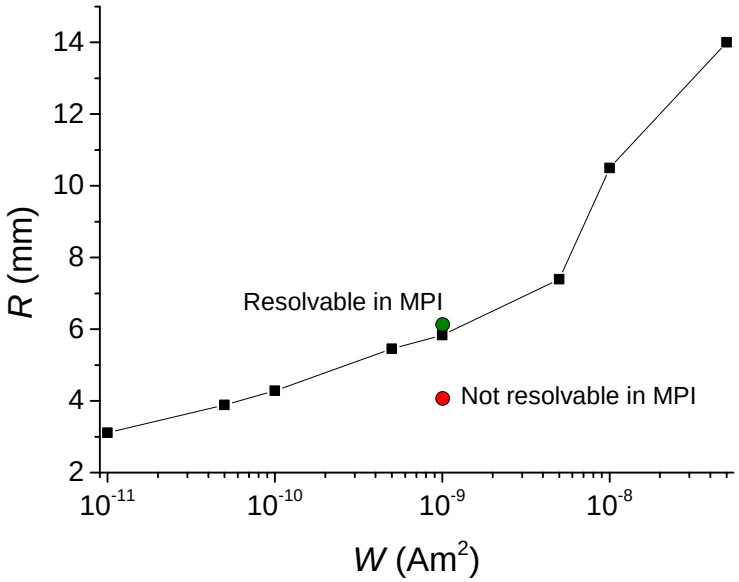

Figure 88: Achievable resolution dependent on noise level as acquired by offset field supported MPS in comparison to MPI phantom experiments.

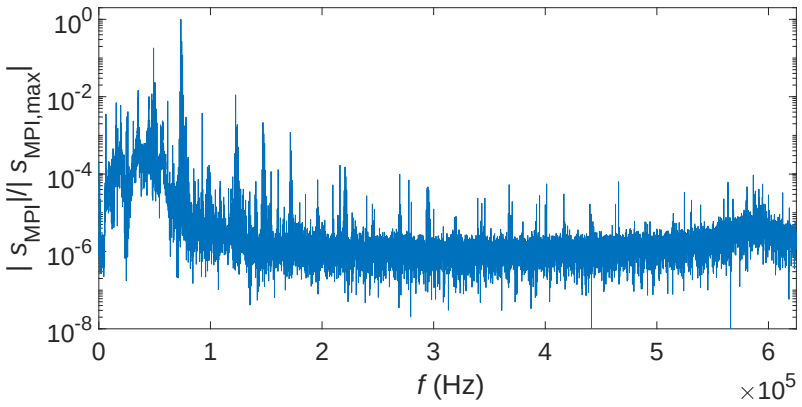

Figure 89: Empty signal of an MPI scanner.

An issue that has not been addressed yet is the noise level over the frequency range of the bandwidth. In the simulations performed here, the noise level was assumed to be constant over the whole spectrum. This needs to be treated as a rough approximation as can be seen in Fig. 89. This nonlinear shape shows that unlike in the simulation of this thesis, different frequency components are affected by different noise levels.

Two aspects are conspicuous here and might be a topic of further research. First, there are very distinct spurious signals around the pure harmonics. Second, the noise

level itself is not constant but has maxima at 50 kHz and 600 kHz. Given this behavior, further developments of a resolution prediction based on simulations should include this behavior of the background signal. Still, this requires the investigation of the sources of these interferences first.

6.5. Discussion of the offset field supported MPS characterization

With the offset field supported MPS characterization of MNP as tracers for MPI, a new method was developed to access relevant imaging parameters, such as the resolution without an otherwise necessary MPI scanner.

The proposed method includes the usage of measurement based software phantoms to obtain general expressions for the respective resolution dependent on the noise level. In a characterization of several tracers, the proposed theory of a resolution that depends on the available spatial frequencies and thus the available harmonics (see Chapter 4) could be confirmed and a generalized expression was found describing the resolution over a ratio between the noise level and the concentration W/c_{Fe}. Based on these results, the mean resolution relative to Feraspin R was found to improve linearly over the ratio between the fifth and third harmonic amplitude.

The same procedure was repeated for fixed object sizes that were moved towards each other until the gap between the objects closed. In contrast to the first experiment, where the object sizes decreased according to the gap width, it could be seen that imaging both objects with only a small gap in between was possible over a wider range of noise levels. This was attributed to the fact that the distance between the centers of the objects was still comparably large even though the gap in between was only very small. Therefore, the reconstruction of these particle distributions was also possible with lower spatial frequencies.

This method was also applied on virtual MPI signals based on immobilized and precipitated particles to introduce the possibility to test the influence of non-ideal system functions or changes in the particle state on the image. It is suggested that it might also be suited to investigate new MPI related applications like multi-color MPI or mobility MPI.

In the current approach, a single measurement takes 45 minutes and enables the generation of every possible 1D phantom. With a more elaborate setup, including an automatized sweep of the offset fields using coils, this time could be reduced drastically. In comparison with this, an MPI measurement is far more time consuming due to the long system function acquisition, which still does not include the actual phantom measurements.

In a comparison with actual MPI phantom experiments, a general agreement between simulations and experiments was found with the simulations being able to predict a distance-concentration combination directly at the resolution limit correctly. Moreover, it was possible to simulate the resolution limit of a certain iron concentration in accordance to the phantom experiments. It is therefore concluded that the offset field supported MPS characterization is indeed able to correctly predict the MPI resolution, regardless of the missing mixed frequencies in the 1D setup. In an MPS comparison between single-coil excitation and double-coil excitation, difference in the steepness of the harmonic decay was still observed. It is not clear yet whether these deviations occur from differences in the calibration or if there are other reasons for this behavior.

Even though the results have been very promising and implications from the offset field supported MPS could be confirmed with MPI experiments, the method still has to face some challenges. First, the relationship between spectral amplitudes of single- and multiple-coil excitation and the influence of the generation of mixed frequencies on the amplitude of pure harmonics still needs further investigation. Second, it will still be necessary to better understand the nonlinear background noise and interference signals (as it was already begun by Schmale et al. [115]). Last, the MPI trajectory on the resolution has not been taken into account, which has been shown to have an influence on the particle behavior and hence, the MPI signal [48]. All these challenges will need to be addressed on several fronts from tracer characterization and simulation to signal analysis at the MPI scanner to understand how and why MPI signals and reconstructed images look the way they do. This method is a contribution to this joint effort by showing the comparability of 1D and 3D sequences as well as the predictability of the achievable resolution dependent on the noise level and therefore: the SNR.

7. Conclusion

The focus of this thesis is the relationship between the essential structural parameters of MNP and the MPS spectrum, as well as between the MPS spectrum and the achievable spatial resolution in MPI.

To that end, a general relationship between spatial frequencies and harmonics of the MPI signal is presented. Moreover, it is explained how the reduction of the available harmonics due to noise contamination influences the resolution. It was concluded that the achievable resolution in the image is not only influenced by the width of the PSF or a limiting contrast loss in the MTF, but also by the concentration, noise level, and the iron amount; in short: the SNR.

To find a set of structural MNP parameters that maximize the SNR in MPI, a simulation environment was developed that employs the effective field method, which was originally developed to describe the dynamic magnetic moment in a low field environment. To also be able to describe the magnetic moment at field strengths applied in MPS and MPI, phenomenological descriptions of the field dependent Brownian and Néel rotational dynamics from literature were included in the simulation. With this tool, a large parameter study was performed to find the most suitable magnetic core sizes for given combinations of effective anisotropy constants and hydrodynamic shell thicknesses. Based on these insights, the highest possible third harmonic amplitude and ratio between fifth and third harmonic were found for log-normally distributed particle suspensions with realistic combinations of structural parameters. A general frequency independent parameter for particles suited for MPI was found in the ratio between characteristic frequency and excitation frequency, which ideally lies between two and three.

Since it is very time consuming to perform phantom experiments in MPI for many different tracers to obtain quantitative information about the potential resolution, a new characterization technique was developed that employs MPS measurements at different static offset fields. Using this data, synthetic 1D MPI signals of virtual resolution phantoms for the commercially available FeraSpin series were generated and the resolution was found to be dependent on the noise level. Based on the characterization results, a general expression was found for the resolution. Moreover, the relationship between the maximum available spatial frequency and resolution could experimentally be confirmed. The implication of these observations is that

a shallow harmonic decay is more important than just a high third harmonic amplitude, which is often taken as an indicator for suitable MPI tracers. This was confirmed by characterizing a simulated particle suspension that exhibited a very large third harmonic amplitude and whose decay was comparable to FeraSpin XL. Here, only slight improvements in the resolution could be observed for the simulated suspension in comparison to FeraSpin XL.

It was furthermore introduced that the offset field supported MPS characterization could also be used to perform experiments regarding the influence of precipitated or immobilized particles on the image quality when a system function of colloidally stable suspended particles is used for reconstruction. This method might also be applied for experiments regarding mobility MPI or multi-color MPI if an MPI scanner is not available.

Besides the 1D characterization, a similar approach in 2D was presented, where not only the pure harmonics, but also mixed frequencies were considered regarding the prediction of the achievable resolution. Here, the deviations between prediction and reconstruction were slightly higher, but still in good agreement with the reconstruction results.

To test the comparability of the 1D offset MPS and 3D MPI sequences, experiments with phantoms consisting of two particle filled bores and a distance in between corresponding to the bore diameter were performed with different combinations of bore diameters and particle concentrations. Based on three phantoms that were close to the experimental resolution limit and an estimated noise level, the results of the three phantoms could be reproduced via the offset MPS method, confirming a general comparability between 1D and 3D sequences.

Overall, a link between elemental structural parameters of the particles and the MPS signal, as well as a link between MPS signal and spatial resolution could be established. This essentially enables the parameters, such as the magnetic core size or the effective anisotropy constant, to be linked to the potential resolution that may be achieved with a tracer. This may be used to perform more application oriented tracer characterizations, which will be important for preclinical MPI experiments where only the potential imaging performance is important, as well as for estimations regarding the theoretically achievable resolution in MPI.

The results in this thesis yield several implications regarding image quality. It was shown that the spatial frequencies in 1D that correspond to the pure harmonics, and in 2D and 3D that are also based on the mixed frequencies, directly influence the achievable spatial resolution. This implies that frequency components with high spatial frequencies above noise are necessary to achieve a high resolution. The particles with the highest harmonic amplitude and therefore spatial frequencies can mostly be found in the regime of Néel rotation and ideally have very low effective anisotropy constants.

Therefore, the SNR, especially in the regime of higher harmonics, is the crucial factor for the achievable spatial resolution. The improvement of the SNR can naturally be achieved via increasing the signal strength or decreasing the noise. Increasing the signal strength can be achieved by increasing the magnetic field strength, applying more MNP, or improving the tracer. Besides general limitations like energy consumption and heating of the excitation coils, the field parameters frequency and magnetic field strength are also limited by the patient health, specifically the peripheral nerve stimulation and the specific absorption rate [11] [116]. Due to safety regulations, it is not possible to increase the amount of particles indefinite. The increase of the signal therefore needs to be achieved by improving the tracer. Due to the high-frequency excitation at $f = 25$ kHz or more, increasing the signal strength is a difficult trade-off between the magnetic moment and the rotational dynamics of the tracer. On the one hand, a large magnetic moment is necessary to generate a large signal. On the other hand, the moment depends on the core size of the tracer, which, together with the effective anisotropy constant, determines the time necessary for the internal reversal of the moment to align to the external field. Depending on the size of the effective anisotropy constant, there may be a small regime of core sizes, in which the spectral amplitudes are maximized. The optimization of MNP in terms of their performance in MPI is therefore physically limited and cannot be improved indefinitely.

The improvement of tracers within its physical limits alone might be not enough for MPI when thinking about upscaling the principle to a human-sized scanner. To improve the SNR, it will also be necessary to work on techniques to improve signal purity and decrease the noise level. Given the relationship between resolution and SNR and the effort that is put into finding tracers with spectral amplitudes several times larger than current MNP, it is also noteworthy that a decrease of the noise level has the same impact as an improvement of the spectral amplitudes by the

same factor. The optimization of colloidally stable, high performant tracers as well as building an imaging system with the lowest possible background noise will be a difficult task as MPI is a very complex imaging technique. Yet, for MPI to find application in hospitals as an alternative imaging device for angiography and nuclear medicine imaging, it will be crucial to improve the SNR in both aspects.

Appendices

A. Simulation of the third harmonic amplitude at 5 mT and 12 mT drive field

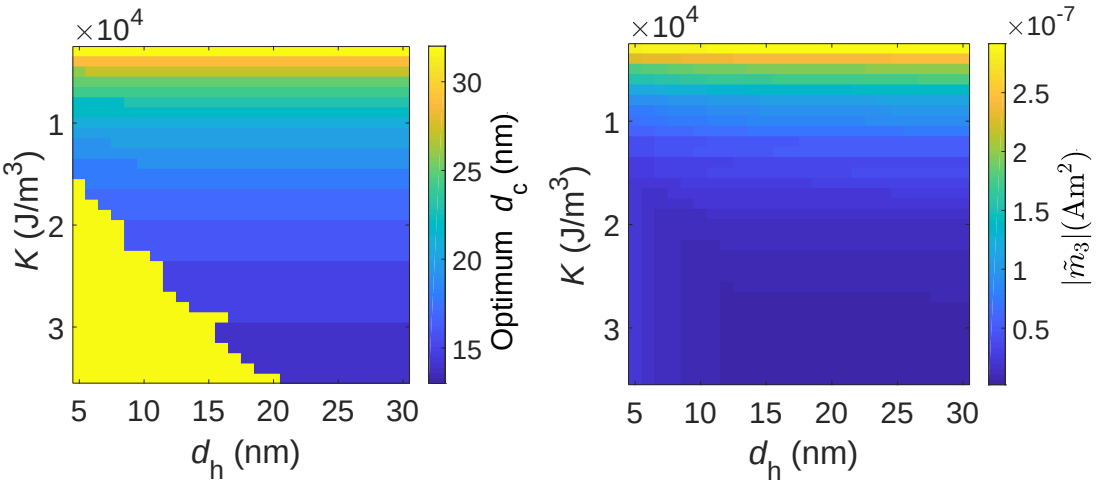

Figure 90: Optimum tracers for $f = 25$ kHz and $B_{\text{drive}} = 5$ mT. Left: Core size with the highest third harmonic amplitude $|\tilde{m}_3|$ for every combination of effective anisotropy constant and hydrodynamic shell thickness; Right: Third harmonic amplitude $|\tilde{m}_3|$ of respective optimum particle core size.

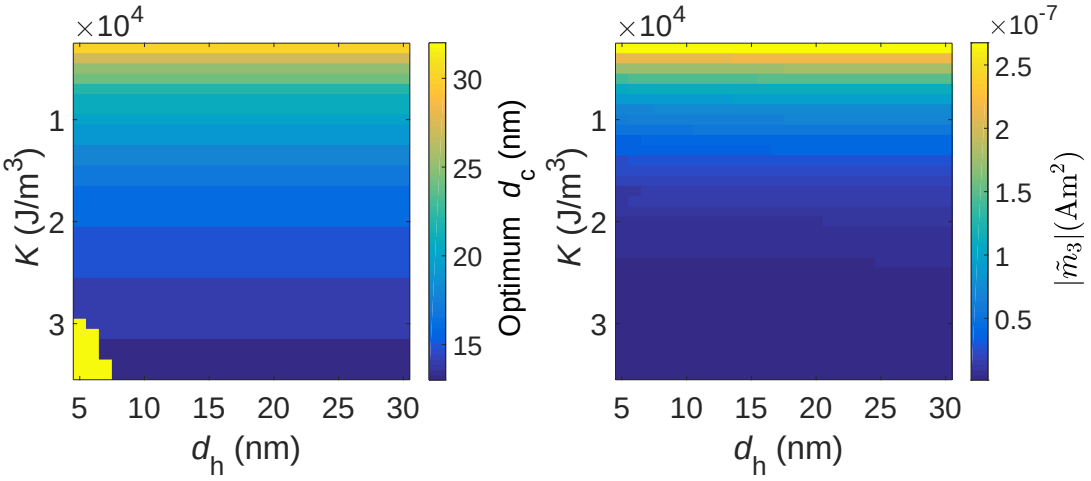

Figure 91: Optimum tracers for $f = 125$ kHz and $B_{\text{drive}} = 5$ mT. Left: Core size with the highest third harmonic amplitude $|\tilde{m}_3|$ for every combination of effective anisotropy constant and hydrodynamic shell thickness; Right: Third harmonic amplitude $|\tilde{m}_3|$ of respective optimum particle core size.

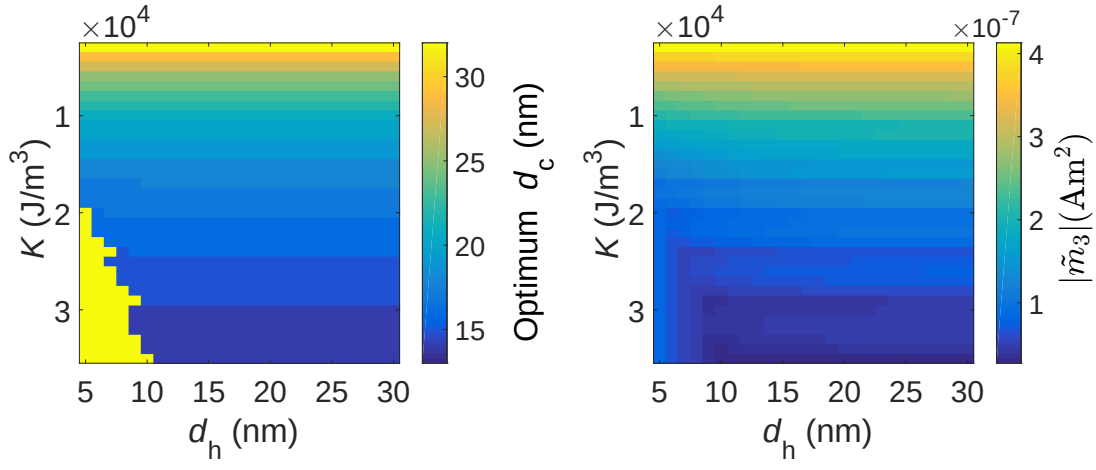

Figure 92: Optimum tracers for $f = 25$ kHz and $B_{\text{Drive}} = 12$ mT. Left: Core size with the highest third harmonic amplitude $|\tilde{m}_3|$ for every combination of effective anisotropy constant and hydrodynamic shell thickness; Right: Third harmonic amplitude $|\tilde{m}_3|$ of respective optimum particle core size.

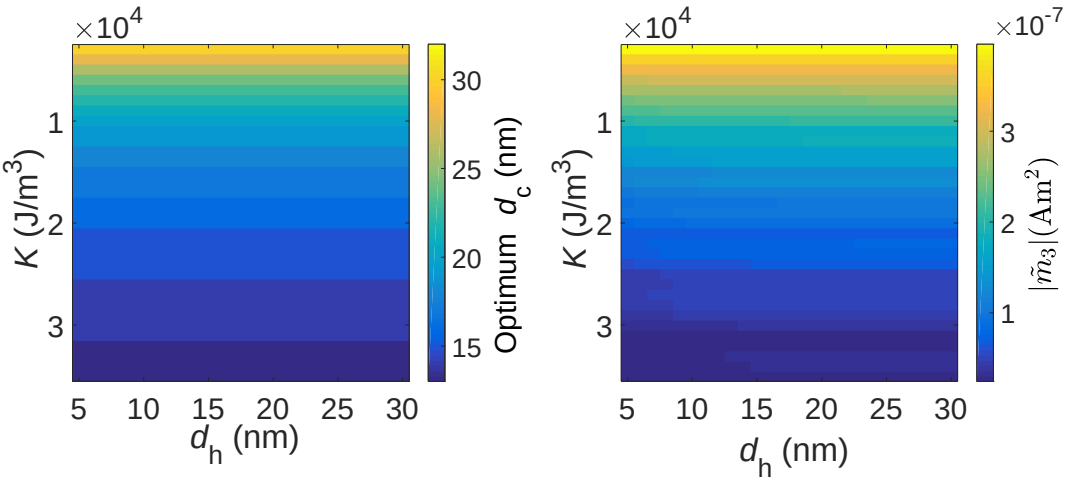

Figure 93: Optimum tracers for $f = 125$ kHz and $B_{\text{drive}} = 12$ mT. Left: Core size with the highest third harmonic amplitude $|\tilde{m}_3|$ for every combination of effective anisotropy constant and hydrodynamic shell thickness; Right: Third harmonic amplitude $|\tilde{m}_3|$ of respective optimum particle core size.

B. Further characterization results of the FeraSpin Series with variable object size

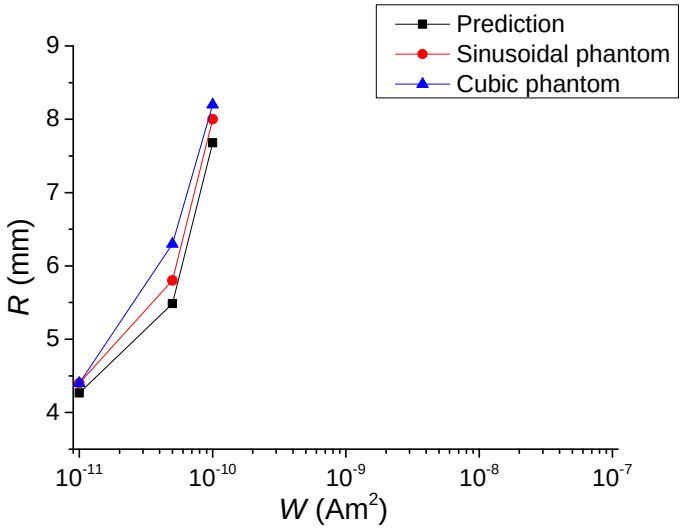

Figure 94: Resolution characterization of FeraSpin XS.

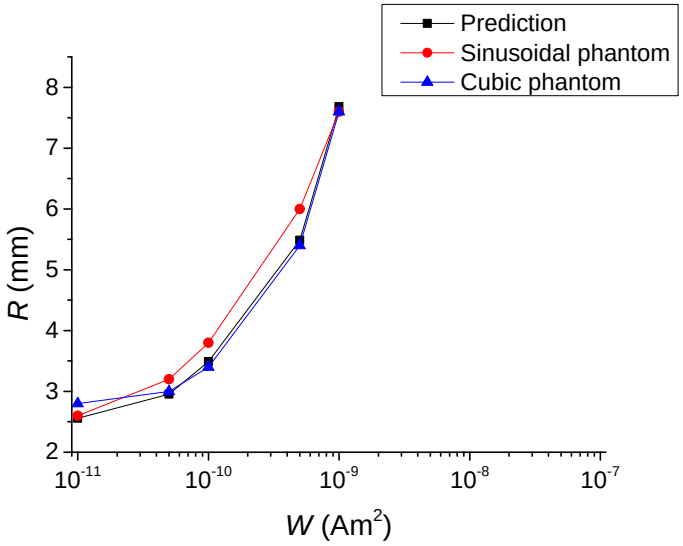

Figure 95: Resolution characterization of FeraSpin S.

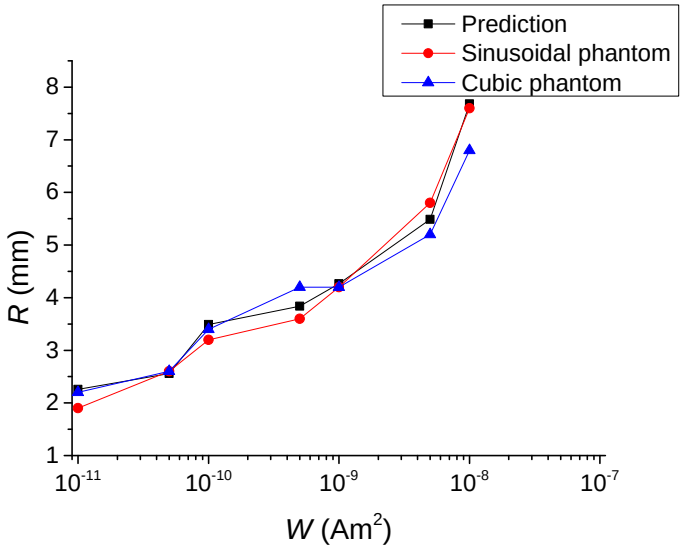

Figure 96: Resolution characterization of FeraSpin M.

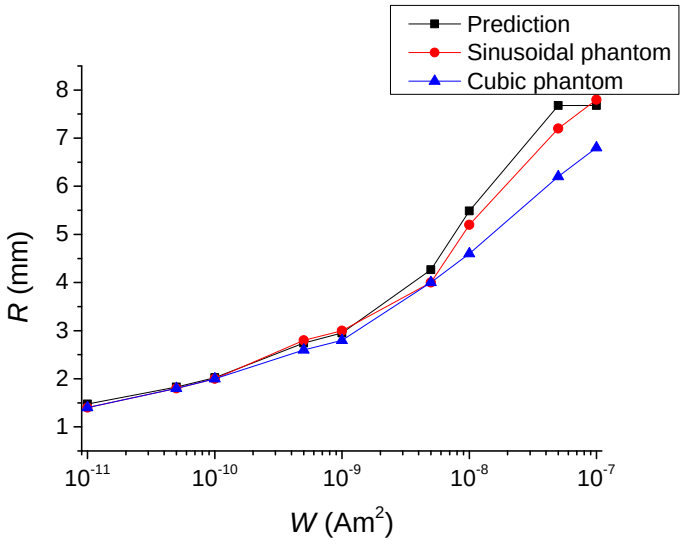

Figure 97: Resolution characterization of FeraSpin L.

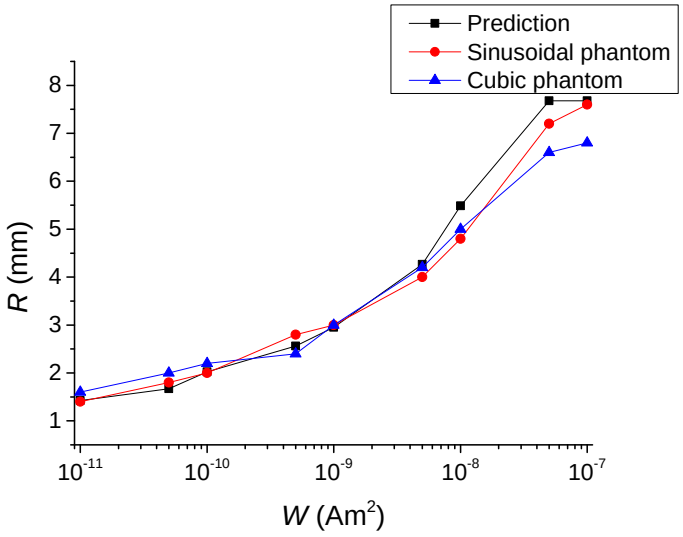

Figure 98: Resolution characterization of FeraSpin XL.

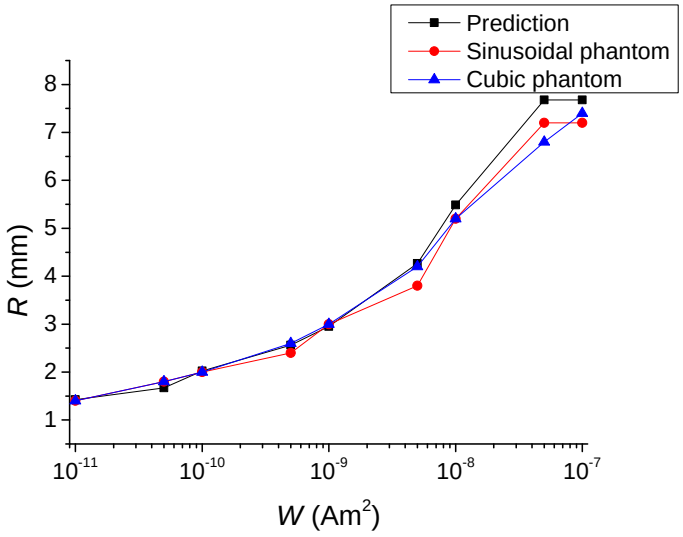

Figure 99: Resolution characterization of FeraSpin XXL.

C. Further characterization results of the FeraSpin Series with constant object size

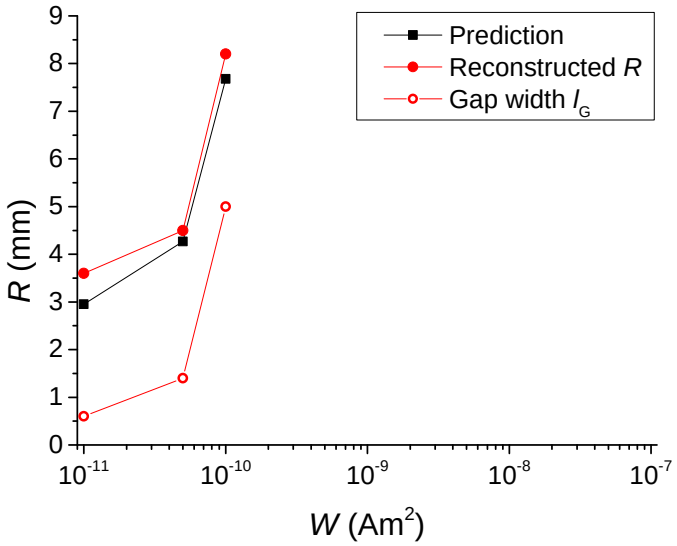

Figure 100: Resolution characterization of FeraSpin XS with constant object sizes.

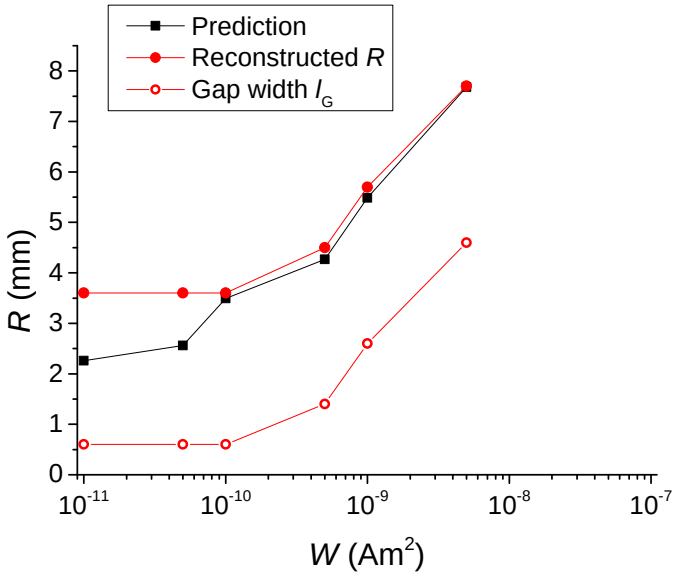

Figure 101: Resolution characterization of FeraSpin S with constant object sizes.

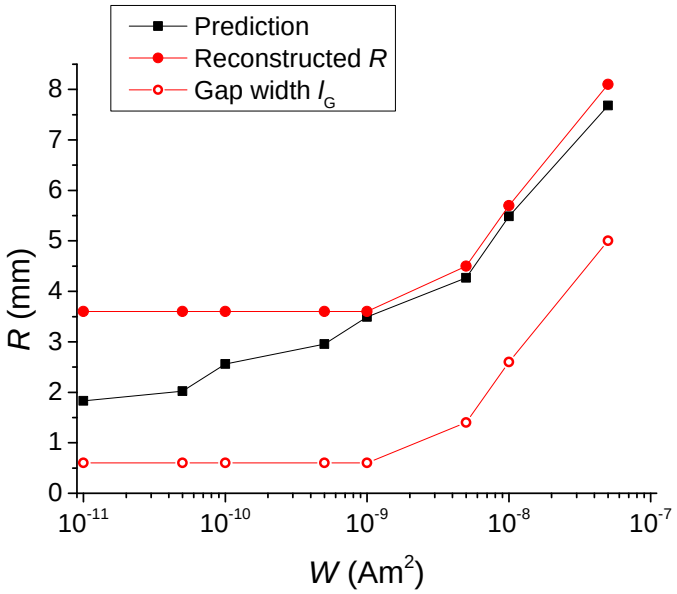

Figure 102: Resolution characterization of FeraSpin M with constant object sizes.

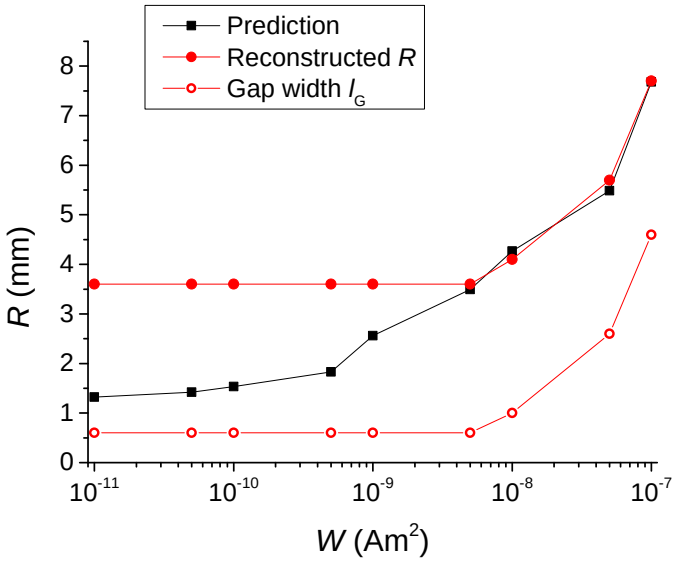

Figure 103: Resolution characterization of FeraSpin L with constant object sizes.

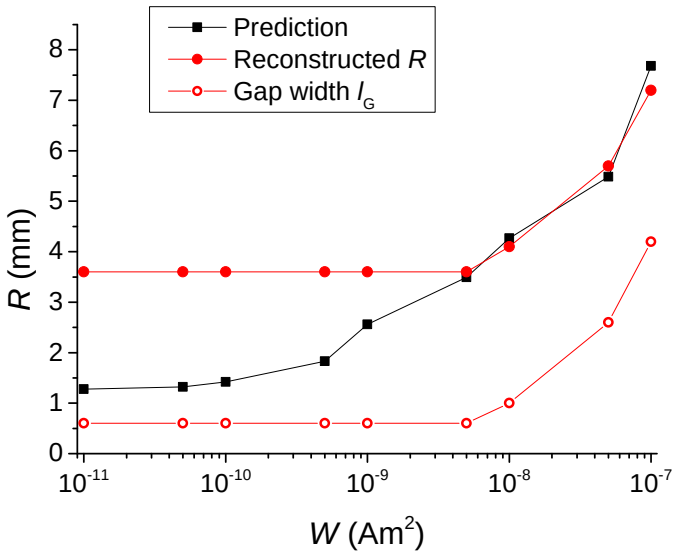

Figure 104: Resolution characterization of FeraSpin XL with constant object sizes.

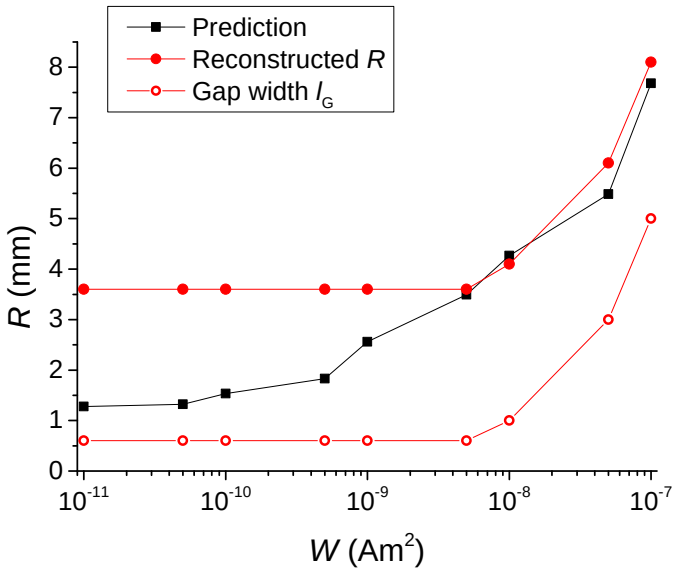

Figure 105: Resolution characterization of FeraSpin XXL with constant object sizes.

Publications

Papers

- J. Leliaert, **D. Schmidt**, O. Posth, M. Liebl, D. Eberbeck, A. Coene, U. Steinhoff, F. Wiekhorst, B. Van Waeyenberge and L. Dupré. Determining the hydrodynamic size distribution of magnetic nanoparticles from magnetorelaxometry data with Kaczmarz' algorithm, *Journal of Physics D: Applied Physics*, vol. 50, no. 19., 195002, 2017.

- D. Heinke, A. Kraupner, D. Eberbeck, **D. Schmidt**, P. Radon, R. Uebe, D. Schüler, A. Briel. MPS and MRI efficacy of magnetosomes from wild-type and mutant bacterial strains. *International Journal on Magnetic Particle Imaging*, vol. 3, no. 2, 2017.

- **D. Schmidt**, D. Eberbeck, U. Steinhoff and F. Wiekhorst. Finding the magnetic size distribution of magnetic nanoparticles from magnetization measurements via the iterative Kaczmarz algorithm. *Journal of Magnetism and Magnetic Materials*, vol. 431, pp. 33-37, 2017.

- **D. Schmidt**, M. Graeser, A. von Gladiss, TM. Buzug, U. Steinhoff. Imaging Characterization of MPI Tracers Employing Offset Measurements in a two Dimensional Magnetic Particle Spectrometer. *International Journal on Magnetic Particle Imaging*, vol. 2, no. 1, 2016.

- D. Heinke, N. Gehrke, **D. Schmidt**, U. Steinhoff, T. Viereck, H. Remmer, F. Ludwig, M. Pósfai and A. Briel. Diffusion-Controlled Synthesis of Magnetic Nanoparticles. *International Journal on Magnetic Particle Imaging*, vol. 2, no. 1, 2016.

- **D. Schmidt**, F. Palmetshofer and U. Steinhoff. Parameterization of the harmonic content of the complex MPI signal of magnetic tracers using a set of polynomial coefficients. *Journal of Magnetism and Magnetic Materials*, vol. 380, pp. 276-279, 2015.

- **D. Schmidt**, F. Palmetshofer, D. Heinke, U. Steinhoff and F. Ludwig. A Phenomenological Description of the MPS Signal Using a Model for the Field Dependence of the Effective Relaxation Time. *IEEE Transactions on Magnetics*, vol. 51, no. 2, pp. 1-4, 2015.

Presentations

- **D. Schmidt**, F. Palmetshofer , D. Heinke, D. Gutkelch , P. Radon and U. Steinhoff. Characterizing the imaging performance of magnetic tracers by Magnetic Particle Spectroscopy in an offset field. *DGBMT Jahrestagung (Hannover, Germany), 2015.*

- **D. Schmidt**, F. Palmetshofer, D. Heinke, D. Gutkelch, P. Radon, O. Posth, U. Steinhoff. Imaging characterization of magnetic nanoparticles for Magnetic Particle Imaging using offset field supported Magnetic Particle Spectroscopy. *German Ferrofluid Workshop (Rostock, Germany), 2015.*

- **D. Schmidt**, F. Palmetshofer , D. Heinke, D. Gutkelch , P. Radon and U. Steinhoff. Characterizing the imaging performance of magnetic tracers by Magnetic Particle Spectroscopy in an offset field. *International Workshop on Magnetic Particle Imaging (Istanbul, Turkey), 2015.*

- **D. Schmidt**, F. Palmetshofer and U. Steinhoff. Parametrisierung des MPI-Signals mittels Taylorentwicklung der Magnetisierungsfunktion magnetischer Nanopartikel. *Workshop Biosignalverarbeitung (Berlin, Germany), 2014.*

- **D. Schmidt**, F. Palmetshofer, D. Heinke, U. Steinhoff and F. Ludwig. A Phenomenological Description of the MPS Signal Using a Model for the Field Dependence of the Effective Relaxation Time. *International Workshop on Magnetic Particle Imaging (Berlin, Germany), 2014.*

Other

- **D. Schmidt**, F. Palmetshofer and U. Steinhoff. Neue präklinische Kontrastmittel für Magnetic Particle Imaging (MPI): Teilvorhaben: Charakterisierung neuer magnetischer Nanopartikel: Statische magnetische Eigenschaften und MPI-Effizienz. Förderkennzeichen KF2303711UW2, Berichtszeitraum 01.01 2013-30.06.2015.

- F. Wiekhorst, Physikalisch-Technische Bundesanstalt, N. Löwa, L. Trahms, D. Eberbeck, O. Kosch, P. Radon, **D. Schmidt**. Magnetic Particle Imaging Technologie (MAPIT) : Teilvorhaben: Magnetische Messverfahren für MPI-Tracer : im Rahmenprogramm Werkstoffinovationen für Industrie und Gesellschaft - WING : Abschlussbericht zum BMBF-Verbundprojekt : Berichtszeitraum: 01.01.2011-31.12.2015

References

[1] H. Arami, R.M. Ferguson, A.P. Khandhar, and K.M. Krishnan. Size-dependent ferrohydrodynamic relaxometry of magnetic particle imaging tracers in different environments. *Medical physics*, 40(7):071904, 2013.

[2] A.D. Arelaro, A.L. Brandl, E. Lima, L.F. Gamarra, G.E.S. Brito, W.M. Pontuschka, and G.F. Goya. Interparticle interactions and surface contribution to the effective anisotropy in biocompatible iron oxide nanoparticles used for contrast agents. *Journal of applied physics*, 97(10):10J316, 2005.

[3] M. Arruebo, R. Fernández-Pacheco, M.R. Ibarra, and J. Santamaría. Magnetic nanoparticles for drug delivery. *Nano today*, 2(3):22–32, 2007.

[4] L. Bauer, M.H. Pablico-Lansigan, R. Deissler, M. Martens, R. Brown, A.C.S. Samia, and M.A. Griswold. Magnetic particle spectroscopy of magnetite-polyethylene nanocomposite films: A novel sample for mpi tracer design. In *Magnetic Particle Imaging (IWMPI), 2013 International Workshop on*, pages 1–1, 2013.

[5] C.P. Bean and J.D. Livingston. Superparamagnetism. *Journal of Applied Physics*, 30(4):120–129, 1959.

[6] D.V. Berkov, P. Görnert, N. Buske, C. Gansau, J. Mueller, M. Giersig, W. Neumann, and D. Su. New method for the determination of the particle magnetic moment distribution in a ferrofluid. *Journal of Physics D: Applied Physics*, 33(4):331, 2000.

[7] M. Bertero and P. Boccacci. *Introduction to inverse problems in imaging*. CRC press, 1998.

[8] S. Biederer, T. Knopp, T.F. Sattel, K. Lüdtke-Buzug, B. Gleich, J. Weizenecker, J. Borgert, and T.M. Buzug. Magnetization response spectroscopy of superparamagnetic nanoparticles for magnetic particle imaging. *Journal of Physics D: Applied Physics*, 42(20):205007, 2009.

[9] R.C. Black and F.C. Wellstood. *The SQUID Handbook. Vol. II: Applications of SQUIDs and SQUID Systems*, chapter Measurements of Magnetism and Magnetic Properties of Matter, pages 392–435. Wiley-VCH, Weinheim, 2006.

[10] S. Bogren, A. Fornara, F. Ludwig, M. del Puerto Morales, U. Steinhoff, M.F. Hansen, O. Kazakova, and C. Johansson. Classification of magnetic nanoparticle systems - synthesis, standardization and analysis methods in the nanomag project. *International journal of molecular sciences*, 16(9):20308–20325, 2015.

[11] J. Bohnert, B. Gleich, J. Weizenecker, J. Borgert, and O. Dössel. Evaluation of induced current densities and SAR in the human body by strong magnetic fields around 100 kHz. In *IFMBE Proceedings*, pages 2532–2535. Springer Science + Business Media, 2009.

[12] G.D. Boreman. *Modulation Transfer Function in Optical and Electro-Optical Systems*. SPIE-Intl Soc Optical Eng, 2001.

[13] W.F. Brown Jr. Thermal fluctuations of a single-domain particle. *Journal of Applied Physics*, 34(4):1319–1320, 1963.

[14] D.M. Bruls, T.H. Evers, J.A.H. Kahlman, P.J.W. Van Lankvelt, M. Ovsyanko, E.G.M. Pelssers, J.J.H.B. Schleipen, F.K. De Theije, C.A. Verschuren, T. Van Der Wijk, et al. Rapid integrated biosensor for multiplexed immunoassays based on actuated magnetic nanoparticles. *Lab on a Chip*, 9(24):3504–3510, 2009.

[15] J. T. Bushberg, J. A. Seibert, E. M. Leidholdt, J. M. Boone, and M. Mahesh. *The Essential Physics of Medical Imaging, Third Edition.* American Association of Physicists in Medicine (AAPM), 2013.

[16] R.W. Chantrell, S.R. Hoon, and B.K. Tanner. Time-dependent magnetization in fine-particle ferromagnetic systems. *Journal of magnetism and magnetic materials*, 38(2):133–141, 1983.

[17] Y.R. Chemla, H.L. Grossman, T.S. Lee, J. Clarke, M. Adamkiewicz, and B.B. Buchanan. A new study of bacterial motion: superconducting quantum interference device microscopy of magnetotactic bacteria. *Biophysical journal*, 76(6):3323–3330, 1999.

[18] D.R. Dance, S. Christofides, A.D.A. Maidment, I.D. McLean, and K.H. Ng. *Diagnostic Radiology Physics*. IAEA (International Atomic Energy Agency), 2014.

[19] B.S. Deaver Jr and W.S. Goree. Some techniques for sensitive magnetic measurements using superconducting circuits and magnetic shields. *Review of Scientific Instruments*, 38(3):311–318, 1967.

[20] P.J.W. Debye. *Polar molecules*. Chemical Catalog Company, Incorporated, 1929.

[21] R.J. Deissler, Y. Wu, and M.A. Martens. Dependence of brownian and néel relaxation times on magnetic field strength. *Medical physics*, 41(1):012301, 2014.

[22] A. Demortiere, P. Panissod, B.P. Pichon, G. Pourroy, D. Guillon, B. Donnio, and S. Begin-Colin. Size-dependent properties of magnetic iron oxide nanocrystals. *Nanoscale*, 3(1):225–232, 2011.

[23] J. Dieckhoff, D. Eberbeck, M. Schilling, and F. Ludwig. Magnetic-field dependence of brownian and néel relaxation times. *Journal of applied physics*, 119(4):043903, 2016.

[24] J. Dobson. Gene therapy progress and prospects: magnetic nanoparticle-based gene delivery. *Gene therapy*, 13(4):283–287, 2006.

[25] J. Dobson. Magnetic nanoparticles for drug delivery. *Drug development research*, 67(1):55–60, 2006.

[26] P. Dutta, A. Manivannan, M.S. Seehra, N. Shah, and G.P. Huffman. Magnetic properties of nearly defect-free maghemite nanocrystals. *Physical Review B*, 70(17):174428, 2004.

[27] D. Eberbeck, C.L. Dennis, N.F. Huls, K.L. Krycka, C. Gruttner, and F. Westphal. Multicore magnetic nanoparticles for magnetic particle imaging. *Magnetics, IEEE Transactions on*, 49(1):269–274, 2013.

[28] D. Eberbeck, F. Wiekhorst, S. Wagner, and L. Trahms. How the size distribution of magnetic nanoparticles determines their magnetic particle imaging performance. *Applied Physics Letters*, 98:182502, 2011.

[29] R. Egli. Characterization of individual rock magnetic components by analysis of remanence curves, 1. unmixing natural sediments. *Studia geophysica et geodaetica*, 48(2):391–446, 2004.

[30] A. Einstein. Über die von der molekularkinetischen theorie der wärme geforderte bewegung von in ruhenden flüssigkeiten suspendierten teilchen. *Annalen der physik*, 322(8):549–560, 1905.

[31] R.M. Ferguson, A.P. Khandhar, H. Arami, L. Hua, O. Hovorka, and K.M. Krishnan. Tailoring the magnetic and pharmacokinetic properties of iron oxide magnetic particle imaging tracers. *Biomedizinische Technik/Biomedical Engineering*, 58(6):493–507, 2013.

[32] R.M. Ferguson, A.P. Khandhar, S.J. Kemp, H. Arami, E.U. Saritas, L.R. Croft, J. Konkle, P.W. Goodwill, A. Halkola, J. Rahmer, J. Borgert, and S.M. Conolloy. Magnetic particle imaging with tailored iron oxide nanoparticle tracers. *Medical Imaging, IEEE Transactions on*, 34(5):1077–1084, 2015.

[33] R.M. Ferguson, A.P. Khandhar, and K.M. Krishnan. Tracer design for magnetic particle imaging. *Journal of applied physics*, 111(7):07B318, 2012.

[34] R.M. Ferguson, K.R. Minard, A.P. Khandhar, and K.M. Krishnan. Optimizing magnetite nanoparticles for mass sensitivity in magnetic particle imaging. *Medical physics*, 38(3):1619–1626, 2011.

[35] R.M. Ferguson, K.R. Minard, and K.M. Krishnan. Optimization of nanoparticle core size for magnetic particle imaging. *Journal of magnetism and magnetic materials*, 321(10):1548–1551, 2009.

[36] J. Frenkel and J. Dorfman. Spontaneous and induced magnetisation in ferromagnetic bodies. *Nature*, 126(3173):274–275, 1930.

[37] N. Gehrke, A. Briel, F. Ludwig, H. Remmer, T. Wawrzik, and S. Wellert. New perspectives for mpi: a toolbox for tracer research. In *Magnetic Particle Imaging*, pages 99–103, 2012.

[38] N. Gehrke, D. Heinke, D. Eberbeck, and A. Briel. The potential of clustered core magnetic particles for mpi. In *Magnetic Particle Imaging (IWMPI), 2013 International Workshop on*, pages 1–1, 2013.

[39] B. Gleich and J. Weizenecker. Tomographic imaging using the nonlinear response of magnetic particles. *Nature*, 435(7046):1214–1217, 2005.

[40] S. Goldfarb, P.A. McCullough, J. McDermott, and S.B. Gay. Contrast-induced acute kidney injury: specialty-specific protocols for interventional radiology, diagnostic computed tomography radiology, and interventional cardiology. *Mayo Clinic Proceedings*, 84(2):170–179, 2009.

[41] J.-L. Gong, Y. Liang, Y. Huang, J.-W. Chen, J.-H. Jiang, G.-L. Shen, and R.-Q. Yu. Ag/sio 2 core-shell nanoparticle-based surface-enhanced raman probes for immunoassay of cancer marker using silica-coated magnetic nanoparticles as separation tools. *Biosensors and Bioelectronics*, 22(7):1501–1507, 2007.

[42] P.W. Goodwill and S.M. Conolly. The x-space formulation of the magnetic particle imaging process: 1-d signal, resolution, bandwidth, snr, sar, and magnetostimulation. *Medical Imaging, IEEE Transactions on*, 29(11):1851–1859, 2010.

[43] P.W. Goodwill and S.M. Conolly. Multidimensional x-space magnetic particle imaging. *Medical Imaging, IEEE Transactions on*, 30:1581–1590, 2011.

[44] P.W. Goodwill, E.U. Saritas, L.R. Croft, T.N. Kim, K.M. Krishnan, D.V. Schaffer, and S.M. Conolly. X-space mpi: magnetic nanoparticles for safe medical imaging. *Advanced materials*, 24(28):3870–3877, 2012.

[45] P.W. Goodwill, A. Tamrazian, L.R. Croft, C.D. Lu, E.M. Johnson, R. Pidaparthi, R.M. Ferguson, A.P. Khandhar, K.M. Krishnan, and S.M. Conolly. Ferrohydrodynamic relaxometry for magnetic particle imaging. *Applied Physics Letters*, 98(26):262502, 2011.

[46] G.F. Goya, T.S. Berquo, F.C. Fonseca, and M.P. Morales. Static and dynamic magnetic properties of spherical magnetite nanoparticles. *Journal of Applied Physics*, 94(5):3520–3528, 2003.

[47] M. Graeser, M. Ahlborg, A. Behrends, K. Bente, G. Bringout, C. Debbeler, A. von Gladiss, K. Graefe, C. Kaethner, S. Kaufmann, K. Lüdtke-Buzug, H. Medimagh, J. Stelzner, M. Weber, and T.M. Buzug. A device for measuring the trajectory dependent magnetic particle performance for mpi. In *5th International Workshop on Magnetic Particle Imaging (IWMPI 2015): Book of Abstracts*, 2015.

[48] M. Graeser, K. Bente, A. Neumann, and T.M. Buzug. Trajectory dependent particle response for anisotropic mono domain particles in magnetic particle imaging. *Journal of Physics D: Applied Physics*, 49(4):045007, 2015.

[49] M. Graeser, M. Grüttner, S. Biederer, H. Wojtczyk, W. Tenner, T. Sattel, B. Gleich, J. Borgert, T. Knopp, and T.M. Buzug. Determination of a 1d-mpi-system-function using a magnetic particle spectroscope. *44. Jahrestagung der Deutschen Gesellschaft für Biomedizinische Technik im VDE*, 56, 2011.

[50] K. Gräfe, T.F. Sattel, K. Lüdtke-Buzug, D. Finas, J. Borgert, and T.M. Buzug. *Magnetic Particle Imaging*, chapter Magnetic-Particle-Imaging for Sentinel Lymph Node Biopsy in Breast Cancer, pages 237–241. Springer, 2012.

[51] M. Grüttner, T. Knopp, J. Franke, M. Heidenreich, J. Rahmer, A. Halkola, C. Kaethner, J. Borgert, and T.M. Buzug. On the formulation of the image reconstruction problem in magnetic particle imaging. *Biomedizinische Technik/Biomedical Engineering*, 58(6):583–591, 2013.

[52] J. Haegele, S. Biederer, H. Wojtczyk, M. Gräser, T. Knopp, T.M. Buzug, J. Barkhausen, and F.M. Vogt. Toward cardiovascular interventions guided by magnetic particle imaging: First instrument characterization. *Magnetic resonance in medicine*, 69(6):1761–1767, 2013.

[53] P.C. Hansen. *Rank-Deficient and Discrete Ill-Posed Problems: Numerical Aspects of Linear Inversion*. Society for Industrial and Applied Mathematics, 1998.

[54] J. Hausleiter, T. Meyer, F. Hermann, M. Hadamitzky, M. Krebs, T.C. Gerber, C. McCollough, S. Martinoff, A. Kastrati, A. Schömig, et al. Estimated radiation dose associated with cardiac ct angiography. *Jama*, 301(5):500–507, 2009.

[55] David Heinke, Nicole Gehrke, Daniel Schmidt, Uwe Steinhoff, Thilo Viereck, Hilke Remmer, Frank Ludwig, Mihály Pósfai, and Andreas Briel. Diffusion-controlled synthesis of magnetic nanoparticles. *International Journal on Magnetic Particle Imaging*, 2(1), 2016.

[56] R. Hergt, S. Dutz, and M. Röder. Effects of size distribution on hysteresis losses of magnetic nanoparticles for hyperthermia. *Journal of Physics: Condensed Matter*, 20(38):385214, 2008.

[57] G.C. Hurst, J. Hua, O.P. Simonetti, and J.L. Duerk. Signal-to-noise, resolution, and bias function analysis of asymmetric sampling with zero-padded magnitude ft reconstruction. *Magnetic resonance in medicine*, 27(2):247–269, 1992.

[58] J.H. Ix, N. Mercado, M.G. Shlipak, P.A. Lemos, E. Boersma, W. Lindeboom, W.W. O'Neill, W. Wijns, and P.W. Serruys. Association of chronic kidney disease with clinical outcomes after coronary revascularization: the arterial revascularization therapies study (arts). *American heart journal*, 149(3):512–519, 2005.

[59] M. Johannsen, U. Gneveckow, L. Eckelt, A. Feussner, N. Waldöfner, R. Scholz, S. Deger, P. Wust, S.A. Loening, and A. Jordan. Clinical hyperthermia of prostate cancer using magnetic nanoparticles: presentation of a new interstitial technique. *International journal of hyperthermia*, 21(7):637–647, 2005.

[60] P.F. Judy. The line spread function and modulation transfer function of a computed tomographic scanner. *Medical physics*, 3(4):233–236, 1976.

[61] S. Kaczmarz. Angenäherte auflösung von systemen linearer gleichungen. *Bulletin International de l'Academie Polonaise des Sciences et des Lettres*, 35:355–357, 1937.

[62] J. Kaipio and E. Somersalo. *Statistical and Computational Inverse Problems*, volume 160. Springer Science & Business Media, 2006.

[63] A.P. Khandhar. *Biomedical imaging and therapy with physically and physiologically tailored magnetic nanoparticles*. PhD thesis, 2013.

[64] A.P. Khandhar, R.M. Ferguson, H. Arami, S.J. Kemp, and K.M. Krishnan. Tuning surface coatings of optimized magnetite nanoparticle tracers for in vivo magnetic particle imaging. *IEEE transactions on magnetics*, 51(2):1–4, 2015.

[65] A.P. Khandhar, R.M. Ferguson, H. Arami, and K.M. Krishnan. Monodisperse magnetite nanoparticle tracers for in vivo magnetic particle imaging. *Biomaterials*, 34(15):3837–3845, 2013.

[66] A.P. Khandhar, R.M. Ferguson, and K.M. Krishnan. Monodispersed magnetite nanoparticles optimized for magnetic fluid hyperthermia: Implications in biological systems. *Journal of applied physics*, 109(7):07B310, 2011.

[67] A.P. Khandhar, R.M. Ferguson, J.A. Simon, and K.M. Krishnan. Tailored magnetic nanoparticles for optimizing magnetic fluid hyperthermia. *Journal of Biomedical Materials Research Part A*, 100(3):728–737, 2012.

[68] F.M. Kievit, Z.R. Stephen, O. Veiseh, H. Arami, T. Wang, V.P. Lai, J.O. Park, R.G. Ellenbogen, M.L. Disis, and M. Zhang. Targeting of primary breast cancers and metastases in a transgenic mouse model using rationally designed multifunctional spions. *ACS nano*, 6(3):2591–2601, 2012.

[69] C. Kittel. Theory of the structure of ferromagnetic domains in films and small particles. *Physical Review*, 70(11-12):965, 1946.

[70] T. Knopp, S. Biederer, T.F. Sattel, M. Erbe, and T.M. Buzug. Prediction of the spatial resolution of magnetic particle imaging using the modulation transfer function of the imaging process. *Medical Imaging, IEEE Transactions on*, 30(6):1284–1292, 2011.

[71] T. Knopp, S. Biederer, T.F. Sattel, J. Rahmer, J. Weizenecker, B. Gleich, J. Borgert, and T.M. Buzug. 2d model-based reconstruction for magnetic particle imaging. *Medical physics*, 37(2):485–491, 2010.

[72] T. Knopp and T.T.M. Buzug. *Magnetic Particle Imaging*. Springer Science + Business Media, 2012.

[73] O. Kosch, N. Löwa, F. Wiekhorst, and L. Trahms. Does a highly concentrated sample genegene a better system function? In *6th International Workshop on Magnetic Particle Imaging (IWMPI 2016): Book of Abstracts*, 2016.

[74] H. Kratz, D. Eberbeck, S. Wagner, J. Schnorr, and M. Taupitz. Tracer development for magnetic particle imaging. In *Magnetic Particle Imaging*, pages 123–127. Springer, 2012.

[75] C. Kuhlmann, A.P. Khandhar, R.M. Ferguson, S. Kemp, T. Wawrzik, M. Schilling, K.M. Krishnan, and F. Ludwig. Drive-field frequency dependent mpi performance of single-core magnetite nanoparticle tracers. *Magnetics, IEEE Transactions on*, 51(2), 2015.

[76] J. Lampe, C. Bassoy, J. Rahmer, J. Weizenecker, H. Voss, B. Gleich, and J. Borgert. Fast reconstruction in magnetic particle imaging. *Physics in medicine and biology*, 57(4):1113, 2012.

[77] L. Lartigue, P. Hugounenq, D. Alloyeau, S.P. Clarke, M. Lévy, J.-C. Bacri, R. Bazzi, D.F. Brougham, C. Wilhelm, and F. Gazeau. Cooperative organization in iron oxide multi-core nanoparticles potentiates their efficiency as heating mediators and mri contrast agents. *ACS nano*, 6(12):10935–10949, 2012.

[78] S. Laurent, D. Forge, M. Port, A. Roch, C. Robic, L. Vander Elst, and R.N. Muller. Magnetic iron oxide nanoparticles: Synthesis, stabilization, vectorization, physicochemical characterizations, and biological applications. *Chemical reviews*, 108(6):2064–2110, 2008.

[79] J.-H. Lee, J.-T. Jang, J.-S. Choi, S.-H. Moon, S.-H. Noh, J.-W. Kim, J.-G. Kim, I.-S. Kim, K.-I. Park, and J. Cheon. Exchange-coupled magnetic nanoparticles for efficient heat induction. *Nature nanotechnology*, 6(7):418–422, 2011.

[80] J. Leliaert, A. Vansteenkiste, A. Coene, L. Dupré, and B. Van Waeyenberge. Vinamax: a macrospin simulation tool for magnetic nanoparticles. *Medical & biological engineering & computing*, 53(4):309–317, 2014.

[81] E. Lima Jr, A.L. Brandl, A.D. Arelaro, and G.F. Goya. Spin disorder and magnetic anisotropy in fe3o4 nanoparticles. *arXiv preprint cond-mat/0505682*, 2005.

[82] P.-C. Lin, P.-H. Chou, S.-H. Chen, H.-K. Liao, K.-Y. Wang, Y.-J. Chen, and C.-C. Lin. Ethylene glycol-protected magnetic nanoparticles for a multiplexed immunoassay in human plasma. *Small*, 2(4):485–489, 2006.

[83] N. Löwa, P. Radon, O. Kosch, and F. Wiekhorst. Concentration dependent mpi tracer performance. *International Journal on Magnetic Particle Imaging*, 2(1), 2016.

[84] A.-H. Lu, E.L. Salabas, and F. Schüth. Magnetic nanoparticles: synthesis, protection, functionalization, and application. *Angewandte Chemie International Edition*, 46(8):1222–1244, 2007.

[85] K. Lu, P.W. Goodwill, B. Zheng, and S.M. Conolly. The impact of filtering direct-feedthrough on the x-space theory of magnetic particle imaging. In *SPIE Medical Imaging*, pages 79652I–79652I. International Society for Optics and Photonics, 2011.

[86] F. Ludwig, D. Eberbeck, N. Löwa, U. Steinhoff, T. Wawrzik, M. Schilling, and L. Trahms. Characterization of magnetic nanoparticle systems with respect to their magnetic particle imaging performance. *Biomedizinische Technik/Biomedical Engineering*, 58(6):535–545, 2013.

[87] F. Ludwig, E. Heim, and M. Schilling. Characterization of superparamagnetic nanoparticles by analyzing the magnetization and relaxation dynamics using fluxgate magnetometers. *Journal of applied physics*, 101(11):113909, 2007.

[88] F. Ludwig, E. Heim, and M. Schilling. Characterization of magnetic core–shell nanoparticles by fluxgate magnetorelaxometry, ac susceptibility, transmission electron microscopy and photon correlation spectroscopy - a comparative study. *Journal of magnetism and magnetic materials*, 321(10):1644–1647, 2009.

[89] F. Ludwig, O. Kazakova, L. Fernandez Barquin, A. Fornara, L. Trahms, U. Steinhoff, P. Svedlindh, E. Wetterskog, Q.A. Pankhurst, P. Southern, et al. Magnetic, structural, and particle size analysis of single-and multi-core magnetic nanoparticles. *Magnetics, IEEE Transactions on*, 50(11):1–4, 2014.

[90] F. Ludwig, C. Kuhlmann, T. Wawrzik, J. Dieckhoff, A. Lak, A.P. Kandhar, R.M. Ferguson, S.J. Kemp, and K.M. Krishnan. Dynamic magnetic properties of optimized magnetic nanoparticles for magnetic particle imaging. *IEEE Transactions on Magnetics*, 50(11):1–4, 2014.

[91] F. Ludwig, H. Remmer, C. Kuhlmann, T. Wawrzik, H. Arami, R.M. Ferguson, and K.M. Krishnan. Self-consistent magnetic properties of magnetite tracers optimized for magnetic particle imaging measured by ac susceptometry, magnetorelaxometry and magnetic particle spectroscopy. *Journal of magnetism and magnetic materials*, 360:169–173, 2014.

[92] F. Ludwig, T. Wawrzik, T. Yoshida, N. Gehrke, A. Briel, D. Eberbeck, and M. Schilling. Optimization of magnetic nanoparticles for magnetic particle imaging. *Magnetics, IEEE Transactions on*, 48(11):3780–3783, 2012.

[93] D.W. Marquardt. An algorithm for least-squares estimation of nonlinear parameters. *Journal of the Society for Industrial & Applied Mathematics*, 11(2):431–441, 1963.

[94] M.A. Martsenyuk, Y.L. Raikher, and M.I. Shliomis. On the kinetics of magnetization of suspensions of ferromagnetic particles. *Soviet Journal of Experimental and Theoretical Physics*, 65, 1974.

[95] S.C. McBain, H.P. Yiu, and J. Dobson. Magnetic nanoparticles for gene and drug delivery. *International journal of nanomedicine*, 3(2):169, 2008.

[96] S.E. McNeil. Nanotechnology for the biologist. *Journal of Leukocyte Biology*, 78(3):585–594, 2005.

[97] K. Murase, H. Takata, Y. Takeuchi, and S. Saito. Control of the temperature rise in magnetic hyperthermia with use of an external static magnetic field. *Physica Medica*, 29(6):624–630, 2013.

[98] O. Mykhaylyk, D. Eberbeck, N. Löwa, I. Almstätter, C. Plank, R. Braren, and L. Trahms. Magnetic particle spectroscopy characterization of the assemblies of magnetic nanoparticles. In *Magnetic Particle Imaging (IWMPI), 2015 5th International Workshop on*, pages 1–1, 2015.

[99] L. Néel. Théorie du traînage magnétique des ferromagnétiques en grains fins avec applications aux terres cuites. *Ann. géophys*, 5(2):99–136, 1949.

[100] N. Nitin, L.E.W. LaConte, O. Zurkiya, X. Hu, and G. Bao. Functionalization and peptide-based delivery of magnetic nanoparticles as an intracellular mri contrast agent. *JBIC Journal of Biological Inorganic Chemistry*, 9(6):706–712, 2004.

[101] J. Nowak, F. Wiekhorst, L. Trahms, and S. Odenbach. The influence of hydrodynamic diameter and core composition on the magnetoviscous effect of biocompatible ferrofluids. *Journal of Physics: Condensed Matter*, 26(17):176004, 2014.

[102] D. Ortega. *Magnetic Nanoparticles: From Fabrication to Clinical Applications*, chapter Structure and Magnetism in Magnetic Nanoparticles, pages 3–46. CRC press, 2012.

[103] M.H. Pablico-Lansigan, S.F. Situ, and A.-C.S. Samia. Magnetic particle imaging: advancements and perspectives for real-time in vivo monitoring and image-guided therapy. *Nanoscale*, 5(10):4040–4055, 2013.

[104] K.D. Pagana, T.J. Pagana, and T.N. Pagana. *Mosby's Diagnostic and Laboratory Test Reference*. Elsevier, 2015.

[105] Q.A. Pankhurst, J. Connolly, S.K. Jones, and J.J. Dobson. Applications of magnetic nanoparticles in biomedicine. *Journal of physics D: Applied physics*, 36(13):R167, 2003.

[106] J. Rahmer, A. Antonelli, C. Sfara, B. Tiemann, B. Gleich, M. Magnani, J. Weizenecker, and J. Borgert. Nanoparticle encapsulation in red blood cells enables blood-pool magnetic particle imaging hours after injection. *Physics in medicine and biology*, 58(12):3965, 2013.

[107] J. Rahmer, A. Halkola, B. Gleich, I. Schmale, and J. Borgert. First experimental evidence of the feasibility of multi-color magnetic particle imaging. *Physics in medicine and biology*, 60(5):1775, 2015.

[108] J. Rahmer, J. Weizenecker, B. Gleich, and J. Borgert. Signal encoding in magnetic particle imaging: properties of the system function. *BMC medical imaging*, 9(1):4, 2009.

[109] J. Rahmer, J. Weizenecker, B. Gleich, and J. Borgert. Analysis of a 3-d system function measured for magnetic particle imaging. *Medical Imaging, IEEE Transactions on*, 31(6):1289–1299, 2012.

[110] D.N. Reddan, L.A. Szczech, R.H. Tuttle, L.K. Shaw, R.H. Jones, S.J. Schwab, M.S. Smith, R.M. Califf, D.B. Mark, and W.F. Owen. Chronic kidney disease, mortality, and treatment strategies among patients with clinically significant coronary artery disease. *Journal of the American Society of Nephrology*, 14(9):2373–2380, 2003.

[111] M.D. Robson, J.C. Gore, and R.T. Constable. Measurement of the point spread function in mri using constant time imaging. *Magnetic resonance in medicine*, 38(5):733–740, 1997.

[112] E.U. Saritas, P.W. Goodwill, L.R. Croft, J.J. Konkle, K. Lu, B. Zheng, and S.M. Conolly. Magnetic particle imaging (mpi) for nmr and mri researchers. *Journal of Magnetic Resonance*, 229:116–126, 2013.

[113] E.U. Saritas, P.W. Goodwill, G.Z. Zhang, and S.M. Conolly. Magnetostimulation limits in magnetic particle imaging. *Medical Imaging, IEEE Transactions on*, 32(9):1600–1610, 2013.

[114] V. Schaller, G. Wahnström, A. Sanz-Velasco, P. Enoksson, and C. Johansson. Monte carlo simulation of magnetic multi-core nanoparticles. *Journal of Magnetism and Magnetic Materials*, 321(10):1400–1403, 2009.

[115] I. Schmale, B. Gleich, and J. Borgert. Noise within magnetic particle imaging. In *Magnetic Nanoparticles: Particle Science, Imaging Technology, and Clinical Applications: Proceedings of the First International Workshop on Magnatic Particle Imaging*, page 154, 2010.

[116] I. Schmale, B. Gleich, J. Rahmer, C. Bontus, J. Schmidt, and J. Borgert. Mpi safety in the view of mri safety standards. *Magnetics, IEEE Transactions on*, 51(2):1–4, 2015.

[117] I. Schmale, J. Rahmer, B. Gleich, J. Borgert, and J. Weizenecker. Point spread function analysis of magnetic particles. In *Magnetic Particle Imaging*, pages 287–292. Springer, 2012.

[118] D. Schmidt, D. Eberbeck, U. Steinhoff, and F. Wiekhorst. Finding the magnetic size distribution of magnetic nanoparticles from magnetization measurements via the iterative kaczmarz algorithm. *Journal of Magnetism and Magnetic Materials*, 2016.

[119] D. Schmidt, F. Palmetshofer, D. Heinke, U. Steinhoff, and F. Ludwig. A phenomenological description of the mps signal using a model for the field dependence of the effective relaxation time. *IEEE Transactions on Magnetics*, 51(2):1–4, 2015.

[120] R.F. Schmidt. *Physiologie des Menschen*. Springer-Verlag, 2013.

[121] G. Schütz, J. Lohrke, and J. Hütter. *Magnetic Nanoparticles: Particle Science, Imaging Technology, and Clinical Applications*, chapter Use of Resovist in magnetic particle imaging, pages 32–36. World Scientific, 2010.

[122] C.E. Shannon. Communication in the presence of noise. *Proceedings of the IRE*, 37(1):10–21, 1949.

[123] M.I. Shliomis. Magnetic fluids. *Soviet Physics Uspekhi*, 17(2):153, 1974.

[124] C.R. Smith and J.W. Erker. Low-cost, high-resolution x-ray detector system for digital radiography and computed tomography. In *SPIE's 1993 International Symposium on Optics, Imaging, and Instrumentation*, pages 31–35, 1993.

[125] S.W. Smith. *The Scientist & Engineer's Guide to Digital Signal Processing*. California Technical Pub, 1997.

[126] H.P. Song, J.Y. Yang, S.L. Lo, Y. Wang, W. M. Fan, X. S. Tang, J. M. Xue, and S. Wang. Gene transfer using self-assembled ternary complexes of cationic magnetic nanoparticles, plasmid dna and cell-penetrating tat peptide. *Biomaterials*, 31(4):769–778, 2010.

[127] L.W.E. Starmans, D. Burdinski, N.P.M. Haex, R.P.M. Moonen, G.J. Strijkers, K. Nicolay, and H. Grüll. Iron oxide nanoparticle-micelles (ion-micelles) for sensitive (molecular) magnetic particle imaging and magnetic resonance imaging. *PloS one*, 8(2):e57335, 2013.

[128] S. Sun and H. Zeng. Size-controlled synthesis of magnetite nanoparticles. *Journal of the American Chemical Society*, 124(28):8204–8205, 2002.

[129] P. Tartaj, M. del Puerto Morales, S. Veintemillas-Verdaguer, T. Gonzalez-Carreno, and C.J. Serna. The preparation of magnetic nanoparticles for applications in biomedicine. *Journal of Physics D: Applied Physics*, 36(13):R182, 2003.

[130] B. Thiesen and A. Jordan. Clinical applications of magnetic nanoparticles for hyperthermia. *International Journal of Hyperthermia*, 24(6):467–474, 2008.

[131] A. Tomitaka, R.M. Ferguson, A.P. Khandhar, S.J. Kemp, S. Ota, K. Nakamura, Y. Takemura, and K.M. Krishnan. Variation of magnetic particle imaging tracer performance with amplitude and frequency of the applied magnetic field. *Magnetics, IEEE Transactions on*, 52(2):1–4, 2015.

[132] M.S. Van Lysel. The aapm/rsna physics tutorial for residents: Fluoroscopy: Optical coupling and the video system 1. *Radiographics*, 20(6):1769–1786, 2000.

[133] O. Veiseh, J.W. Gunn, and M. Zhang. Design and fabrication of magnetic nanoparticles for targeted drug delivery and imaging. *Advanced drug delivery reviews*, 62(3):284–304, 2010.

[134] O. Veiseh, F.M. Kievit, J.W. Gunn, B.D. Ratner, and M. Zhang. A ligand-mediated nanovector for targeted gene delivery and transfection in cancer cells. *Biomaterials*, 30(4):649–657, 2009.

[135] T. Viereck, C. Kuhlmann, S. Draack, F. Ludwig, and M. Schilling. Functional magnetic particle imaging in measurement and simulation. In *International Workshop on Magnetic Particle Imaging (IWMPI) 2016*, 2016.

[136] A.F. Wang, J.J. Ying, Y.J. Yan, R.H. Liu, X.G. Luo, Z.Y. Li, X.F. Wang, M. Zhang, G.J. Ye, P. Cheng, et al. Superconductivity at 32 k in single-crystalline $Rb_{0.78}Fe_2Se_{1.78}$. *Physical Review B*, 83(6):060512, 2011.

[137] T. Wawrzik, C. Kuhlmann, F. Ludwig, and M. Schilling. Estimating particle mobility in mpi. In *2013 International Workshop on Magnetic Particle Imaging (IWMPI)*, 2013.

[138] T. Wawrzik, M. Schilling, and F. Ludwig. Perspectives of magnetic particle spectroscopy for magnetic nanoparticle characterization. In *Magnetic Particle Imaging*, 2012.

[139] A. Weber and T. Knopp. Symmetries of the 2d magnetic particle imaging system matrix. *Physics in medicine and biology*, 60(10):4033, 2015.

[140] J. Weizenecker, J. Borgert, and B. Gleich. A simulation study on the resolution and sensitivity of magnetic particle imaging. *Physics in Medicine and biology*, 52(21):6363, 2007.

[141] J. Weizenecker, B. Gleich, J. Rahmer, and J. Borgert. Micro-magnetic simulation study on the magnetic particle imaging performance of anisotropic mono-domain particles. *Physics in medicine and biology*, 57(22):7317, 2012.

[142] J. Weizenecker, B. Gleich, J. Rahmer, H. Dahnke, and J. Borgert. Three-dimensional real-time in vivo magnetic particle imaging. *Physics in medicine and biology*, 54(5):L1, 2009.

[143] F. Wiekhorst, U. Steinhoff, D. Eberbeck, and L. Trahms. Magnetorelaxometry assisting biomedical applications of magnetic nanoparticles. *Pharmaceutical research*, 29(5):1189–1202, 2012.

[144] D.S. Xue, C.X. Gao, Q.F. Liu, and L.Y. Zhang. Preparation and characterization of haematite nanowire arrays. *Journal of Physics: Condensed Matter*, 15(9):1455, 2003.

[145] T. Yoshida and K. Enpuku. Simulation and quantitative clarification of ac susceptibility of magnetic fluid in nonlinear brownian relaxation region. *Japanese Journal of Applied Physics*, 48(12R):127002, 2009.

[146] T. Yoshida and K. Enpuku. Nonlinear behavior of magnetic fluid in brownian relaxation: Numerical simulation and derivation of empirical model. In *Magnetic Particle Imaging*, pages 9–13. Springer Science + Business Media, 2012.

[147] T. Yoshida, K. Enpuku, F. Ludwig, J. Dieckhoff, T. Wawrzik, A. Lak, and M. Schilling. *Magnetic Particle Imaging*, chapter Characterization of Resovist® nanoparticles for magnetic particle imaging, pages 3–7. Springer, 2012.